Modelling the Wave-Induced Collisions of Ice Floes

Lucas J. Yiew

Thesis submitted for the degree of

Doctor of Philosophy

in

Applied Mathematics

at

The University of Adelaide

Faculty of Engineering, Computer and Mathematical Sciences

School of Mathematical Sciences

February 22, 2017

Contents

List of Tables

List of Figures

Signed Statement

I certify that this work contains no material which has been accepted for the award of any other degree or diploma in my name in any university or other tertiary institution and, to the best of my knowledge and belief, contains no material previously published or written by another person, except where due reference has been made in the text. In addition, I certify that no part of this work will, in the future, be used in a submission in my name for any other degree or diploma in any university or other tertiary institution without the prior approval of the University of Adelaide and where applicable, any partner institution responsible for the joint award of this degree.

I give consent to this copy of my thesis, when deposited in the University Library, being made available for loan and photocopying, subject to the provisions of the Copyright Act 1968.

I also give permission for the digital version of my thesis to be made available on the web, via the University's digital research repository, the Library Search and also through web search engines, unless permission has been granted by the University to restrict access for a period of time.

SIGNED: ..... DATE: .....

Acknowledgements

I would like to express my deepest gratitude to my supervisors Dr. Luke Bennetts and Assoc. Prof. Mike Meylan for their support and guidance. Dr. Bennetts has been an exemplary role model and has been generous in providing much of his time and effort to guide me in my research over the last three years. I must thank him for assisting me with a smooth transition from engineering to mathematics.

Assoc. Prof. Meylan has also been instrumental to the progress of my research. It was a privilege to work with him in Newcastle on a number of occasions.

I must acknowledge the support of Prof. Giles Thomas and Assoc. Prof. Guoxing Huang (through the recommendation of Assoc. Prof. Adrian Law), who provided us with the facilities and funds to perform wave basin experiments at the Australian Maritime College and the Dalian University of Technology. I am deeply appreciative for the technical assistance from Benjamin French, Tian Yong Jin, Song Yue and Sun Zhen Xiang during the experiments.

I would also like to thank Prof. Hayley Shen and Assoc. Prof. Agnieszka Herman for allowing me the opportunity to share my research with them.

Finally, I am thankful for the support and love from my parents, the Ki family, and most of all my wife, Grace, who has been remarkably longsuffering and patient with me throughout my studies, all the while encouraging and motivating me to better myself each day.

This thesis contains excerpts which have been published in the following journals and conference proceedings:

Yiew, L. J., Bennetts, L. G., Meylan, M. H., French, B. J., & Thomas, G. A. (2016). Hydrodynamic responses of a thin floating disk to regular waves. *Ocean Modelling*, 97, 52–64.

Meylan, M. H., Yiew, L. J., Bennetts, L. G., French, B. J., & Thomas, G. A. (2015). Surge motion of an ice floe in waves: comparison of theoretical and experimental models. *Annals of Glaciology*, 56(69), 155–159.

Bennetts, L. G., Yiew, L. J., Meylan, M. H., French, B. J., & Thomas, G. A. (2014). An experimental model of non-rafting collisions between ice floes caused by monochromatic water waves. *Proceedings of the 19th Australasian Fluid Mechanics Conference*.

Abstract

The wave-induced collisions and rafting of ice floes are investigated experimentally and theoretically. Results from a series of wave basin experiments are presented. Ice floes are simulated experimentally using thin plastic disks. The first round of experiments focusses on measuring the oscillatory surge, heave, pitch and drift motions of solitary floes. The second and third rounds of experiments record the motions of two adjacent floes. Rafting is suppressed in the second round, and allowed in the third round. Collision and rafting regimes are identified, and collision behaviours are quantified over a range of incident wavelengths and wave amplitudes.

Two mathematical models are proposed to model the wave-induced motions of solitary floes. The first is based on slope-sliding theory, and the second is based on linear potential-flow theory. Both models are validated using results from the single-floe experiments. Model-data comparisons show that the slope-sliding model is valid in the long-wavelength regime, and potential-flow model is more accurate in shorter wavelengths.

A two-floe collision model is then developed to replicate the conditions of the two-floe experiments. Slope-sliding theory is used to model floe motions. A time-stepping algorithm is implemented to determine the occurrence of collision and rafting events. Predicted collision behaviours are compared with results from the two-floe experiments. Good agreement is attained in incident waves of intermediate to long wavelengths.

Chapter 1

Introduction

1.1 Background and context

In the Arctic and Antarctic regions, vast swaths of the sea ice cover are exposed to the effects of ocean waves. Liu and Mollo-Christensen (1988) and many others have reported observations of ocean waves penetrating hundreds of kilometres into the ice cover. The region of sea ice influenced by interactions with the open ocean is known as the marginal ice zone (MIZ) (Wadhams, 1986). When ocean waves penetrate into the MIZ, they encounter discrete, fragmented, thin sheets of sea ice (otherwise known as ice floes) of increasing horizontal dimensions (Squire and Moore, 1980). Ice floes range from several metres to a hundred kilometres in length (Rothrock and Thorndike, 1984) and have small thickness to length ratios. The size and shape distributions and physical properties of ice floes vary according to seasonal conditions and their geographic location within the MIZ.

The interaction between waves and sea ice alters the distribution of ice floes and affects the rheological properties and extent of the MIZ (Squire et al., 1995; Feltham, 2005). This in turn affects large-scale marine and atmospheric processes such as thermohaline circulations, ice-albedo effects, and heat and moisture exchanges between the ocean and atmosphere (Feltham, 2008). Recent increases in global temperatures have accelerated the melting of sea ice in the Arctic (Stroeve et al., 2012), thereby causing the sea ice cover to progressively weaken and disperse. In the Antarctic, opposite trends have been observed. Nonetheless, on a global scale the overall sea

ice extent remains on a downward trend (Parkinson and DiGirolamo, 2016). Additionally, destructive storms, which generate stronger waves, are also becoming more prevalent in response to climate change (Squire, 2007). Stronger waves penetrate deeper into the MIZ and further weaken the ice cover.

With the global extent of sea ice reaching multiple record lows in the past decade (Parkinson and DiGirolamo, 2016), there is an increasing demand for improved predictions of seasonal and long-term sea ice conditions. Accurate forecasts are also required due to the proliferation of maritime activities in the Arctic regions, which have resulted from the opening of the ice cover (Stephenson et al., 2011). Sea ice is a navigational hazard to ocean going vessels operating in high latitudes, particularly those involved in the fisheries, tourism, shipping and offshore industries.

In order to develop accurate models of sea ice, better understanding of wave-ice dynamics is needed. Contemporary operational forecast models of sea ice are currently deficient, in that they do not account for the granular rheologies of ice, and do not include the effects of waves in the ice-covered ocean (Williams et al., 2013b). Due to the complexities associated with modelling these coupled processes, physical exchanges between waves and sea ice have not been fully incorporated into operational ice-ocean and oceanic global circulation models (Squire et al., 2013).

Wave-ice dynamics play a significant role in the overall dynamics and thermodynamics of the sea ice cover in the MIZ. Ocean waves weaken and breakup the ice through oscillatory bending (Langhorne et al., 1998; Prinsenberg and Peterson, 2011). Floes broken up by waves are more susceptible to melting and are much easily driven by wind, current and waves. Waves can also run over the surface of floes in a process known as overwashing, and accelerate ice melt (Wadhams et al., 1979; Massom and Stammerjohn, 2010). When ocean waves propagate through the MIZ, wave energy is progressively dispersed as it interacts with ice floes. This process, which is known as wave attenuation, determines the extent of influence of waves through the MIZ. Wave attenuation has been attributed to energy dissipative mechanisms such as wave scattering (Bennetts et al., 2010), viscous losses (e.g. wave breaking and turbulence Keller, 1998), and hysteresis (as floes flex in response to waves) (Wadhams, 1973).

The wave-induced collisions between ice floes have also been identified as another dissipative mechanism. When ice floes collide, energy is lost through inelastic collisions. Shen and Squire (1998) found that collisions were one of the two most dominant energy dissipative mechanisms in a compact field of pancake ice (relatively small circular ice floes); the other being turbulence. McKenna and Crocker (1990) used measurements from the Labrador Ice Margin Experiments (LIMEX) and estimated that the amount of wave energy lost to inelastic collisions is 14% of the total energy lost.

Floe collisions are also an important mechanism in determining the size and shape distributions of floes within an ice field. Collisions can either result in mechanical degradation of floes at their edges after repeatedly colliding (McKenna and Crocker, 1990), or cause floes to grow in size if they freeze together upon contact (Shen and Ackley, 1991). In certain situations, waves may cause floes to collide sufficiently out of plane, such that floes overlap with each other. This phenomenon is known as rafting. If floes stay rafted long enough, they may bond together. Rafting has been suggested to contribute significantly to the thickening of the ice cover, much more so than thermodynamic growth (Dai et al., 2004).

1.2 Existing theoretical models

A handful of field experiments were conducted in the 1980s and 1990s to investigate the cause, nature and consequence of collisions between floes. Field observations by Martin and Becker (1987, 1988) in the Bering and Greenland Seas showed that the majority of floe collisions in the MIZ are caused by ocean waves. When an oncoming wave encounters a floe, the floe responds by surging back and forth and drifting in the direction of the travelling wave. Floes collide due to a combination of these motions. Rottier (1992) measured interaction event rates of floes from the Barents and Greenland Seas and showed a relationship between event rates and the ratio between the root-mean-square wave amplitude and amount of open water between floes.

A number of theoretical models have been developed to simulate floe collisions in

order to confirm these observations. The majority of these models are based on simplified assumptions of floe motions relative to waves. For example, some models approximate a floe's response with the motions of water particles at the free-surface. McKenna and Crocker (1990) and Gao (1991) modelled the collisions of ice floes by applying this assumption. In their models, all non-unitary floe responses (with respect to water particle motions) are neglected. Gao (1991) also used this assumption to develop a stochastic model of floe collisions. The motions of floes and their spacing distances were treated as a stochastic processes. The model was used to calculate collision probabilities and frequencies.

In other collision models, a more complex formulation of wave-induced floe motion, based on slope-sliding theory, is used. Slope-sliding theory is derived by representing floating bodies (or floes in this case) as objects travelling on the surface of a sinusoidal wave train. Motions are induced by a gravitational force proportional to the slope of the wave (hence the name "slope-sliding"). This theory was first developed by Rumer et al. (1979), and then independently derived by Marchenko (1999). Both versions of the model are based on extensions to Morison's equation (Morison et al., 1950), which decomposes the forces acting on a body into inertial and drag components. Slope-sliding theory assumes that floating bodies do not modify the surrounding wave field. This is also known as the Froude-Kryloff assumption, and is applicable when wavelengths are much larger than the horizontal dimension of a thin body (Newman, 1977).

Shen and Ackley (1991) and Shen and Squire (1998) proposed a one-dimensional collision model based on slope-sliding theory. Their model predicts the horizontal responses of a one-dimensional array of floes. Floe interactions were simulated using a spring-dashpot model, in which floes are represented as elastic bodies, and collisions are governed by a spring coefficient proportional to the elastic modulus of the floe, and a damping coefficient, which is a function of the coefficient of restitution. Shen and Ackley focussed on simulating a field of interacting floes, and showed that the herding of ice floes could be simulated. They describe wave herding as the "grouping of floes into bands of a width of the wavelength". Shen and Ackley also showed that with an appropriate damping constant, it was possible simulate the prolonged contact of floes. They suggest that under the right thermodynamic con-

ditions, prolonged contact will lead to the formation of composite floes as they freeze together. Shen and Ackley also quantified collision behaviours and showed that the frequency of collisions depends on the elastic properties of floes and the wave amplitude. Later, Shen and Squire applied the same collision model to quantify the significance of floe collisions to the attenuation of waves. They found the energy dissipated from collisions to be a function of the restitution coefficient (i.e. proportion of kinetic energy remaining after a collision) and their impact velocities.

Rottier (1992) proposed an alternative model based on the dynamic equilibrium of forces acting on a floe. Floes are represented as two-dimensional rectangular rigid bodies. Brash ice (ice fragments), which is a product of the collision process, was accounted for by including a small body between two floes. In Rottier's model, wave forcing is due to hydrostatic and hydrodynamic pressures around the wetted surface of the floe. Rottier adopted the Froude-Kryloff assumption to simplify the model (i.e. wave scattering effects were neglected). The model was used to predict collision rates in a random wave field (he refers to them as "interaction events").

Other collision models, such as the ones developed by Shen et al. (1987), Lu et al. (1989), Feltham (2005) and Herman (2011, 2012, 2013) do not account for the wave-induced motions of floes. Momentum is imparted by atmospheric and oceanic pressure (i.e. wind and current). These models are significantly different to those previously mentioned in terms of their approach to modelling floe collisions – granular flow theory is applied to simulate the large-scale effects of collisions on the MIZ. These models consist of momentum balance equations for the sea ice-ocean mixture layer and energy balance equations for kinetic energy fluxes. Collisions are integrated into the model as an internal ice stress tensor.

Another conventional approach towards modelling wave-induced floe motions is to apply linear potential-flow theory. This theory is widely utilised in a variety of hydrodynamic and aerodynamic applications. (For example, it can be used to model the wave-induced responses of ships and the air flow around aerofoils.) In potential-flow theory, the velocity field of a inviscid, incompressible and irrotational fluid is represented as the gradient of a scalar velocity potential (Linton and McIver, 2001). Motions are induced by hydrodynamic forces on the wetted surfaces of a floating body. Models based on potential-flow theory are intrinsically more sophisticated

than, say, slope-sliding models since they contain information on the velocity field throughout the fluid domain.

Wadhams (1973, 1986) applied this theory to formulate a model for the wave-induced response of a solitary ice floe and the modification of the surrounding wave field, but was not able to generate solutions to the problem. Meylan and Squire (1993b,a, 1994) obtained solutions to a two-dimensional problem (one horizontal dimension and one depth dimension) for an ice floe of finite length. In the models of Meylan and Squire, ice floes are treated as elastic bodies, on the basis that floes flex in response to waves. Energy is allowed to propagate through the floe as a flexural-gravity wave. The bending of ice floes, however, is only significant in certain wavelength regimes. When floe lengths are small in comparison to the wavelength, the flexural response of floes are small enough to be ignored. Based on this assumption, Masson and LeBlond (1989) developed a three-dimensional model for a solitary rigid floe. The model calculates the amplitudes of the scattered wavefield in all horizontal directions.

Kohout and Meylan (2008) and Williams et al. (2013a,b) further extended existing two-dimensional models to predict the wave-induced breakup of a large collection of floes. Masson and LeBlond (1989), Meylan et al. (1997) and Bennetts et al. (2010) further extended existing three-dimensional models to calculate the attenuation of waves through large groups of floes. Despite the inclusion of multiple floes, none of these models consider the effect of floe collisions.

As for the phenomenon of rafting, several authors have investigated the physical process of rafting (e.g. Parmerter, 1975; Hopkins et al., 1999; Bailey et al., 2010), however none of these models attempt to predict the wave conditions required for rafting to occur. For example, Hopkins et al. (1999) modelled rafting by pushing two ice sheets together at constant speeds. This was to simulate the forces between much larger sheets of pack ice. Parmerter (1975) did however investigate the in-plane force required to raft flexible ice sheets. If the in-plane force is associated with wave forces, one might be able to deduce the wave characteristics required for rafting to occur. Parmerter reports that only a small percentage of the buckling load is needed to initiate rafting. The only relevant investigation of wave-induced rafting was conducted by Dai et al. (2004), who developed a numerical model simulating the

buildup of rafted pancake ice floes in waves. Their mechanism of rafting, however, was not purely due to waves. In their model, rafting occurs when floes encounter a large and relatively unmovable barrier, which represents pack ice.

1.3 Relevant laboratory experiments

A number of laboratory experiments have been conducted to verify existing theoretical wave-ice interaction models, and indicate physical phenomena not yet accounted for. Frankenstein (1996) conducted wave tank experiments in non-refrigerated (i.e. room temperature) and refrigerated environments to verify the slope-sliding models of Rumer et al. (1979) and Shen and Ackley (1991). For non-refrigerated tests, the oscillatory surge amplitudes, drift velocities, and collision frequencies and durations of 1 to 4 rectangular polypropylene floes (positioned in line with the direction of incident waves) of thickness to length quotients $H/D_l \approx 1.6 \times 10^{-2}$ and 3.2×10^{-2} were measured in regular incident waves of wavelengths λ to floe lengths $\lambda/D_l \approx 9.5$ to 66.3 and in incident wave steepnesses $ka \approx 0.005$ to 0.14 (where $k = 2\pi/\lambda$ is the wavenumber and a is the incident amplitude). Floe lengths were measured longitudinally (i.e. in line with the direction of incident waves). For refrigerated tests, which were conducted in air temperatures between $-14°$C to $-5°$C, the same measurements were recorded for 1 to 50 rectangular sheets of urea ice of $H/D_l \approx 5.1 \times 10^{-2}$ to 1.2×10^{-1}. Tests were conducted in regular waves of $\lambda/D_l \approx 15.8$ to 29.1 and $ka \approx 0.03$ to 0.1. Experimental results from both sets of tests were generally in poor agreement to theoretical predictions of surge, drift, collision frequencies and durations. Frankenstein attributed this to sensitivities to initial conditions, experimental errors and physical effects (specific to the design of the experiment) not included in the model. For example, friction was generated between floes and a guide wire installed to prevent floes from rotating horizontally. This resulted in the dampening of floe motions.

Bennetts and Williams (2015) performed wave basin experiments to investigate wave energy transmission through a collection of thin disks, and validate the linear potential-flow models of Meylan et al. (1997) and Bennetts and Squire (2012); the latter of which was used in Williams et al. (2013a,b). Experiments were conducted

on a array of 40-80 identical thin wooden disks. The disks had a thickness H to diameter D quotient of $H/D \approx 3.3 \times 10^{-2}$. The proportion of wave energy transmitted was measured in regular incident waves of $\lambda/D \approx 0.67$ to 6.28, and wave steepnesses $ka \approx 0.04$ to 0.26. Experiments showed that the models predict the transmitted energy accurately for small incident amplitudes and low concentrations of the disks. The models, however, were inaccurate for larger incident amplitudes when wave overwash of the disks was strong. Recall, overwash refers to the phenomenon of waves running semi-continuously over the top of the disks, due to their small freeboards. The models were also inaccurate for high concentrations due to collisions between the disks and rafting. The potential-flow/thin-plate model does not include the highly nonlinear processes of overwash and collisions.

Bennetts and Williams (2015) also conducted a series of tests on a solitary wooden disk and presented the oscillatory surge, heave and pitch motions for a subset of incident frequencies and amplitudes used for their multiple-disk tests. Measurements were compared to the predictions of the potential-flow/thin-plate model, and the model was found, in general, to be accurate. They showed the model was least accurate for a test in which strong overwash occurred. In particular, the model overpredicted the translational motions, surge and heave, and underpredicted the rotational motion, pitch.

Montiel et al. (2013a,b) also performed experiments on solitary disks. They presented measurements of the flexural motions of a thin plastic disk in response to regular incident waves, as functions of the incident frequency. Tests were conducted on three thin disks of $H/D = 2.1 \times 10^{-3}$ to 6.9×10^{-3}, in incident wavelengths ranging from $\lambda/D \approx 0.63$ to 3.14, and in two small steepnesses $ka \approx 0.03$ and 0.06. Measurements were also compared to predictions of the potential-flow/thin-plate model. However, they used a vertical rod through the centre of the disk to suppress surge, and a barrier around the edge of the disk to prevent overwash.

McGovern and Bai (2014) presented measurements of the heave and a composite surge and drift of solitary floes made of paraffin wax. Several shapes were tested. This included square, rectangular and triangular shapes, but not disks. They modelled thick multiyear floes, and hence used relatively large thickness over characteristic length, D_c, quotients, typically $H/D_c = \mathrm{O}(10^{-1})$. Characteristic length was

defined as the longest length along a floe's edge. Floes were tested in regular incident wavelengths ranging from $\lambda/D_c \approx 1.3$ to 10, and in steepness ranging from $ka \approx 0.03$ to 0.28. They studied heave and composite surge-drift as functions of λ/D_c and $2a/\lambda$, but did not compare these results to model predictions. They noted the occurrence of overwash for large incident amplitudes and high steepnesses, and suggested it as a source of the reduced heave responses they found in this regime, which mirrors the finding of Bennetts and Williams (2015).

McGovern and Bai also presented measurements of drift for their model floes. They compared the measurements to the predictions of Stokes drift theory. They found the theory slightly underestimates the measurements. This finding is consistent with that of Huang et al. (2011), who examined the drift velocities of square, circular and elliptical plates of thickness to longitudinal length quotients $H/D_l = 0.15$ and 0.225, in wavelengths between $\lambda/D_l \approx 6.3$ to 7.8 and in wave steepnesses between $ka \approx 0.04$ to 0.15.

1.4 Scope of thesis

In this thesis, the mechanics of wave-induced floe collisions will be investigated experimentally and theoretically. Wave basin experiments are implemented to simulate wave-ice interactions in a controlled laboratory environment. Regular waves (i.e. unidirectional waves of a single frequency and amplitude) are used to excite floes. In our experiments, thin plastic disks are used to simulate ice floes.

Experimental and theoretical analyses in this thesis are divided into three phases. The first phase focusses on quantifying and modelling the wave-induced motions of solitary floes. As such, the first round of experiments are conducted to measure the hydrodynamic behaviour of a single floe. Two theoretical single-floe models based on (i) slope-sliding theory and (ii) linear potential-flow theory are then investigated and validated using results from the single-floe experiments. As part of our analyses, we will determine the limits of validity of each model.

The second phase investigates the collisions between two adjacent floes. In the second round of experiments, floes are positioned inline with the direction of the

incident wave, and are allowed to collide under wave action. In this round of experiments, rafting is suppressed through the use of edge barriers. Experimental analyses are therefore restricted to non-rafting collisions. Collision behaviours are quantified over a range of incident wave conditions. A theoretical two-floe collision model is then proposed to predict the occurrence and behaviour of non-rafting collisions. In the first instance, we will develop the collision model based on modifications to the models of Shen and Ackley (1991) and Shen and Squire (1998). The accuracy and range of validity of the model will be assessed by comparing theoretical solutions with data from the non-rafting experiments.

The third and final phase investigates the phenomenon of rafting. A third round of wave basin experiments are performed to determine the wave conditions required for rafting to occur between two adjacent floes. Edge barriers are removed to allow for rafting. The two-floe collision model is modified to predict rafting events. Results are then compared with data from the rafting experiments.

Chapter 2

Single-floe experiments

The first round of wave basin experiments was conducted at the Australian Maritime College (AMC), Launceston, Australia in July 2013, using the Model Test Basin (MTB) facility. The purpose of the experiments was to simulate the motions of solitary ice floes in waves in order to understand the hydrodynamic behaviour of a floe in different wave regimes. This chapter describes the experimental methods and presents the results from our experiments.

2.1 Objectives

The three main objectives of the single-floe experiments were to:

1. simulate the interactions between solitary ice floes and waves;
2. understand the motions of single floes over a range of wave conditions;
3. obtain experimental data to validate theoretical single-floe models.

In these experiments, thin plastic disks were used to simulate ice floes. The properties of the model floes are described in § 2.2.2. Floes were set in motion by regular waves (i.e. monochromatic plane waves), which are characterised by a single wave frequency and amplitude. The range of test parameters considered are described in § 2.2.5.

2.2 Experimental method

2.2.1 Wave basin facility

The MTB facility houses a wave basin, which is 35 m long, 12 m wide, and 1 m deep. In the single-floe experiments, the basin was filled with fresh water of density $\rho \approx 1000\,\mathrm{kg\,m^{-3}}$ to a depth of $h = 0.83\,\mathrm{m}$.

Figure 2.2.1 shows a photo of the MTB being used in unrelated seakeeping experiments. Incident wave parameters (wave frequency and wave amplitude) are specified on a control program. The resulting wavefield is then generated by an electrically driven piston-type wave maker (left background). A sloping beach (right foreground) consisting of a dense grid of small rubber cylinders acts to disperse incident waves in order to minimise the influence of reflected waves on floe motions. Reflected wave amplitudes were measured to be less than 13% of incident wave amplitudes. This corresponds to a reflection of less than 1.7% of the incident wave energy. These percentages were calculated by fitting sinusoidal functions (for incident and reflected waves) to the measured wave profiles before and after the interference of reflected waves, and were based on the upper range of wavelengths tested in these experiments. For shorter wavelengths, a higher percentage of incident wave energy would be scattered by the beach, therefore the proportion of reflected energy would be smaller.

Figure 2.2.1: Image of the MTB being used for seakeeping experiments (`http://www.amc.edu.au/`).

2.2.2 Floe properties

Thin plastic disks were used to represent ice floes. Two model floes were tested in the experiments. Floes were manufactured from Nycel, an expanded rigid foam polyvinyl chloride (PVC) polymer. The floes had a radii $R = 200\,\mathrm{mm}$, thickness $H = 15\,\mathrm{mm}$, density $\rho_b \approx 636\,\mathrm{kg\,m^{-3}}$, and hence equilibrium draft $d \approx 9.55\,\mathrm{mm}$ and mass $m = 1.2\,\mathrm{kg}$. The centres of mass were assumed to coincide with the geometric centre, i.e. approximately 7.5 mm from the base of each floe and at the radial axis of symmetry.

An edge barrier, similar to the one used by Montiel (2012) and Montiel et al. (2013b), was installed on one floe. This floe is referred to as Floe B. The floe with no barrier is referred to as Floe NB. The edge barrier is a 50 mm high and 25 mm thick styrofoam ring. The function of the barrier was to prevent overwash, i.e. waves running over the surface of the floe, due to its small freeboard (Skene et al., 2015). The barrier therefore allows for investigations into the effect of overwash on the motions of floes. The left panel of Figure 2.2.2 shows a photo of Floe B.

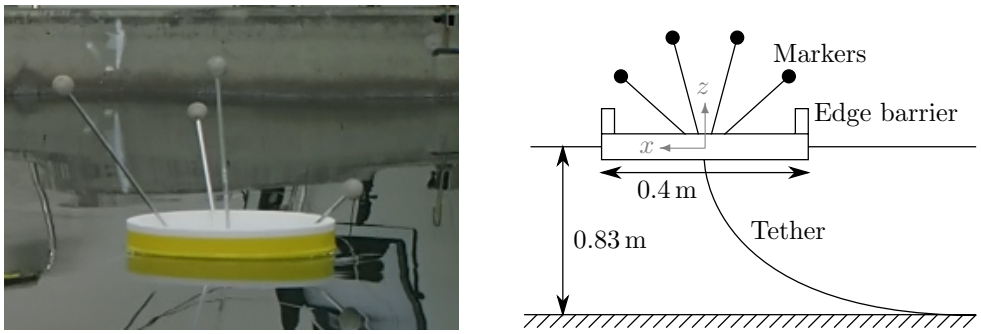

Figure 2.2.2: Left panel: Photo of Floe B, showing the edge barrier, rods and markers. Right panel: Cross-sectional schematic of Floe B, which shows the mooring system.

2.2.3 Coordinate system

Figure 2.2.3 shows the plan view of the MTB and the orientation of the coordinate system. The Cartesian coordinate system (x, y, z) is adopted to define locations in the basin. Locations on the horizontal plane, parallel to the equilibrium water surface, are defined by the coordinates (x, y). Vertical locations are defined by the coordinate z (shown in the right panel of Figure 2.2.2). The positive direction of

x corresponds to the direction from the wave maker to the beach. The positive direction of z points upward, with its origin coinciding with the equilibrium water surface.

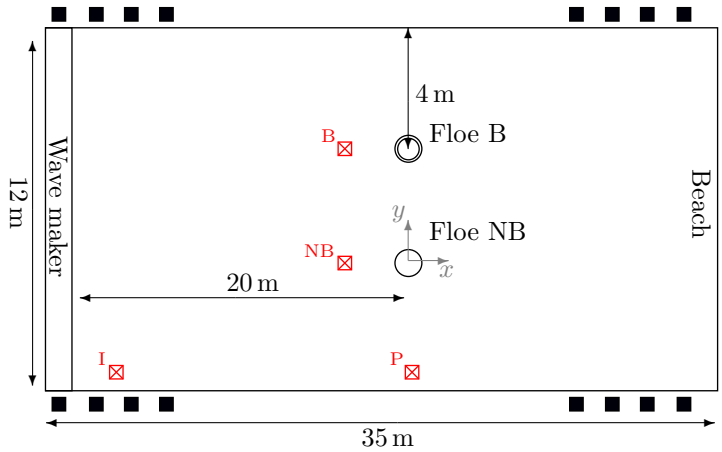

Figure 2.2.3: Schematic plan view of MTB. Wave probes (⊠) record the wave profiles at set locations, and motion tracking cameras (■) record the motions of the floes.

The locations of the floes at time t are defined according to the locations of their centres of mass, which are denoted as $(x, y, z) = (X_B(t), Y_B(t), Z_B(t))$ for Floe B, and $(x, y, z) = (X_{NB}(t), Y_{NB}(t), Z_{NB}(t))$ for Floe NB. The two floes were initially positioned 20 m down the basin. The floes were also positioned approximately 4 m apart, and 4 m from the sides of the basin. This was to minimise the interference caused by scattered waves between the floes and side walls. The origin of the Cartesian coordinate system is defined to coincide with the equilibrium location of Floe NB. Therefore $X_{NB}(0) = Y_{NB}(0) = 0$, and $X_B(0) = 0$ and $Y_B(0) = 4\,\mathrm{m}$.

Loose elastic tethers were attached to both floes to assist in resetting the floes to their initial positions after each test. The tethers also prevented the floes from drifting too far down the tank. Tethers were anchored to the basin floor. The cross-sectional schematic in the right panel of Figure 2.2.2 shows the attachment of the tether to the floe.

2.2.4 Instrumentation

Wave probes

Incident wave amplitudes and wave frequencies were recorded at four locations in the basin using a set of resistive wave probes. Figure 2.2.3 shows the locations of the wave probes. Two probes, which are labelled as Probes B and NB, were positioned directly in front of each respective floe to measure the wavefield interacting with the floes. These probes were placed approximately 2 m away from the floes, thus ensuring that floes would not collide into them during the tests. Another two probes were installed along the sides of the basin. Probe I was positioned close to the wave maker to monitor the developing incident wavefield, and Probe P was positioned 20 m down the wave basin, approximately in line with the floes.

Wave probes were calibrated at the start of each day to ensure accurate measurements of wave amplitudes and frequencies. Measured incident frequencies were within 2% of target values. Measured incident amplitudes were on average 15% smaller than the target amplitudes.

Motion tracking system

The Qualisys system was employed to record the motions of the floes. Qualisys is a non-contact stereoscopic motion tracking system, widely used in industrial and research applications. Qualisys is also commonly used in wave tank/floating body experiments, for example Law and Huang (2007), Huang et al. (2011) and Montiel (2012).

The system utilised eight pairs of infrared (IR) cameras and receivers installed along the perimeter of the wave basin, and a set of light-weight polystyrene tracking balls/markers (covered with a retro-reflective tape), four of which were mounted onto each floe via thin aluminium rods (see Figure 2.2.2). Rods were used to space the markers sufficiently far apart and at different heights. This was to prevent them from overlapping/merging on the IR camera image. Qualisys identifies each marker as a point. The locations of each marker are used to calculate the translational and rotational motions of the floes in real-time at 200 frames per second. The locations

of at least three markers were required to calculate the floe's motions. Four markers were used for each floe as a redundancy.

Qualisys calculates the motions of the floes in terms of its six (rigid-body) degrees of freedom. Since regular waves were used to excite the floes, the only dominant motions were those symmetric with respect to the x-axis. Oscillatory translations in the z-direction are known as heave. Oscillatory rotations about the y-axis are known as pitch. Translations in the x-direction are a sum of surge, drift, and restoration components due to the mooring system. Surge corresponds to oscillatory motions at the frequency of the incident wave. Drift is represented by the long-term net displacement in the x-direction. Figure 2.2.4 indicates the oscillatory motions with respect to the coordinate system.

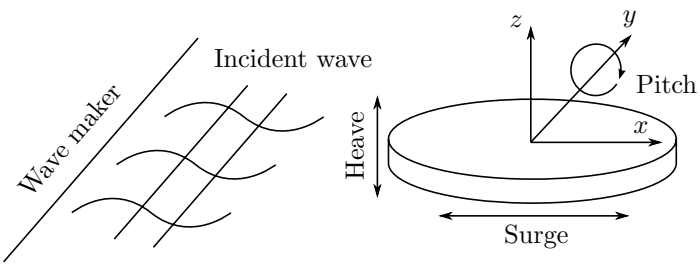

Figure 2.2.4: Schematic of Floe NB. Coordinate system and oscillatory motions are shown.

2.2.5 Test conditions

Incident wave frequencies and wave amplitudes were varied between tests. Target wave amplitudes ranged from $a = 5\,\mathrm{mm}$ to $40\,\mathrm{mm}$, and frequencies from $f = 0.5\,\mathrm{Hz}$ to $2.0\,\mathrm{Hz}$. This corresponds to incident wavelengths of $\lambda \approx 0.4\,\mathrm{m}$ to $5\,\mathrm{m}$. Wavelengths are calculated using the dispersion relation, which relates the wave number $k = 2\pi/\lambda$ to the wave frequency through the equation

$$k \tanh kh = \sigma. \tag{2.2.1}$$

The term $\sigma = \omega^2/g$ is the frequency parameter, with $\omega = 2\pi f$ representing the angular frequency, and $g \approx 9.81\,\mathrm{m\,s^{-2}}$ the gravitational acceleration.

Table 2.2.1 lists the test conditions for the single-floe experiments. Tests were di-

vided into two matrices. This first matrix was used to investigate the functional dependence of floe motions on wave frequency, for three wave amplitudes. Hence, there were more frequency entries than amplitude entries. The second matrix was used to investigate the effect of wave steepness on floe motions in two wave frequencies. Up to six wave amplitudes were considered.

Matrix 1

f [Hz]	0.5	0.55	0.6	0.65	0.7	0.8	0.9	1.05	1.25	1.4	1.5	1.6	1.7	1.8	1.9	2
λ [m]	4.91	4.31	3.81	3.37	3.00	2.38	1.91	1.41	1.00	0.80	0.69	0.61	0.54	0.48	0.43	0.39
$a = 10$ mm	•	•	•	•	•	•	•	•	•	•	•	•	•	•	•	•
$a = 20$ mm	•	•	•	•	•	•	•	•	•	•	•	•	•			
$a = 40$ mm	•	•	•	•	•	•	•	•	•							

Matrix 2

a [mm]	5	10	15	20	30	40
$f = 1.25$ Hz	•	•	•	•	•	•
$f = 1.5$ Hz	•	•	•	•		

Table 2.2.1: Summary of test matrices for single-floe experiment. Red bullets indicates tests with wave steepnesses $ka > 0.21$.

A total of 50 tests (inclusive of repeated tests) were conducted from Matrix 1, and 18 tests from Matrix 2. Results from tests with wave steepnesses exceeding $ka \approx 0.25$ are not reported. In these tests, waves were clearly within the breaking limit and were observed to be non-planar. This produced irregular wave amplitudes and significant lateral motions in the y-direction. Waves were observed to approach the breaking limit from $ka \approx 0.21$ onwards. Tests with wave steepnesses between $ka \approx 0.21$ to 0.25 are highlighted in red in Table 2.2.1.

2.2.6 Data processing

Data from the wave probes and Qualisys were collected simultaneously over a period of 60 s, starting at the moment the wave maker was activated, and ending when the wave maker was turned off. Figure 2.2.5 shows an example of the data generated by Qualisys. Here, the translational motion of Floe B in the z-direction is shown as a function of time. In this test, the incident wave frequency is $f = 1.25$ Hz and the measured amplitude is $a = 8.5$ mm.

Vertical lines in the left panel of Figure 2.2.5 indicate the steady-state interval, which

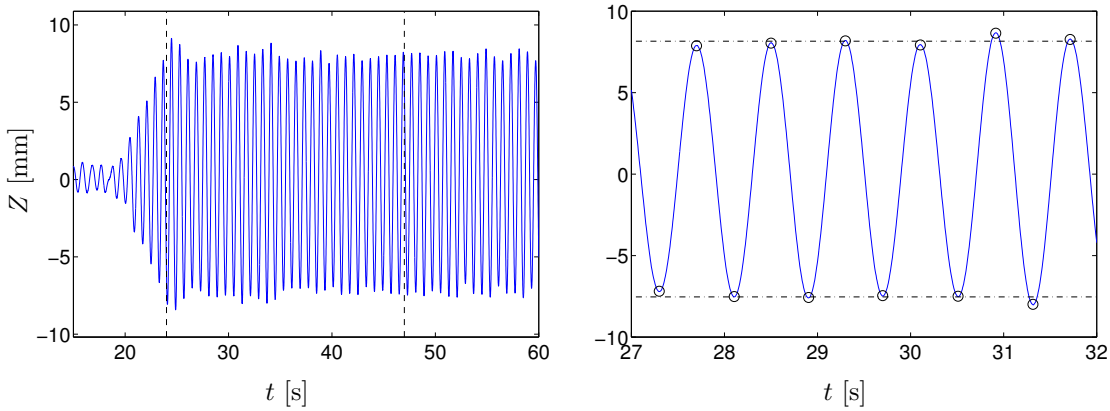

Figure 2.2.5: Left panel: Example of motions in the z-direction (−). Steady-state interval is denoted by vertical lines (- -). Right panel: Close-up of smoothed signal (−). Local maxima and minima (∘) are shown. Mean maxima and minima are denoted by horizontal lines (- · -).

is defined as the interval beginning after the initial transient motions, and ending when reflected waves from the beach return to the centre of the basin and interfere with incident waves. This interval is calculated using the phase velocity of the wave $c = f\lambda$. Analysis of all oscillatory motions and wave amplitudes are restricted to this common interval. Motions were observed to be significantly affected by reflected waves in some tests.

The steady-state interval in Figure 2.2.5 runs over approximately 26.25 incident wave periods. This gives a large sample size for calculations of average surge, heave, pitch and wave amplitudes. The intervals in all tests span an average of approximately 23 wave periods. Note that in long waves, the steady-state intervals and sample size decreases due to the increased phase velocity of incident waves. The converse is true for short waves.

Signal processing begins with the removal of noise from raw signals generated by Qualisys. This was done using the MATLAB `smooth` function together with the `lowess` smoothing method. This method employs a local regression, whereby each smoothed value is determined by neighbouring data points defined within the span (MATLAB, 2012). The `lowess` method also applies a weighted linear least squares algorithm, in which a regression weight function is defined for the data points contained within the span. The degree of smoothing is determined by the span, which is defined as a percentage of the total number of data points, less than or equal to

1. The larger the span, the greater the degree of smoothing. A span of 0.01 was specified to eliminate noise in all tests.

After removing noise from the raw signal, the local maxima and minima can be identified. The right panel of Figure 2.2.5 shows these points and their mean values. The heave amplitude a_h is calculated as half of the difference between the mean maxima and minima. The same procedure is repeated to calculate the pitch amplitude a_p and the measured wave amplitude.

Figure 2.2.6 shows the time series of translational motions in the x-direction, for the same test as in Figure 2.2.5. Surge is identified as the short-period oscillations. In the first 35 s of the test, the floe drifts freely. After drifting approximately 50 mm down the basin, the tether engages and begins to restrict drift. The result of this is long-period oscillations, which occur due to restoration forces from the mooring system.

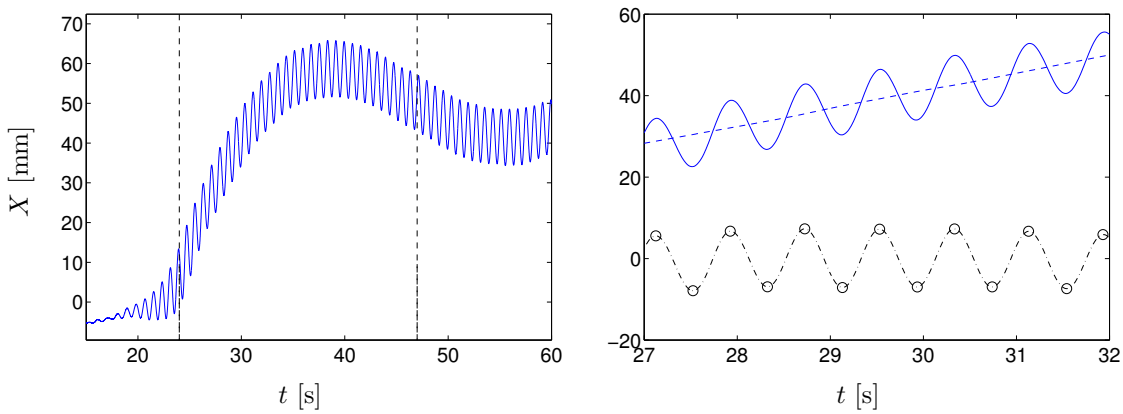

Figure 2.2.6: Left panel: As with the left panel of Figure 2.2.5 but for motions in the x-direction. Right panel: Close-up of smoothed signal (—), which is the sum of surge (-·-) and drift (- -). Local maxima and minima of surge motion (○) are shown.

Surge is isolated from drift using the `smooth` function with a span of 0.9. The output signal represents translations due to drift. The right panel of Figure 2.2.6 shows a close-up of the time-series before the tether engages. Surge is found by taking the difference between the full signal and drift. The surge amplitude a_s is then calculated using the same method as for heave and pitch.

Surge amplitudes were compared before and after the tether was engaged (i.e. in the free-drift and long-period oscillation intervals) to determine the effect of the tether

on surge motions. The effect on surge was shown to be minimal. For the example in Figure 2.2.6, the average surge amplitudes between 27-32 s and 40-45 s differed by less than 3%. Similar results were also observed in other tests.

2.3 Results

The following link contains the complete experimental dataset, from which results in this section are derived: `https://github.com/AdelaideUniversityMathSciences/SingleFloeModels/tree/master/SingleFloeExperiments`.

2.3.1 Response amplitude operators

Surge, heave and pitch motions are conventionally expressed in terms of nondimensional quantities known as response amplitude operators (RAOs) (see Newman, 1977; Faltinsen, 1990, for example). RAOs give an indication of floe motions in relation to wave motions. The surge RAO is calculated as $a_s/\{a \coth kh\}$, and the heave RAO is a_h/a. The terms $a \coth kh$ and a respectively represent the maximum horizontal and vertical displacements of a fluid particle at the free-surface. The pitch RAO is calculated as a_p/ka, with ka the incident wave steepness. Measured wave amplitudes are used in the calculation of all RAOs.

Figure 2.3.1 shows the surge, heave and pitch RAOs of Floe B, as functions of the incident wavelength nondimensionalised with respect to the disk diameter, $D = 2R$. Wavelengths are nondimensionalised to identify behavioural trends in different wavelength regimes. Experimental and numerical studies such as Murray et al. (1983) and Masson and LeBlond (1989) have shown that the motions of floating bodies are comparable to the motions of fluid particles in long waves but decrease in shorter waves.

Only data from Matrix 1 is considered in Figure 2.3.1. Error bars, shown in grey, indicate the RAOs corresponding to the maximum and minimum surge, heave and pitch amplitudes in each test. Median errors are largest for surge at $\pm 13\%$, and least for pitch at $\pm 7\%$.

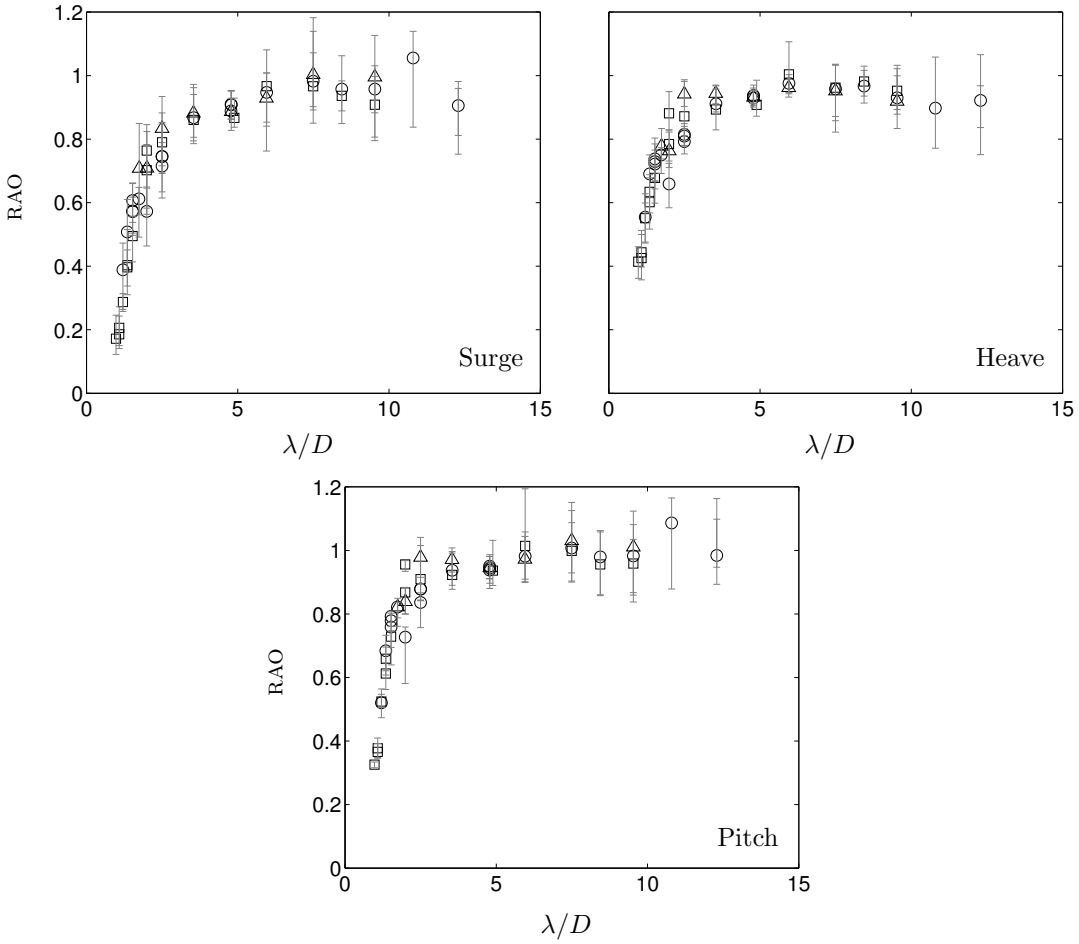

Figure 2.3.1: RAOs for Floe B for Matrix 1, as functions of nondimensional incident wavelength. Data are grouped according to target incident wave amplitude: a =10 mm (□), 20 mm (○) and 40 mm (△). Error bars are shown.

Figure 2.3.1 shows very little spread in RAOs between different wave amplitudes. This implies that surge, heave and pitch are linear with respect to wave amplitude. The mean range of RAOs for different wave amplitudes is approximately 0.065. Figure 6 in Yiew et al. (2016) also shows linear responses for Floe NB, with the mean range of RAOs at 0.053. Linearity with respect to wave amplitude is expected since tests were conducted within the regimes where viscous (nonlinear) wave forces are insignificant. Figure 1.1 in Linton and McIver (2001) shows these linear regimes to occur below the wave-breaking limit and in intermediate to short wavelengths.

In Figure 2.3.1, RAOs approach a unitary value for λ/D approximately greater than 3. In long waves, floes do not modify the incident wavefield. This is demonstrated in an example shown in the left panel of Figure 2.3.2. Here, $\lambda/D = 8.4$. In this wavelength regime, floes behave like fluid particles at the free-surface and follow the same trajectory (John, 1949; Murray et al., 1983; Lever et al., 1988).

Figure 2.3.2: Example of changes to the wave field in the long- and short-wavelength regime (left and right panels, respectively).

For λ/D less than 3, RAOs decrease with decreasing wavelengths. In shorter wavelengths, incident waves diffract and radiate around the floe. The right panel of Figure 2.3.2 shows an example of this occurring when $\lambda/D = 1.7$. This effect is known as wave scattering. Scattered waves reduce the amount of wave energy imparted to the floe, thereby decreasing the RAOs (Masson and LeBlond, 1989). Video recordings of tests in Figure 2.3.2 can be downloaded through the following link: `https://github.com/AdelaideUniversityMathSciences/SingleFloeModels/tree/master/SingleFloeExperiments/Videos/Wavefield`.

Figure 2.3.3 compares the RAOs of Floes B and NB for the tests in the first matrix. Error bars are removed for clarity. On average, Floe NB has smaller RAOs than

Floe B. The largest difference is 16.4% for heave, and the smallest is 7.1 % for surge. The percentages are calculated using the difference between the mean RAOs for each floe at each incident wavelength, and averaged across all wavelengths. Differences between the RAOs for the two floes are greatest in the short-wavelength regime, $\lambda/D < 3$. The largest difference is 0.24, which occurs for heave at $\lambda/D = 0.9$.

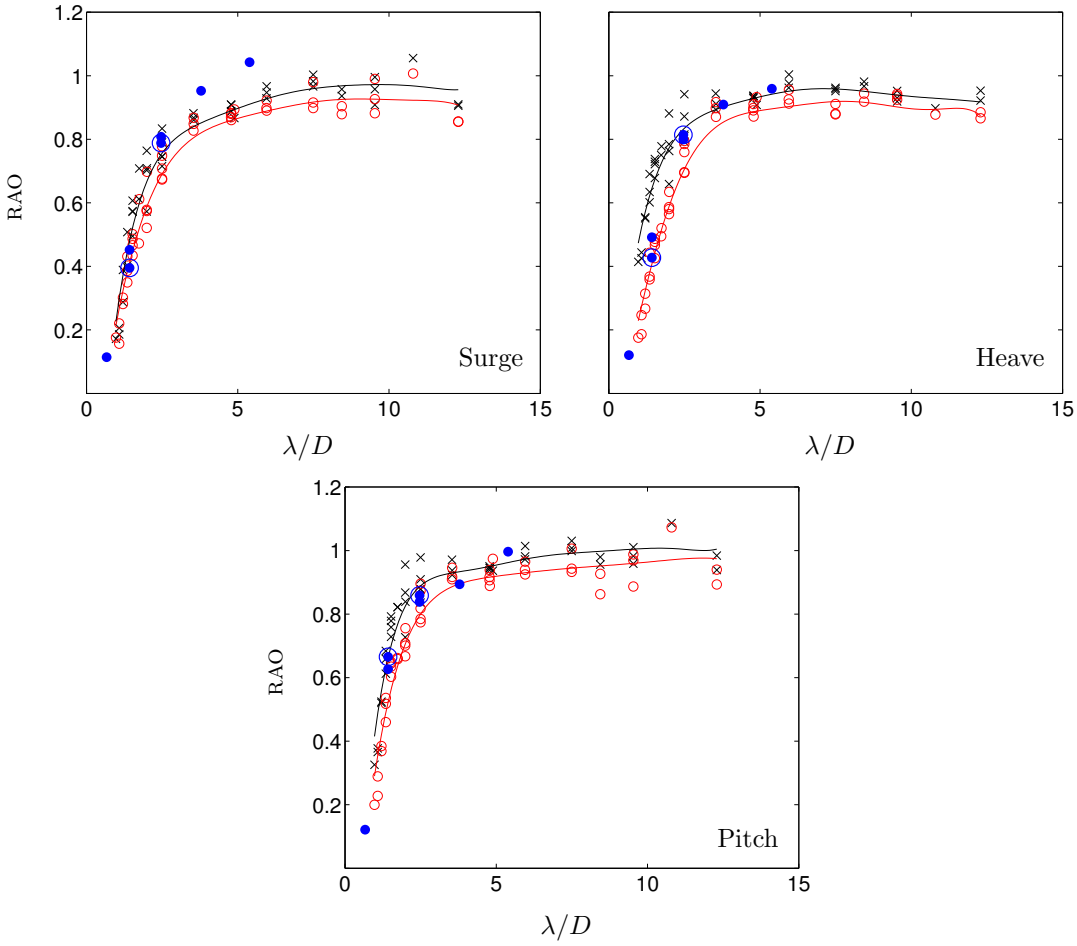

Figure 2.3.3: RAOs for Floe B (×) and Floe NB (○) for Matrix 1. Trend lines for Floe B (−) and Floe NB (−) are shown. RAOs calculted by Bennetts and Williams (2015) are also included (●). Encircled bullets denote large-amplitude tests.

Trend lines for each floe are included in Figure 2.3.3. Trend lines are derived from the mean RAOs of each floe at each incident wavelength. The `smooth` function is first used to find a best-fit curve. The `polyfit` function is then applied to generate a 7th-order polynomial approximation, $p_7(\lambda/D)$, of the best-fit curves. Trend lines are accurate to within 6% of the mean RAOs.

The concavity or relative change in gradients of trend lines is used to quantify the transition of RAOs from strongly increasing with wavelength in the short-wavelength

regime to insensitive to wavelength in the long-wavelength regime. Concavity is calculated as p_7''/p_7'. The prime symbols indicates differentiation with respect to λ/D. For Floe NB, the maximum rate of change occurs at $\lambda/D \approx 2.2$, 2.5 and 2.7, for surge, heave and pitch, respectively. For Floe B, the maximum rate of change occurs at $\lambda/D \approx 3.2$ for surge, heave and pitch. The transition between the short- and long-wavelength regimes therefore occurs when wavelengths are approximately three times the floe length. The results also indicate that the long-wavelength regime begins at shorter wavelengths for Floe NB as compared to Floe B. Murray et al. (1983) performed similar experiments on cylindrical, spherical and cubic models (constructed from paraffin wax) and also found the transition between short- and long-wavelength regimes to occur at approximately $\lambda/D = 3$. Their analysis was based comparisons of the maximum instantaneous surge and drift velocities with fluid particle velocities at the free-surface.

Bennetts and Williams (2015) also performed related wave basin experiments using a wooden disk without a barrier. RAOs calculated by Bennetts and Williams are overlaid onto Figure 2.3.3 for comparison. Note that the wooden disk had a density $\rho_b \approx 545\,\mathrm{kg\,m^{-3}}$, which is smaller than the density of our PVC floes ($\rho_b \approx 636\,\mathrm{kg\,m^{-3}}$). The thickness-diameter ratio of the wooden disk was also smaller than the PVC floe ($H/D = 3.3 \times 10^{-2}$ versus $H/D = 3.8 \times 10^{-2}$). Masson and LeBlond (1989) conducted numerical simulations of thin disks using potential-flow theory and showed that RAOs generally decrease with larger thickness-diameter ratios. The mooring system used by Bennetts and Williams also differed from our experiments. Their disks were anchored to the floor using a set of springs and a steel cable. Despite these differences, the RAOs for the wooden disk are still generally comparable with the PVC floe, especially with Floe NB for heave and pitch. Slightly larger surge RAOs are seen for the two longest wavelengths, although differences are within the range of errors of Floe NB (not shown). Minor differences can be attributed to the different thickness-diameter ratios used. Furthermore, fewer tests were conducted.

Figure 2.3.4 presents the surge RAOs as a function of wave steepness ka, using the data from the second matrix. Results for $\lambda/D = 2.50$ and $\lambda/D = 1.73$ are shown separately, in the left and right panels, respectively. RAOs of Floes B and NB are

distinguished using the same colours and symbols as in Figure 2.3.3. Surge RAOs are expressed in terms of the relative deviation from the mean RAO. The mean RAO, ⟨Surge RAO⟩, is calculated using the RAOs of both floes over all wave steepnesses. The relative deviation is therefore

$$\Delta\text{RAO} = \frac{\text{Surge RAO} - \langle\text{Surge RAO}\rangle}{\langle\text{Surge RAO}\rangle}. \tag{2.3.1}$$

Error bars in Figure 2.3.4 denote the maximum and minimum deviations from the mean RAOs.

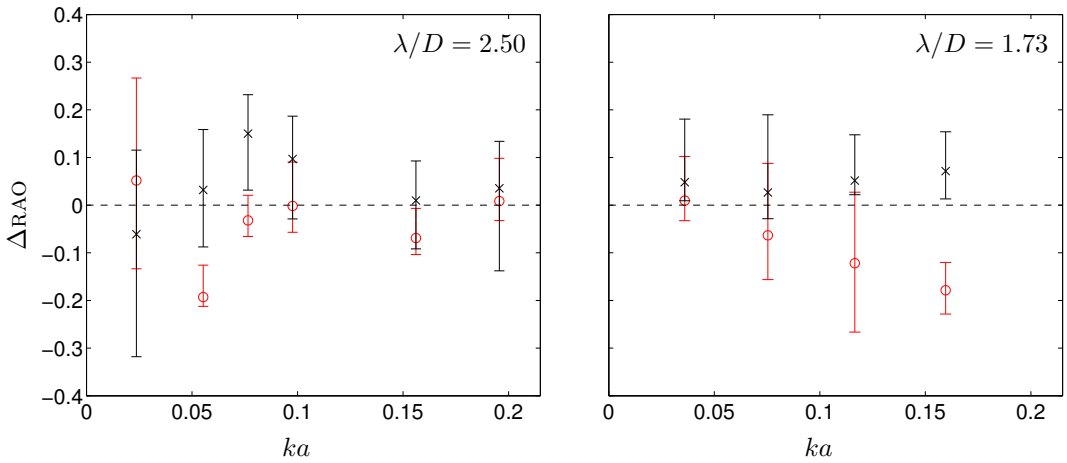

Figure 2.3.4: Deviation of surge RAO from the mean (- -) for Matrix 2, as a function of wave steepness. Incident frequency is $f = 1.25$ Hz (left panel) and 1.5 Hz (right). Results for Floe B (×) and Floe NB (○). Error-bar limits represent deviation of the RAOs corresponding to maximum and minimum individual amplitudes.

For the longer wavelength considered, $\lambda/D = 2.50$, the RAOs generally differ from the mean by less than 10%. No consistent trend is observed – this is possibly due to measurement errors e.g. random experimental errors arising from small sample sizes at each wave steepness interval (note, these are contained within the error-bar limits). For the shorter wavelength considered, $\lambda/D = 1.73$, no significant change in the RAOs of Floe B is observed when the wave steepness is increased. The RAOs for Floe NB however decrease with increasing wave steepness. Heave and pitch RAOs for Floe NB also demonstrated the same behaviour. The decrease in RAOs are probably due to the increasing effects of overwash as ka increases. The amount of overwash fluid was observed to increase as the wave amplitude, and hence wave steepness increased. Figure 2.3.5 shows an example of this occur-

ring for Floe NB (located in the foreground). The photos correspond to results from the right panel of Figure 2.3.4. Video recordings of the tests in Figure 2.3.5 can be downloaded via `https://github.com/AdelaideUniversityMathSciences/SingleFloeModels/tree/master/SingleFloeExperiments/Videos/Overwash`.

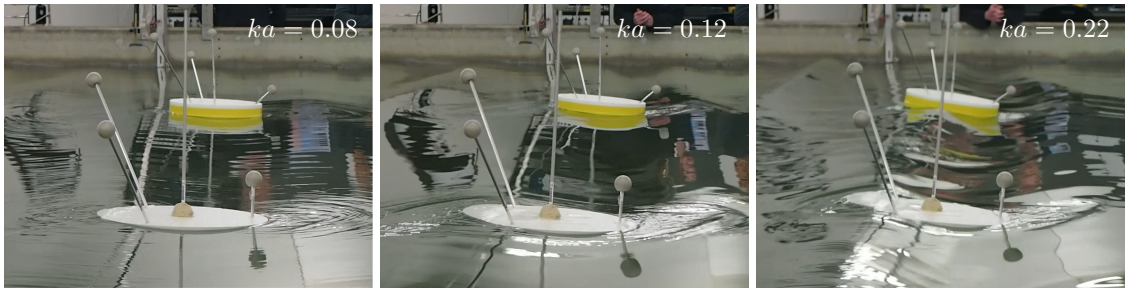

Figure 2.3.5: Example of overwash increasing with wave steepness. Wave frequency is kept constant at $f = 1.5\,\mathrm{Hz}$.

Bennetts and Williams (2015) also reported similar decreases in RAOs in the short-wavelength regime. Large-amplitude tests were conducted for $\lambda/D = 1.42$ and 2.46, by doubling the incident wave amplitude. Whilst no significant changes in RAOs were observed for the larger of the two wavelengths, when $\lambda/D = 1.42$, the surge and heave RAOs decreased by 0.057 and 0.064 units respectively. Contrary to this trend is the pitch RAO, which increased by 0.039 units. It should be noted that Bennetts and Williams used two incident amplitudes only, and steepness for the largest amplitude was relatively low, $ka \approx 0.11$.

2.3.2 Drift velocity

Drift velocities are calculated as the maximum gradient of the drift signal over the free-drift interval. Due to the nature of the mooring system, the gradient of the drift signal decreases when the tether engages. Therefore the maximum gradient will give the best approximation of the drift velocity for an unrestrained floe. Drift velocities are only calculated for tests which have clearly identifiable free-drift intervals. In general, tests with wavelengths less than $\lambda/D \approx 5$ fall under this category.

Figure 2.3.6 demonstrates how drift velocity is calculated. In this example, $f = 1.25\,\mathrm{Hz}$ (corresponding to $\lambda/D \approx 2.5$) and $a = 65.2\,\mathrm{mm}$. The free-drift interval spans $t \approx 20\,\mathrm{s}$ to $25\,\mathrm{s}$. Drift is extracted from the full signal using the `smooth`

function, with a span of 0.1. The location of the maximum gradient is indicated by a red bullet. The calculated drift velocity in this example is $v_d = 0.11\,\mathrm{m\,s^{-1}}$.

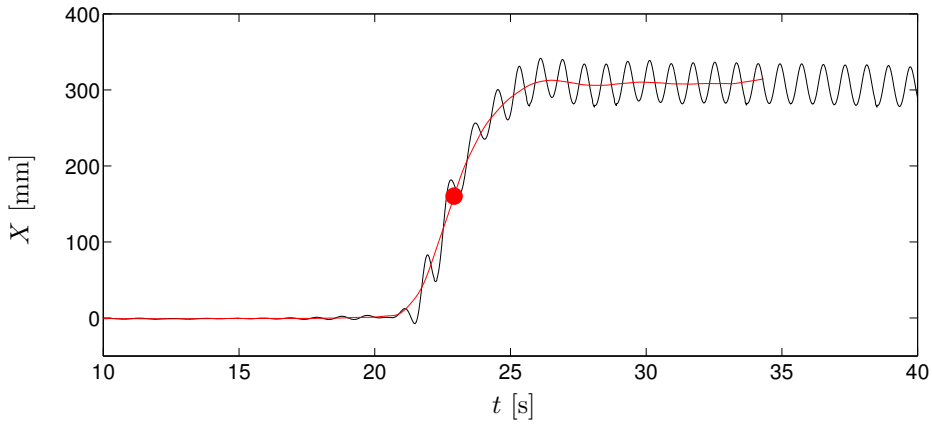

Figure 2.3.6: Drift velocity is calculated by taking the maximum gradient (•) of the drift signal (−), which is isolated from the x-displacement of the floe (−).

Figure 2.3.7 shows the drift velocities v_d for Floes B and NB, as a function of wave steepness ka. Data from both matrices are considered here. Drift velocities are nondimensionalised with respect to the phase velocity $c = f\lambda$, as was done by Huang et al. (2011) and McGovern and Bai (2014).

The drift velocities for both floes follow an increasing relationship with respect to ka. In general, drift velocities for Floe NB are smaller than that of Floe B. Differences increase with wave steepness. The increasing divergence is attributed to the increase in overwash, which damps drift. This diverging behaviour may also be compounded by edge effects at the fluid-barrier interface of Floe B. The edge barrier increases the vertical surface area in contact with fluid when wave steepness are sufficiently large. This results in larger wave forces exerted on the floe.

In Figure 2.3.7, drift velocities are compared with experimental results from Huang et al. (2011) and McGovern and Bai (2014). Huang et al. recorded the drift velocities of paraffin wax plates of different shapes and thicknesses in wave steepnesses ranging from $ka = 0.04$ to 0.15. Drift velocities in Figure 2.3.7 are for square plates of thickness to length quotient, $H/D_l = 0.225$ and mass 1.7 kg. McGovern and Bai performed similar experiments on a square (polyethylene) plate of $H/D_l = 0.167$ and mass 4 kg, in wave steepnesses from $ka = 0.02$ to 0.31. No edge barriers were used in either experiments. In comparison, our floes were thinner at $H/D = 0.0375$ and lighter with a mass of 1.2 kg, and were tested in wave steepnesses $ka = 0.013$ to 0.3.

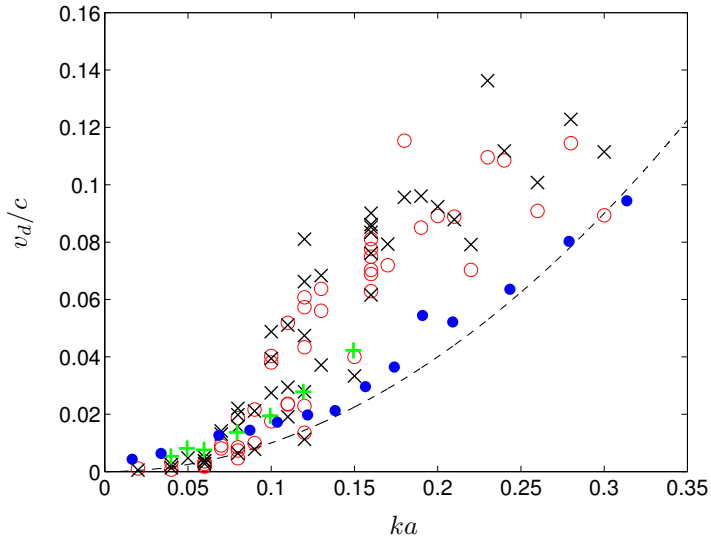

Figure 2.3.7: Drift velocities v_d of Floe B (×) and Floe NB (○) from Matrix 1 and 2, with respect to the phase velocity c, as a function of wave steepness ka. Stokes drift (- -) is overlaid. Results from Huang et al. (2011) (+) and McGovern and Bai (2014) (●) are shown for comparison.

Bai et al. (2016) compared the results from the two previous experiments against Stokes drift velocity v_s, which is calculated using the formula (Phillips, 1977)

$$v_s = \omega k a^2 \coth kh \coth 2kh, \tag{2.3.2}$$

and reported that the drift of McGovern and Bai is approximately equivalent to Stokes drift over the range of wave steepnesses considered. The drift of Huang et al. closely follows McGovern and Bai for wave steepnesses less than 0.1, but begins to increasingly diverge as ka increases.

Similar to Huang et al., the drift of Floes B and NB are correlated to Stokes drift when $ka < 0.1$, but diverges with increased wave steepnesses. For wave steepnesses less than $ka = 0.1$, the average drift velocity is 1.85 times v_s for Floe B, and 1.45 times v_s for Floe NB. For wave steepnesses larger than $ka = 0.1$, the average drift velocity is 2.62 times v_s for Floe B, and 2.46 times v_s for Floe NB. The difference in drift velocities in steeper waves is likely related to their masses. Floes B and NB have the smallest masses ($m = 1.2\,\mathrm{kg}$), therefore least inertial resistance to drift. In contrast, McGovern and Bai's floe has the greatest mass ($m = 1.7\,\mathrm{kg}$) and smallest drift velocities. The effects of overwash in steeper waves is also likely to increase the mass of the floe and further decrease drift velocities.

2.4 Summary

Laboratory wave basin experiments were conducted on two solitary circular floes, to investigate wave-induced motions in regular incident waves. Wavelengths ranging from 1 to 12 times the floe diameter, and wave amplitudes corresponding to wave steepnesses between 0.01 to 0.26, were tested. An edge barrier was installed on one floe to investigate the effects of overwash. Results for dominant oscillatory motions are presented in terms of nondimensional response amplitude operators. Drift motions are also investigated.

The key findings are summarised as follows:

1. Floes behave like fluid particles in wavelengths approximately 3 times larger than the floe diameter. This interval defines the transition between the short- and long-wavelength regimes.

2. Surge, heave and pitch amplitudes for both floes are generally linear with respect to the incident wave amplitude, except when overwashing occurs.

3. Overwash predominantly occurs in the short-wavelength regime, and increases with increasing wave steepness. Overwash suppresses the surge, heave and pitch motions of the floe without a barrier in very short waves. The floe with a barrier was insensitive to changes in the wave steepness.

4. The floe without a barrier has smaller RAOs than the floe with a barrier. Differences are largest in the short-wavelength regime.

5. Drift velocities for both floes increase with wave steepness.

6. In wave steepnesses less than 0.1, drift velocities of both floes are approximately equal to Stokes drift. In larger wave steepnesses, drift velocities are much larger than Stokes drift.

7. The floe without a barrier has smaller drift velocities compared to the floe with a barrier, in wave steepnesses larger than 0.1. This is likely due to edge-effects at the barrier, and the influence of overwash.

8. In wave steepnesses larger than 0.1, drift velocities of both floes were much larger than that of thin plates tested in other similar experiments. We related

this observation to the increase of drift velocity with decreasing floe mass.

Chapter 3

The slope-sliding model

The first theoretical model we will consider is based on slope-sliding theory. Slope-sliding theory assumes that incident wavelengths are much longer than the length of a floating body, such that wave scattering can be neglected (Rumer et al., 1979; Marchenko, 1999). This phenomenon was observed in the single-floe experiments (see Figure 2.3.2). The incident wavefield is therefore assumed to remain unmodified during its interaction with small bodies.

In this chapter, waves are defined to be regular, i.e. planar, monochromatic and periodic in time. We assume that waves are sinusoidal, therefore on an xz-plane, the incident wave profile (vertical displacement of the free-surface) can be expressed as

$$z = \eta(x,t) = a\sin(kx - \omega t). \tag{3.0.1}$$

Figure 3.0.1 shows the general wave parameters on a cross-sectional diagram of a wave-floe system. The incident wave is parameterised by its wavelength λ and wave amplitude a. Wavelengths may also be expressed in terms of corresponding wave frequencies f, or wavenumbers $k = 2\pi/\lambda$ (not shown). The latter is associated to f according to the dispersion relation $k \tanh kh = \omega^2/g$, where $\omega = 2\pi f$ is the angular wave frequency, h is the water depth, and $g = 9.81\,\mathrm{m\ s^{-2}}$ is the gravitational constant.

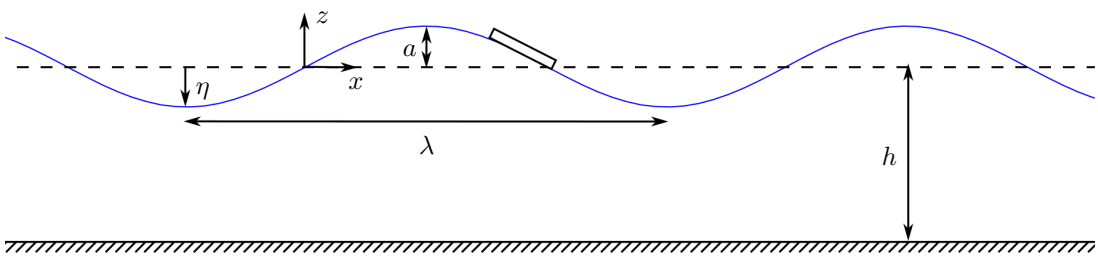

Figure 3.0.1: General wave parameters.

3.1 Equation of motion

In the slope-sliding model, a one-dimensional equation of motion is derived by considering the horizontal motions and wave forces inline with the direction of the propagating wave. The motions of a floating body, or in this case a floe, are calculated at its centre of mass. The location of the centre of mass on an x-coordinate system is denoted as $X(t)$ at time t.

The equation of motion of a floe in the x-direction is

$$m(1+c_m)\frac{dV}{dt} = -mg\left[\frac{\partial \eta}{\partial x}\right]_{x=X} + \rho c_d W|\widehat{V}|\widehat{V}. \tag{3.1.1}$$

The term on the left-hand side of (3.1.1) represents the inertial force, which is proportional to the mass m and the acceleration (i.e. time derivative of the velocity V) of the floe.

The first term on the right-hand side is the gravitational force, which is a function of the slope of the wave profile (i.e. x derivative of η), at the horizontal location of the floe, i.e. at $x = X(t)$. From Equation (3.0.1), the slope of the wave profile is

$$\frac{\partial \eta}{\partial x} = ka\cos(kx - \omega t). \tag{3.1.2}$$

The second term on the right-hand side of (3.1.1) is the drag force, which represents the resistance between the fluid and the floe. Here, ρ is the fluid density, and W is the wetted surface area of the floe. If a floe is represented as a disk, and assuming that it moves on the water surface, then $W = \pi R^2$. The drag force is also a function

of the relative velocity of the floe $\widehat{V} = V_w(t) - V(t)$, where $V(t)$ is the velocity of the floe, and $V_w(t)$ is the velocity of a fluid particle on the water surface at the location of the floe. The horizontal fluid velocity V_w is calculated from (3.0.1). For a regular wave propogating in the positive x-direction, the x-coordinate of a fluid particle at the free-surface will be $\chi(x,t) = a\cos(kx - \omega t)$. For finite-depth water waves, χ is scaled by a factor of $\coth kh$ to account for elliptical orbits of fluid particles. The horizontal velocity is calculated by taking the time derivative of χ, i.e.

$$V_w(x,t) = \omega a \sin(kx - \omega t) \coth kh. \tag{3.1.3}$$

Equation (3.1.1) contains two hydrodynamic parameters. The coefficient c_m represents the added mass coefficient. Newman (1977), Mei et al. (2005) and others describe the added mass as a virtual hydrodynamic inertia experienced by a body moving through a fluid, and is proportional to the amount of fluid accelerated with the submerged body. The coefficient c_d is the drag coefficient. This parameter determines the magnitude of resistive forces at the fluid-floe interface due to parasitic drag forces such as skin friction and form drag (Madsen and Bruno, 1987). The effects of c_m and c_d on floe motions will be discussed in § 3.4. Values for c_m and c_d are determined through empirical means using results from the single-floe experiments in Chapter 2. Model-data comparisons and analyses are described in § 3.6.

3.2 Solution method

System (3.1.1) is a nonlinear second order ordinary differential equation (ODE), which is solved for the unknown quantities $X(t)$ and $V(t)$. The MATLAB function `ode45` is implemented to solve the ODE. This numerical solver applies a variable step size fourth and fifth-order Runge-Kutta integration method.

In (3.1.1), the absolute function $|\widehat{V}|$ presents a removable discontinuity, which cannot be integrated by `ode45`. To alleviate this problem, $|\widehat{V}|$ is replace by the continuous function $\widehat{V}\tanh(100\widehat{V})$.

To solve for $X(t)$ and $V(t)$, wave conditions, floe parameters and hydrodynamic

coefficients are first defined. In the slope-sliding model, we are solving an initial value problem, therefore simulation parameters such as the time step and initial conditions (X and V at $t = 0$) must also be specified. The effect of initial conditions on the solution will be discussed in § 3.3.

For example problems in this chapter, we will use floe and wave parameters corresponding to those in the single-floe experiments of Chapter 2, i.e. floe diameter $D = 400\,\mathrm{mm}$, floe thickness $H = 15\,\mathrm{mm}$, floe density $\rho_b = 636\,\mathrm{kg\,m^{-3}}$, and $\lambda/D = 0.97$ to 12.2. The fluid density will be taken as $\rho = 1000\,\mathrm{kg\,m^{-3}}$, and the mean water depth $h = 830\,\mathrm{mm}$. The MATLAB code used to solve the example problem can be obtained via `https://github.com/AdelaideUniversityMathSciences/SingleFloeModels/tree/master/SlopeSliding`.

Figure 3.2.1 shows an example of the solution generated by `ode45` (left panel, solid curve). Here, the displacement of the floe is presented as a function of time. The simulation parameters for this example are $a = 20\,\mathrm{mm}$, $\lambda = 2\,\mathrm{m}$, and the coefficients $c_m = c_d = 0$. Initial conditions are defined as $X(0) = V(0) = 0$.

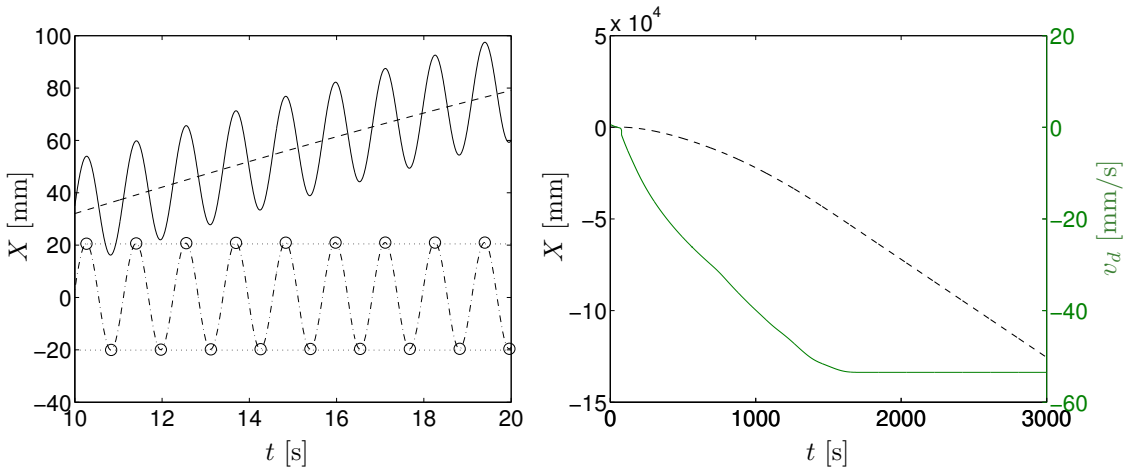

Figure 3.2.1: Left panel: Example of a floe's displacement predicted by the slope-sliding model, over a 10 s interval. The full solution (−) is the sum of surge (-·-) and drift (--). Right panel: Drift and drift velocity v_d (−) over an expanded time interval.

Translations in the x-axis are a combination of surge and drift. Surge and drift are separated using a numerical smoothing method identical to the one applied in the single-floe experiments (see § 2.2.6). The left panel of Figure 3.2.1 illustrates the decomposition of surge and drift. The dot-dashed and dashed curves are surge and

drift, respectively.

Surge motions are quantified using the same procedure described in § 2.2.6. Drift is quantified in terms of the drift velocity, v_d, which is calculated by finding the gradient of the drift signal. The right panel of Figure 3.2.1 shows the drift signal over an enlarged time scale. The initial drift velocity changes with time, but settles at a constant steady-state value after approximately 1700 seconds. In this chapter, v_d will be defined as the long term steady-state drift velocity.

3.3 Phase space

The notation $Q(t) = kX - \omega t$ is adopted, so that Equation (3.1.1) can be expressed as an autonomous dynamical system in terms of V and Q,

$$\frac{dV}{dt} = \frac{-mgka\cos Q + \rho c_d W|\widehat{\mathcal{V}}|\widehat{\mathcal{V}}}{m(1+c_m)}, \tag{3.3.1}$$

where $\widehat{V}(t) \equiv \widehat{\mathcal{V}}(V,Q) = \omega a \sin Q \coth kh - V$, and

$$\frac{dQ}{dt} = kV - \omega. \tag{3.3.2}$$

The solution of the dynamical system is defined on a cylindrical surface, with the azimuthal coordinate $Q \in [0, 2\pi]$, and vertical coordinate $V \in \mathbb{R}$.

The left panel of Figure 3.3.1 shows the phase space when $c_m = c_d = 0$, $a = 50\,\text{mm}$ and $\lambda = 6\,\text{m}$. In this example problem, the solution has two fixed points, which are located at $(Q, V) = (\pi/2, \omega/k)$ and $(3\pi/2, \omega/k)$. These two fixed points are found by solving Equations (3.3.1) and (3.3.2) when $dV/dt = dQ/dt = 0$. This represents surfing solutions, where V and Q do not change in time.

The fixed point at $(3\pi/2, \omega/k)$ is a centre equilibrium node. All orbits around the node are concentric and periodic. Figure 3.3.1 shows an example of a closed concentric orbit in green. The fixed point at $(\pi/2, \omega/k)$ is a saddle node. Stable and unstable manifolds are indicated by arrows pointing towards and away from the node, respectively. To generate solutions for unstable manifolds, an initial condition close to the saddle point is selected, then applied to the ODE solver. Similarly,

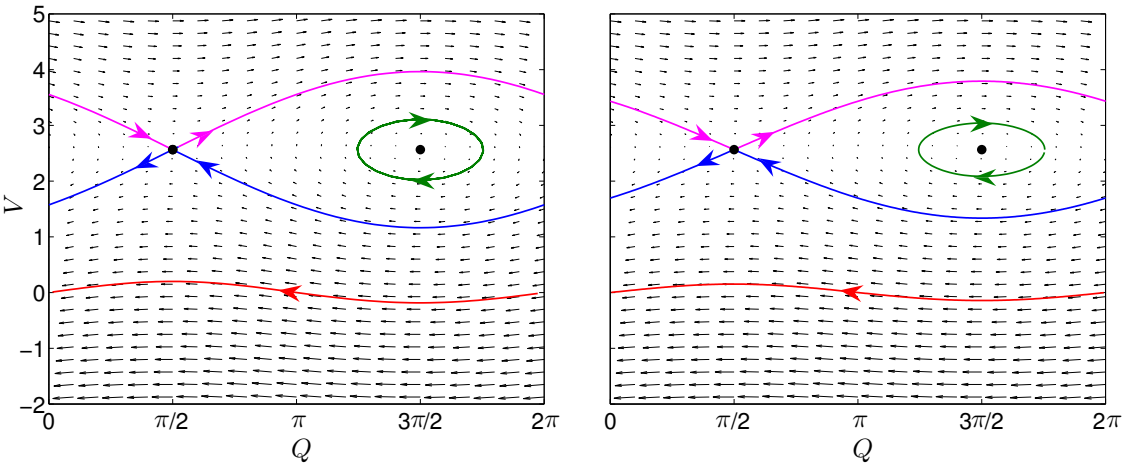

Figure 3.3.1: Phase diagrams for zero drag case when $c_m = 0$ (left panel) and $c_m = 0.3$ (right).

for stable manifolds, a point close to the saddle node is selected, however this time Equation (3.3.1) is integrated backwards in time. The stable and unstable manifolds can also be divided into upper and lower homoclinic connections, i.e. trajectories which join a saddle node to itself. Figure 3.3.1 shows the upper and lower connections in magenta and blue, respectively.

All trajectories below the lower homoclinic connection are closed periodic orbits. These orbits represent surge and drift. The integral of V over one period gives the displacement from which surge amplitude may be deduced. The difference between the period of each orbit and the incident wave period represents drift. These solutions are relevant to our investigation.

An example of a closed orbit is shown in red. This orbit is obtained when $V(0) = Q(0) = 0$. The periodicity of these orbits can be proven analytically using Equations (3.3.1) and (3.3.2). For simplicity, all time independent constants here are taken to be unit valued. For this example case, Equations (3.3.1) and (3.3.2) reduces to

$$\frac{dV}{dt} = \frac{d^2Q}{dt^2} - \cos Q \tag{3.3.3}$$

The analytic solution of this second-order differential equation is found using MATLAB's `dsolve` package, which returns the solution

$$Q(t) = \frac{1}{2}\left(\pi - 4\ \mathrm{am}\left(\frac{1}{2}\sqrt{(c_1-2)(t+c_2)^2}\ \middle|\ \frac{4}{c_1-2}\right)\right), \tag{3.3.4}$$

where c_1 and c_2 are arbitrary constants which are determined by specifying the initial conditions. The function "am" is a Jacobi amplitude function, which is periodic in time. The periodicity of $Q(t)$ implies that dQ/dt and $V(t)$ are also periodic. The zero drag case is analogous to a nonlinear ideal pendulum system (e.g. Hirsch et al., 2013, § 9.2). In an ideal system no friction exists. This produces a phase plane with level curves above and below the homoclinic manifolds. Since solutions here are periodic, surge and drift motions will be insensitive to small changes in the initial conditions.

The right panel of Figure 3.3.1 shows the phase space when $c_d = 0$ and $c_m = 0.3$. When a non-zero added mass coefficient is introduced, scaling occurs on the vertical axis. Periodic orbits and homoclinic connections decrease in amplitudes. However fixed points remain at $(\pi/2, \omega/k)$ and $(3\pi/2, \omega/k)$. For orbits below the lower homoclinic connection, the decrease in amplitude translates to a smaller surge response. By increasing the added mass, the overall inertia of the system increases. This results in a suppression of surge motions.

When drag is introduced, fixed points are shifted horizontally towards each other. Figure 3.3.2 shows the phase space when $c_d = 3 \times 10^{-4}$ and $c_m = 0$. All other input parameters are unchanged. The vertical coordinate of the fixed point remains at $V = \omega/k$, while the azimuthal coordinate shifts to

$$Q = \arccos\left(\frac{\rho c_d W |\widehat{\mathcal{V}}| \widehat{\mathcal{V}}}{mgka}\right). \tag{3.3.5}$$

The left-hand fixed point remains as a saddle node, however the right-hand fixed point now becomes a stable spiral. All trajectories below the lower manifolds tend towards a limit cycle, which is shown in red. This suggests that a steady-state surge and drift response will occur after a sufficient amount of time. (Note, this was demonstrated for drift in the right panel of Figure 3.2.1.) The limit cycle is comparable to the periodic orbit in Figure 3.3.1. Grotmaack and Meylan (2006) performed a similar analysis using non-zero drag and obtained analogous results. They also considered another case when the drag coefficient was further increased until all equilibrium points vanished in a saddle-node bifurcation. In this scenario, all solutions tend to the limit cycle.

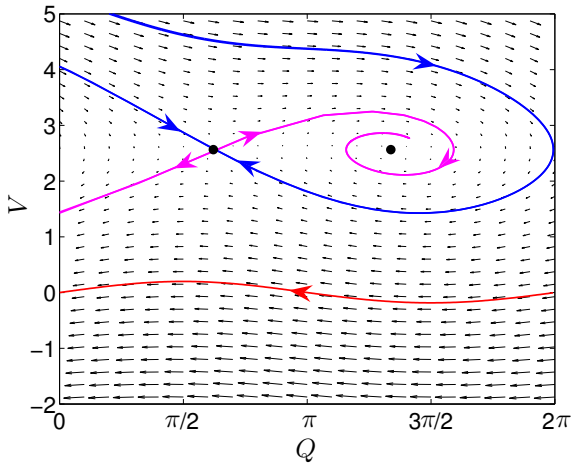

Figure 3.3.2: Phase diagram when $c_d = 3 \times 10^{-4}$.

3.4 Drag and added mass coefficients

3.4.1 Effect on surge

Figure 3.4.1 shows the surge RAOs as a function of the incident wavelength, for various combinations of drag and added mass coefficients. The incident wavelength λ is nondimensionalised with respect to the floe diameter D to indicate the wavelength regime. Three added mass coefficients ranging from $c_m = 0$ to 0.2 are considered. These values are chosen in consideration of Luk (1987), who applied potential-flow theory to calculate the added mass coefficient of a circular disk in surge motion. Luk found that a disk with $h_f/h = 0.8$, where h_f is the distance from the sea floor to the base of the disk, had added mass coefficients of less than 0.12, over wave frequencies between 0 to 4.5 Hz. Luk also reported that the added mass decreases with increasing values of h_f/h. In other words, for a thin floating body, having a small draft to water depth ratio, the added mass coefficient will be small. In the single-floe experiments, $h_f/h \approx 1$, therefore the added mass coefficient is expected to be relatively small.

When $c_m = 0$, the slope-sliding model predicts that the surge RAO tends to 1 in long waves, i.e. for $\lambda/D > 4$, approximately. This means that in long waves, the horizontal trajectory of the floe will be equivalent to that of a fluid particle at the free-surface. In shorter waves, the surge RAO marginally decreases with decreasing wavelength. At $\lambda/D = 1$, the surge RAO is approximately 0.9. This behaviour also

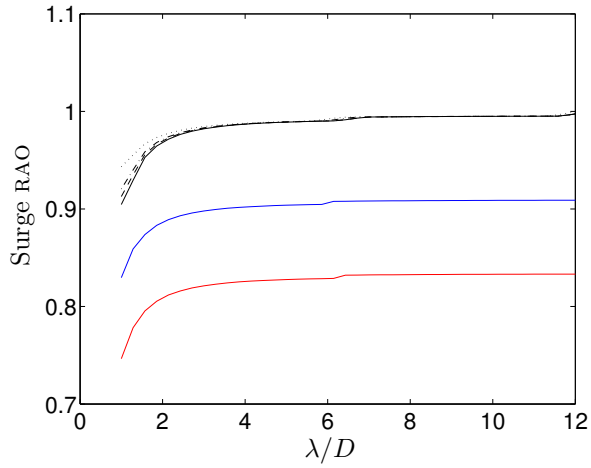

Figure 3.4.1: Effect of the drag and added mass on surge. Three added masses and four drag coefficients are considered: $c_m = 0$ (black), 0.1 (blue), 0.2 (red); $c_d = 0$ (solid curve), 0.005 (dashed), 0.02 (dot-dashed), 0.1 (dotted). Surge RAOs are insensitive to drag.

occurs for the other two added masses.

When the added mass is increased, the RAOs across all wavelengths decreases. In long waves, the RAOs tend to 0.91 and 0.83, for $c_m = 0.1$ and 0.2, respectively. This confirms the results in § 3.3, which show a decrease in the amplitude of the surge velocity when an added mass was introduced. The RAO limits in Figure 3.4.1 are observed to be approximately equal to $1/(1 + c_m)$.

Figure 3.4.1 also shows the effect of drag on surge. Madsen and Bruno (1987) measured the drag coefficients of actual ice floes during field experiments in the Bering Sea, and reported values of $O(10^{-2})$. In this analysis, four drag coefficients ranging from $c_d = 0$ to 0.1 are investigated when $c_m = 0$. Increases in c_d produce no significant change in surge RAOs. This behaviour also occurs for other values of c_m (not shown in Figure 3.4.1) when using the same drag coefficients.

3.4.2 Effect on drift

Grotmaack and Meylan (2006) calculated the drift velocity and considered the effect of varying drag. They calculated the long-term drift velocity as

$$v_d = \frac{1}{\tilde{t}} \int_0^T V(t) \;\; \mathrm{d}t, \tag{3.4.1}$$

where $\tilde{t}$ is the time it takes for a floe to travel from one wavecrest to another wavecrest and $T = 1/f$ is the wave period. In their study, two wave frequencies were considered and the drift velocities were found for a range of drag coefficients. All parameters in their study were nondimensionalised. The two nondimensional wave frequencies they used correspond to approximately $\lambda/D = 1.3$ and 5 in the example problem here. Likewise, the drag coefficients they considered correspond to $c_d = 0$ to 2. Grotmaack and Meylan found that the drift velocity increases when the drag coefficient increases, and changes to the drift velocity were larger in short waves and smaller in longer waves. Drift velocities were however only marginally affected by the drag coefficient. The variation in v_d over the range of drag coefficients was $\mathrm{O}(10^{-3})\,\mathrm{m\,s^{-1}}$.

Figure 3.4.2 shows the drift velocities as functions of nondimensional wavelength (left panel), and wave steepness (right panel), when $a = 20\,\mathrm{mm}$. Four drag coefficients between $c_d = 0$ and 2, and two added mass coefficients, $c_m = 0$ and 0.2, are considered. For both values of c_m, the variation in v_d across the range of drag coefficients considered is also $\mathrm{O}(10^{-3})\,\mathrm{m\,s^{-1}}$ or less for all wavelengths and wave steepnesses considered.

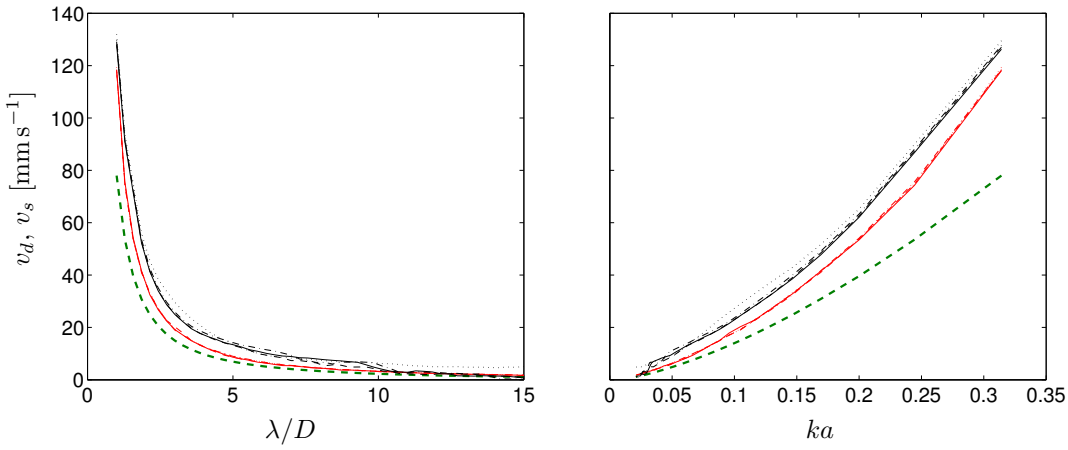

Figure 3.4.2: Effect of drag and added mass on drift velocity. Drift velocity is expressed as a function of nondimensional wavelength (left panel) and wave steepness (right panel). Two added masses and four drag coefficients are considered: $c_m = 0$ (black) and 0.2 (red); and $c_d = 0$ (solid curve), 0.1 (dashed), 0.5 (dot-dashed) and 2 (dotted). Stokes drift velocity is overlaid (- -).

Figure 3.4.2 also shows minimal changes to the drift velocity when different added mass coefficients are applied. Drift velocities for $c_m = 0$ are slightly larger than

that of $c_m = 0.2$. However the average difference between the two added masses are small, at $\mathrm{O}(10^{-3})\,\mathrm{m\,s^{-1}}$. The difference is slightly larger in short waves ($\lambda/D < 3$, approximately), at $\mathrm{O}(10^{-2})\,\mathrm{m\,s^{-1}}$, but decreases with increasing wavelength. The drift velocities for all added mass and drag coefficients tend to zero in the long-wavelength limit.

In addition, Figure 3.4.2 compares the slope-sliding model's predictions of drift with the Stokes drift velocity, v_d, using Equation (2.3.2). Drift velocities for all combinations of added mass and drag overestimate Stokes drift. Differences in drift velocities are largest when λ/D is small (for example, $v_d - v_s = \mathrm{O}(10^{-2})\,\mathrm{m\,s^{-1}}$ when $\lambda/D = 1$), but decrease as wavelengths increase. The Stokes drift velocity also tends to zero in the long-wavelength limit

3.5 Long-wavelength approximation

In § 3.4 it was found that in long waves, surge RAOs tend to 1 when $c_m = 0$, or approximately $1/(1 + c_m)$ if the added mass is non-zero. This is regardless of the value of c_d.

The long-wavelength limit for surge can be proved analytically by considering the following. In the long-wavelength limit, the slope-sliding model predicts that drift velocities tends to zero (for all combinations of c_m and c_d). This was shown in Figure 3.4.2. At $\lambda/D = 6$, the drift velocity is $\mathrm{O}(10^{-3})\,\mathrm{m\,s^{-1}}$. This means that surge is the dominant motion in this regime. Since surge does not depend on drag, the drag term in Equation (3.1.1) may be omitted such that

$$\begin{aligned}(1 + c_m)\frac{dV}{dt} &= -g\left[\frac{\partial \eta}{\partial x}\right]_{x=X} \\ &= -gak\cos(kX - \omega t).\end{aligned} \tag{3.5.1}$$

The slow drift velocity equates to the condition $|kX| \ll 1$. Therefore the above equation may also be expressed as

$$(1 + c_m)\frac{dV}{dt} = -gak\cos\omega t + \mathrm{O}(kX). \tag{3.5.2}$$

If zero initial velocity is assumed, (3.5.2) can be integrated to give

$$V(t) = \frac{-gak\sin(\omega t)}{\omega(1+c_m)} + \mathrm{O}(kX). \tag{3.5.3}$$

Integrating again, and considering only the leading orders in kX, the displacement of the floe is

$$X(t) = \frac{gak\cos(\omega t)}{\omega^2(1+c_m)} = \frac{a\coth(kh)\cos(\omega t)}{1+c_m}, \tag{3.5.4}$$

after applying the dispersion relation $k\tanh kh = \omega^2/g$. The surge amplitude is therefore

$$a_s = \frac{a\coth(kh)}{1+c_m}, \tag{3.5.5}$$

hence the surge RAO predicted by the slope-sliding model will tend to $1/(1+c_m)$ in the long-wavelength limit. Figure 3.5.1 compares the leading-order displacement against the full solution when $\lambda/D = 6$, $a = 20\,\mathrm{mm}$ and $c_m = c_d = 0$. The figure shows that the long-wavelength approximation for surge is accurate.

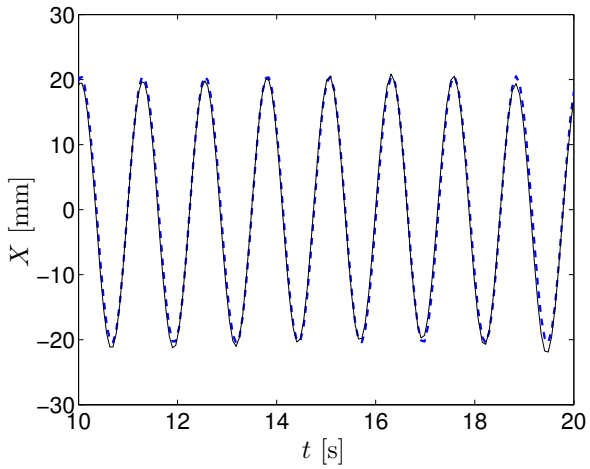

Figure 3.5.1: Full numerical solution of the slope-sliding model (−) versus long-wavelength approximation of surge (- -).

3.6 Comparison with single-floe experiments

Figure 3.6.1 shows the surge RAOs predicted by the slope-sliding model in comparison to data from single-floe experiments, as given in Figure 2.3.3. RAOs are plotted as functions of nondimensional wavelength. Two added mass coefficients, $c_m = 0$ and 0.1, are considered in the figure. Drag coefficients are set to zero, since surge is

insensitive to drag. Experimental data from Figure 2.3.3 are presented in terms of the mean RAOs, with respect to the incident wavelength, i.e. RAOs of both floes (with and without edge barriers) are grouped according to incident wavelength. Symbols denote the group means of each floe. Error bars indicate the overall maximum and minimum RAOs of each wavelength group.

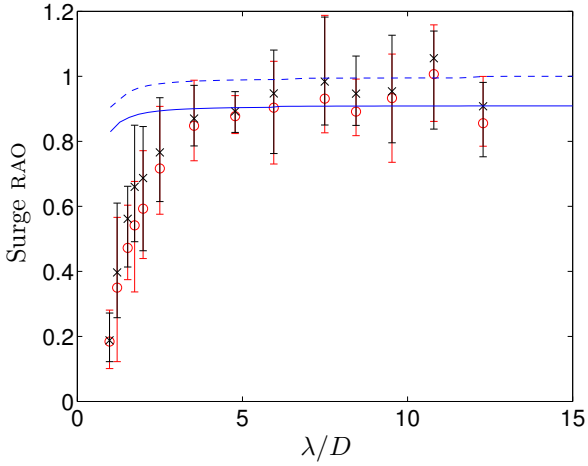

Figure 3.6.1: Comparison of surge RAOs from single-floe experiments (symbols) and slope-sliding model (blue curves) when $c_d = 0$, and $c_m = 0$ (- -) and 0.1 (−). RAOs for Floe B (×) and Floe NB (○), and their respective error bars are shown.

The slope-sliding model shows good agreement with Floes B and NB in the long-wavelength regime ($\lambda/D > 3$) only. Recall that the differences in RAOs of Floes B and NB are small in long wavelengths. The average difference between mean RAOs of the two floes is less than 0.04 units (4%), in the long-wavelength regime. When $c_m = 0$, surge responses from the slope-sliding model lie within the error limits of Floe B and NB in wavelengths of $\lambda/D \geq 5.95$. The average difference between the model and the mean RAOs, when $\lambda/D \geq 3$, is 7.8% for Floe B, and 11.2% for Floe NB. Better agreement is achieved by increasing the added mass to 0.1. When this value of c_m is used, theoretical predictions lie within the error limits of Floe B and NB in wavelengths $\lambda/D \geq 2.5$. Average differences between the model and the mean RAOs, when $\lambda/D \geq 3$, are 4.8% for Floe B, and 4.2% for Floe NB.

The slope-sliding model does not capture the strong dependence of surge RAOs on incident wavelengths in the short-wavelength regime. Model predictions of surge increasingly deviate from the experiments as the wavelength decreases. At the shortest wavelengths considered ($\lambda/D = 0.98$), the model overpredicts the surge RAO by more than 0.64 units.

3.7 Summary

The slope-sliding model was proposed to predict the surge and drift motions of an ice floe. The equation of motion was derived, using the assumptions of small amplitude and long waves. In the model, floes are driven by a gravitational force, due to the slope of waves, and resisted by a drag force. The slope-sliding model has two semi-empirical hydrodynamic coefficients for added mass and drag. Their effects on the solution were investigated.

General solutions to the dynamical system were presented on a phase plane. Solutions were shown to approach either a surfing solution, in which the floe travels with the wave, or a periodic orbit. The behaviour of the solution was dependent on the values of the two hydrodynamic coefficients. The added mass coefficient determined the amplitude of the floe's velocity, and the drag coefficient determined the existence and locations of equilibrium nodes. Relevant solutions for surge and drift were obtained when small initial velocities were used. These motions were insensitive to small changes in initial conditions.

Surge motions were quantified as response amplitude operators (RAOs) and presented as functions of incident wavelength. Surge RAOs were generally insensitive to changes in incident wavelength, and approached an asymptotic value in the long-wavelength limit.

The effects of drag and added mass on surge and drift were investigated. Surge RAOs were shown to be inversely proportional to the magnitude of added mass. There were no significant changes in RAOs when drag was varied. Drift velocities were marginally sensitive to drag, and decreased slightly with increasing added mass. Drift velocities monotonically decreased with increasing incident wavelength. In the long-wavelength limit, drift velocities approached zero for all combinations of added mass and drag.

An analytical long-wavelength approximation for surge was derived from the slope-sliding model, using the assumptions of small drift velocity. The approximate solution confirmed the numerical long-wavelength limit for surge.

Finally, theoretical results for surge were compared against data from the single-

floe experiments. Model-data comparisons were best in the long-wavelength regime (when wavelengths are longer than three times the floe diameter) and when an added mass coefficient of 0.1 was applied. These findings suggest the slope-sliding model is not appropriate for modelling the motions of floes in the short-wavelength regime.

Chapter 4

The potential-flow model

The second theoretical model for wave-induced motions of single floating bodies is introduced in this chapter. This model is based on linear potential-flow theory. Much of the work in this chapter is derived from Linton and McIver (2001), Dean and Dalrymple (1991, Chapters 2 and 3) and Mei et al. (2005, Chapter 8), who describe the fundamental concepts of potential-flow theory and formulate problems for general cases of waves interacting with an arbitrarily shaped floating body. Linton and McIver also presents solution methods, which we will apply numerically to solve the problem of a solitary floe in waves.

4.1 Formulating the boundary value problem

Consider the water-floe system in Figure 4.1.1. In the slope-sliding model, a one-dimensional system was adopted to define floe motions on a horizontal x-axis. Here, we adopt a two-dimensional Cartesian plane (x, z) to represent the water-floe domain. A floe is represented as a rectangular cross-section on the xz-plane. The x- and z-coordinates define horizontal and vertical locations, respectively. The z-axis is directed upwards, with $z = 0$ at the equilibrium water surface, and the x-axis points in the same direction as the oncoming incident wave. The origin of the coordinate system lies at the intersection of the mean waterline and the floe's vertical axis of symmetry.

The floe has a length of $2L$, thickness H, and an equilibrium draft d. The mean

water depth is h. The geometric centre of the floe is denoted Z^c, which has the coordinates $(Z_x^c, Z_z^c) = (0, (H - 2d)/2)$. In Figure 4.1.1, s_1, s_2 and s_3 denote the respective wetted surface areas at the sides and bottom of the floe.

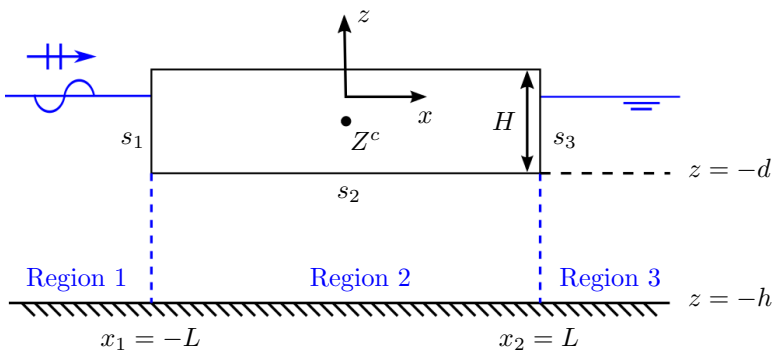

Figure 4.1.1: Two-dimensional Cartesian coordinate system and geometry of water-floe domain. The floe is represented as a rectangular cross-section.

In an inviscid, irrotational and incompressible flow, the velocity field of a body of water can be expressed as the gradient of a scalar velocity potential, $\Phi(x, z, t)$ (Linton and McIver, 2001). If we assume that waves are time-harmonic, then Φ can be expressed in terms of a time-independent complex potential $\phi(x, z)$ through

$$\Phi(x, z, t) = \mathrm{Re}\left\{\frac{g}{\mathrm{i}\omega}\phi(x, z)\mathrm{e}^{-\mathrm{i}\omega t}\right\}, \tag{4.1.1}$$

where Re denotes the real part, g is the gravitational constant, $\omega = 2\pi f$ is the angular wave frequency, and $\mathrm{i} = \sqrt{-1}$ is the imaginary unit.

In an irrotational and incompressible fluid, the potential ϕ throughout the fluid domain Ω satisfies Laplace's equation, $\nabla^2\phi = \partial_x^2\phi + \partial_z^2\phi = 0$. In this chapter, the notations $\partial_X = \partial/\partial X$ and $\partial_X^2 = \partial^2/\partial X^2$ are used to denote the first and second partial derivatives with respect to some variable X.

If wave steepnesses are sufficiently small, ϕ can be linearised (Mei et al., 2005, § 8.2) such that at the free-surface,

$$\partial_z\phi = \sigma\phi, \qquad \text{where} \qquad \sigma = \omega^2/g. \tag{4.1.2}$$

This linearised free-surface boundary condition is derived from Bernoulli's equation (see Linton and McIver, 2001, § 1.2, for example). On any static and impermeable surfaces (e.g. seabed), the no-normal-flow condition, $\partial_n\phi = 0$, exists. Here n refers to

the normal with respect to the static/impermeable boundary. Boundary conditions on the wetted surfaces of the floe depend on the motions of the floe. These conditions will be defined in the next section.

4.2 The eigenfunction matching method

In Figure 4.1.1, the fluid domain is divided into three distinct regions, which are separated by vertical interfacial boundaries at $x_1 = -L$ and $x_2 = L$. For each region, the expression for the potential ϕ can be found using the method of separation of variables (Mei et al., 2005, § 8.4). This involves applying the horizontal boundary conditions in each region, and the Sommerfeld far-field radiation condition in Regions 1 and 3. The Sommerfeld condition assumes that the potential at $|x| \rightarrow \infty$ consists of outgoing and incident waves only (Sommerfeld, 1949). The velocity potentials in each region are then solved explicitly by matching the potentials and horizontal velocities at the interfacial boundaries. This method is known as the eigenfunction matching method (Linton and McIver, 2001, § 2.5).

The wave-floe problem can also be analysed in terms of its diffraction and radiation parts separately. The potential ϕ can be solved by considering the problem as a sum of its diffraction and radiation parts. In the diffraction problem, a floe is considered to be artificially held in a fixed position. Incident waves are reflected and transmitted on either side of the floe. For radiation problems, a floe is considered to undergo forced oscillation in either surge, heave or pitch. Waves are radiated away from the floe as a result. Linearisation allows the potential ϕ to be expressed as a superposition of the diffraction and radiation potentials,

$$\phi = \phi^d + A_s\phi_s^r + A_h\phi_h^r + A_p\phi_p^r. \tag{4.2.1}$$

The superscripts d and r refer to the diffraction and radiation parts, and the subscripts s, h and p refer to surge, heave and pitch, respectively. Each radiation potential, ϕ^r, represents a unit solution for the corresponding radiation problem. Linearity implies that each radiation solution can be scaled by a factor of A. Recall that linearity of floe motions with respect to wave amplitude was observed in the

single-floe experiments (see § 2.3.1). The factors A_s, A_h and A_p are the unknown complex amplitudes of surge, heave and pitch. Their magnitudes give the surge, heave and pitch amplitudes, i.e. $a_s = |A_s|$, $a_h = |A_h|$ and $a_p = |A_p|$, and their arguments correspond to the phases of their respective motions. These complex amplitudes are determined by solving the equations of motion, which are derived in § 4.3.

Lee et al. (2007) and Wu et al. (1995) provide some examples of solution methods which are relevant to this problem. Lee et al. analysed the wave-induced motions of a rigid floating pontoon-pier system, while Wu et al. calculated the displacements of an elastic floating plate in waves. Both considered a two-dimensional problem and applied the eigenfunction matching method, described in Linton and McIver (2001, § 2.5), to derive solutions.

4.2.1 Diffraction problem

In the diffraction problem, we consider an incident wave interacting with a stationary floe. Since the floe is static, $\partial_n \phi = 0$ on surfaces s_1, s_2 and s_3. By applying the method of separation of variables and by taking into account the boundary conditions, the potentials in each region can be expressed as an infinite sum of eigenfunctions (Fourier series) as follows. In the free-surface regions (Regions 1 and 3),

$$\phi_1 = \sum_{n=0}^{\infty} \left(a_n^+ \mathrm{e}^{ik_n(x-x_1)} + a_n^- \mathrm{e}^{-ik_n(x-x_1)} \right) \psi_n, \tag{4.2.2}$$

and

$$\phi_3 = \sum_{n=0}^{\infty} \left(b_n^+ \mathrm{e}^{ik_n(x-x_2)} + b_n^- \mathrm{e}^{-ik_n(x-x_2)} \right) \psi_n, \tag{4.2.3}$$

respectively, for $n \in \mathbb{N}$. In the above expressions, the wavenumbers k_n correspond to the real and imaginary roots of the dispersion relation, $k \tanh kh = \sigma \equiv \omega^2/g$. The first term of the series ($n = 0$) corresponds to the propagating wave mode, therefore k_0 is the real root. All other terms ($n > 0$) represent evanescent wave modes, for which k_n is imaginary. The coefficients a_n and b_n denote the complex wave amplitudes in Regions 1 and 3, respectively. Superscripts $\pm$ indicate the direction of the wave with respect to x. The term ψ_n represents a vertical eigenfunction,

which is defined as

$$\psi_n(z) = \frac{\cosh k_n(z+h)}{\cosh k_n h}. \tag{4.2.4}$$

This term determines the value of the potential along the vertical transect of the water column.

In the floe-covered region (Region 2), the potential takes the form of

$$\phi_2 = \alpha_0^+ x + \alpha_0^- + \sum_{n=1}^{\infty} \left(\alpha_n^+ \mathrm{e}^{i\kappa_n(x-x_1)} + \alpha_n^- \mathrm{e}^{-i\kappa_n(x-x_2)}\right) \zeta_n. \tag{4.2.5}$$

Wavenumbers $\kappa_n = \mathrm{i}n\pi/(h-d)$ are purely imaginary. The coefficients $\alpha_n^\pm$ denote the complex wave amplitudes in the floe-covered region. In this region, the vertical eigenfunction ζ_n is defined as

$$\zeta_n(z) = \frac{\cosh \kappa_n(z+h)}{\cosh \kappa_n(h-d)}. \tag{4.2.6}$$

To derive numerical solutions of ϕ, the infinite series will be truncated into a maximum of $N+1$ modes, such that

$$\phi_1 \approx \sum_{n=0}^{N} \left(a_n^+ \mathrm{e}^{ik_n(x-x_1)} + a_n^- \mathrm{e}^{-ik_n(x-x_1)}\right) \psi_n, \tag{4.2.7}$$

for example. For brevity, bold lower-case symbols, e.g. $\boldsymbol{a}^+$, are implemented to represent column vectors containing the first $N+1$ terms of a_n^+, in this case. Again, superscripts $\pm$ indicate the direction of the wave with respect to x. In the diffraction problem, the coefficients of the incoming waves ($\boldsymbol{a}^+$ and $\boldsymbol{b}^-$) are prescribed. For a unidirectional wave, $\boldsymbol{a}^+$ is defined, while $\boldsymbol{b}^-$ is set to the zero vector $\mathbf{0}$. The remaining reflected and transmitted coefficients ($\boldsymbol{a}^-, \boldsymbol{b}^+, \boldsymbol{\alpha}^+$ and $\boldsymbol{\alpha}^-$) are found by implementing the dynamic and kinematic continuity conditions at the interfacial boundaries.

Dynamic continuity requires that water pressure is continuous across the vertical interfaces between each region. Water pressure, p, is calculated from the linearised Bernoulli's equation as $p = -\rho g z - \rho \partial_t \Phi$ (Dean and Dalrymple, 1991). Since ρ, g and z are constant on either sides of an interface, this implies that the potentials ϕ

will be consistent across the interface. In other words,

$$\phi_1 = \phi_2 \quad \text{at } x = x_1, \quad \text{and} \quad \phi_2 = \phi_3 \quad \text{at } x = x_2. \tag{4.2.8}$$

Kinematic continuity simply requires that the horizontal velocity is continuous across each interface, i.e.

$$\partial_x \phi_1 = \partial_x \phi_2 \quad \text{at } x = x_1, \quad \text{and} \quad \partial_x \phi_2 = \partial_x \phi_3 \quad \text{at } x = x_2. \tag{4.2.9}$$

Equations (4.2.7) to (4.2.5) are substituted into (4.2.8) and (4.2.9), and multiplied by an appropriate test function to obtain inner products, which are integrated over the intervals $z \in [-h, 0]$ and $z \in [-h, -d]$. The choice of test function is determined by the interval over which ϕ and $\partial_x \phi$ are integrated. The following test function is used when integrating over the limits $z \in [-h, 0]$:

$$\psi_m(z) = \frac{\cosh k_m(z+h)}{\cosh k_m h}. \tag{4.2.10}$$

When integrating over the limits $z \in [-h, -d]$, the following test function is applied:

$$\zeta_m(z) = \frac{\cosh \kappa_m(z+h)}{\cosh \kappa_m(h-d)}. \tag{4.2.11}$$

In the above, the subscript m refers to the $(m+1)$-th term of the test function, which is assigned to the $(m+1)$-th position in a row vector.

The truncated form of Equations (4.2.8) and (4.2.9) can therefore be expressed as

$$\sum_{n=0}^{N} (a_n^+ + a_n^-)\mathcal{A}_{nm} = (-\alpha_0^+ L + \alpha_0^-)\mathcal{B}_m + \sum_{n=1}^{N} \left(\alpha_n^+ + \alpha_n^- \mathrm{e}^{2\mathrm{i}\kappa_n L}\right) \mathcal{B}_{nm}, \tag{4.2.12}$$

$$\sum_{n=0}^{N} (a_n^+ - a_n^-)\mathrm{i}k_n \mathcal{D}_{nm} = \alpha_0^+ \mathcal{D}_m + \sum_{n=1}^{N} \left(\alpha_n^+ - \alpha_n^- \mathrm{e}^{2\mathrm{i}\kappa_n L}\right) \mathrm{i}\kappa_n \mathcal{C}_{nm}, \tag{4.2.13}$$

$$\sum_{n=0}^{N} (b_n^+ + b_n^-)\mathcal{A}_{nm} = (\alpha_0^+ L + \alpha_0^-)\mathcal{B}_m + \sum_{n=1}^{N} \left(\alpha_n^+ \mathrm{e}^{2\mathrm{i}\kappa_n L} + \alpha_n^-\right) \mathcal{B}_{nm}, \tag{4.2.14}$$

$$\sum_{n=0}^{N}(b_n^+ - b_n^-)\mathrm{i}k_n\mathcal{D}_{nm} = \alpha_0^+\mathcal{D}_m + \sum_{n=1}^{N}\left(\alpha_n^+\mathrm{e}^{2\mathrm{i}\kappa_n L} - \alpha_n^-\right)\mathrm{i}\kappa_n\mathcal{C}_{nm}, \tag{4.2.15}$$

where

$$\begin{aligned}
\mathcal{A}_{nm} &= \int_{-h}^{-d}\psi_n\zeta_m\,\mathrm{d}z, \quad \mathcal{B}_{nm} = \int_{-h}^{-d}\zeta_n\zeta_m\,\mathrm{d}z, \quad \mathcal{C}_{nm} = \int_{-h}^{-d}\zeta_n\psi_m\,\mathrm{d}z,\\
\mathcal{D}_{nm} &= \int_{-h}^{0}\psi_n\psi_m\,\mathrm{d}z, \quad \mathcal{B}_m = \int_{-h}^{-d}\zeta_m\,\mathrm{d}z, \qquad \mathcal{D}_m = \int_{-h}^{-d}\psi_m\,\mathrm{d}z.
\end{aligned} \tag{4.2.16}$$

Finally, the unknown vectors $\boldsymbol{a}^-$, $\boldsymbol{b}^+$, $\boldsymbol{\alpha}^+$ and $\boldsymbol{\alpha}^-$ are calculated by simultaneously solving Equations (4.2.12) to (4.2.15) using the solution matrix

$$\mathbf{S}\begin{bmatrix}\boldsymbol{a}^-\\ \boldsymbol{b}^+\\ \boldsymbol{\alpha}^+\\ \boldsymbol{\alpha}^-\end{bmatrix} = \mathbf{I}\begin{bmatrix}\boldsymbol{a}^+\\ \boldsymbol{b}^-\end{bmatrix}. \tag{4.2.17}$$

The matrices $\mathbf{S}$ and $\mathbf{I}$ represent the scattering and incident matrix, which contains terms in Equations (4.2.12) to (4.2.15) corresponding to the scattered coefficients ($\boldsymbol{a}^-$, $\boldsymbol{b}^+$, $\boldsymbol{\alpha}^+$ and $\boldsymbol{\alpha}^-$) and incident amplitudes ($\boldsymbol{a}^+$ and $\boldsymbol{b}^-$). In the diffraction problem, $\boldsymbol{a}^+$ and $\boldsymbol{b}^-$ must be specified. Far-field condition can be applied, such that the incident vectors contains propagating modes only.

The MATLAB code for the diffraction problem is available on `https://github.com/AdelaideUniversityMathSciences/SingleFloeModels/tree/master/PotentialFlow`.

4.2.2 Radiation problems

For radiation problems, a floe is forced to oscillate in either surge, heave or pitch to produce radiated waves. No incident waves are prescribed, since they have already been considered in the diffraction problem. Solutions for each radiation potential ϕ^r in Equation (4.2.1) are found by assigning a unit oscillation amplitude (i.e. $A_s = A_h = A_p = 1$). From this, the radiated wave amplitudes corresponding to each unit motion can be determined.

The wetted surface boundary conditions for each radiation problem are summarised

in Table 4.2.1. For pitch, the rotational axis is defined to coincide with the floe's geometric centre Z^c.

	On surface s_2	On surfaces s_1 and s_3
Surge	$\partial_z\phi = 0$	$\partial_x\phi = \sigma A_s$
Heave	$\partial_z\phi = \sigma A_h$	$\partial_x\phi = 0$
Pitch	$\partial_z\phi = -\sigma x A_p$	$\partial_x\phi = \sigma(z - Z_z^c)A_p$

Table 4.2.1: Wetted surface boundary conditions for radiation problems.

Using the method of separation of variables, the potentials in Regions 1 and 2 can be expressed as

$$\phi_1 = \sum_{n=0}^{\infty} a_n^- \mathrm{e}^{-\mathrm{i}k_n(x-x_1)}\psi_n, \tag{4.2.18}$$

$$\phi_3 = \sum_{n=0}^{\infty} b_n^+ \mathrm{e}^{\mathrm{i}k_n(x-x_2)}\psi_n. \tag{4.2.19}$$

In Region 2, it is convenient to express the potential as a sum of the homogenous and particular solution, $\phi_2 = \phi_2^h + \phi_2^p$, according to the method employed by Wu et al. (1995) and Lee (1995). This is done since potentials in Region 2 cannot be derived directly from the method of separation of variables when non-homogenous boundary conditions for heave and pitch on s_2 are applied. The expression for the homogenous solution ϕ_2^h can be derived by applying the boundary conditions of the diffraction problem. As a result, ϕ_2^h will be identical to Equation (4.2.5). Therefore

$$\phi_2 = \alpha_0^+ x + \alpha_0^- + \sum_{n=1}^{\infty} \left(\alpha_n^+ \mathrm{e}^{\mathrm{i}\kappa_n(x-x_1)} + \alpha_n^- \mathrm{e}^{-\mathrm{i}\kappa_n(x-x_2)}\right)\zeta_n + \phi_2^p. \tag{4.2.20}$$

For the particular solution, only Laplace's equation and the horizontal boundary conditions for Region 2 need to be satisfied. Therefore

$$\phi_2^p = 0 \qquad \text{for surge,} \tag{4.2.21}$$

$$\phi_2^p = \frac{\sigma A_h}{2(h-d)}\left[(z+h)^2 - x^2\right] \qquad \text{for heave,} \tag{4.2.22}$$

and

$$\phi_2^p = -\frac{\sigma x A_p}{2(h-d)}\left[(z+h)^2 - \frac{1}{3}x^2\right] \qquad \text{for pitch.} \tag{4.2.23}$$

The rest of the problem follows from the continuity conditions, as per the diffraction problem. The same test functions are used to derive the inner products. Continuity conditions therefore give

$$\sum_{n=0}^{N} a_n^- \mathcal{A}_{nm} = (-\alpha_0^+ L + \alpha_0^-)\mathcal{B}_m + \sum_{n=1}^{N} \left(\alpha_n^+ + \alpha_n^- \mathrm{e}^{2\mathrm{i}\kappa_n L}\right) \mathcal{B}_{nm} + [\mathcal{F}_1]_{x=x_1}, \quad (4.2.24)$$

$$\sum_{n=0}^{N} -a_n^- \mathrm{i}k_n \mathcal{D}_{nm} = \alpha_0^+ \mathcal{D}_m + \sum_{n=1}^{N} \left(\alpha_n^+ - \alpha_n^- \mathrm{e}^{2\mathrm{i}\kappa_n L}\right) \mathrm{i}\kappa_n \mathcal{C}_{nm} + [\mathcal{F}_2]_{x=x_1} + \mathcal{F}_3, \quad (4.2.25)$$

$$\sum_{n=0}^{N} b_n^+ \mathcal{A}_{nm} = (\alpha_0^+ L + \alpha_0^-)\mathcal{B}_m + \sum_{n=1}^{N} \left(\alpha_n^+ \mathrm{e}^{2\mathrm{i}\kappa_n L} + \alpha_n^-\right) \mathcal{B}_{nm} - [\mathcal{F}_1]_{x=x_2}, \quad (4.2.26)$$

$$\sum_{n=0}^{N} b_n^+ \mathrm{i}k_n \mathcal{D}_{nm} = \alpha_0^+ \mathcal{D}_m + \sum_{n=1}^{N} \left(\alpha_n^+ \mathrm{e}^{2\mathrm{i}\kappa_n L} - \alpha_n^-\right) \mathrm{i}\kappa_n \mathcal{C}_{nm} + [\mathcal{F}_2]_{x=x_2} + \mathcal{F}_3. \quad (4.2.27)$$

In Equations (4.2.24) to (4.2.24), $\mathcal{A}_{nm}$, $\mathcal{B}_{nm}$, $\mathcal{C}_{nm}$, $\mathcal{D}_{nm}$, $\mathcal{B}_m$ and $\mathcal{D}_m$ are consistent with those of (4.2.16) in the diffraction problem. The terms $\mathcal{F}_1$, $\mathcal{F}_2$ and $\mathcal{F}_3$ are row vectors representing the hydrodynamic forcing from oscillatory floe motions. These are evaluated as

$$\mathcal{F}_1 = \int_{-h}^{-d} \phi_2^p \, \zeta_m \, \mathrm{d}z, \quad \mathcal{F}_2 = \int_{-h}^{-d} \partial_x \phi_2^p \, \eta_m \, \mathrm{d}z, \quad \mathcal{F}_3 = \int_{-d}^{0} \partial_x \phi \, \eta_m \, \mathrm{d}z. \quad (4.2.28)$$

Radiation problems are solved using the solution matrix

$$\mathbf{S} \begin{bmatrix} \boldsymbol{a}^- \\ \boldsymbol{b}^+ \\ \boldsymbol{\alpha}^+ \\ \boldsymbol{\alpha}^- \end{bmatrix} = \mathbf{F}. \quad (4.2.29)$$

In Equation (4.2.29), the scattering matrix $\mathbf{S}$ is equivalent to that of the diffraction problem. The only difference is on the right-hand side of (4.2.29). Here, instead of an incident matrix, a forcing matrix $\mathbf{F}$ is used to represent the forcing terms $\mathcal{F}_1$, $\mathcal{F}_2$ and $\mathcal{F}_3$ associated with Equations (4.2.24) to (4.2.27).

Solutions to the radiation problems can be obtained via `https://github.com/AdelaideUniversityMathSciences/SingleFloeModels/tree/master/PotentialFlow`.

4.2.3 Analytical and numerical checks

In § 1.4 of Linton and McIver (2001), several reciprocity relations are provided as theoretical checks for solutions to the diffraction and radiation problems. The first check for the diffraction problem is derived from the requirements of conservation of energy. This translates to the identity

$$|\mathcal{R}|^2+|\mathcal{T}|^2= 1, \tag{4.2.30}$$

in which $\mathcal{R}$ and $\mathcal{T}$ are the reflection and transmission coefficients corresponding to a_0^- and b_0^+. All solutions to the diffraction problem satisfied this identity.

Green's theorem in a plane was also be applied to check the solutions of the diffraction and radiation problems individually. Linton and McIver (2001, § 1.4) and Mei et al. (2005, § 8.6) provide detailed descriptions of this check. Green's theorem allows us to derive the equation

$$\iint_\Omega \phi\ \nabla^2\bar{\phi} - \bar{\phi}\ \nabla^2\phi\ \mathrm{d}\Omega = \int_{\delta\Omega} \phi\ \partial_n\bar{\phi} - \bar{\phi}\ \partial_n\phi\ \mathrm{d}S = 0, \tag{4.2.31}$$

which is integrated around the perimeter of the fluid domain $\delta\Omega$. The term $\bar{\phi}$ denotes the complex conjugate of ϕ. Figure 4.2.1 shows the boundary conditions on $\delta\Omega$ for the surge problem. Far-field conditions are assumed at $x_\pm \to \pm\infty$, i.e. $\phi(x_\pm, z)$ consists of propagating modes only. Solutions to the diffraction and radiation problems are also confirmed to satisfy Equation (4.2.31).

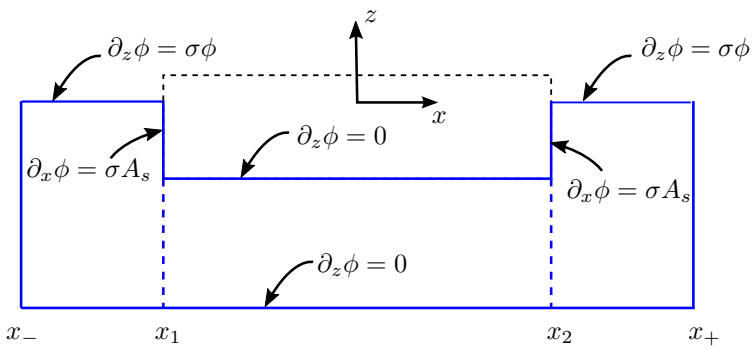

Figure 4.2.1: Boundary conditions for surge problem. The perimeter of the fluid domain $\delta\Omega$ is defined by the blue outlined region.

Solutions for the radiation problems were also verified against the results of Black

et al. (1971), who also formulated the surge, heave and pitch problems in two dimensions using linear potential-flow theory, and applied the eigenfunction matching method to solve the problem. Black et al. presented the normalised radiated wave amplitudes of the individual problems as functions of the wavelength parameter kd. Radiated wave amplitudes were normalised as

$$\mathscr{A}_s = \frac{a_0^-}{A_s}, \quad \mathscr{A}_h = \frac{a_0^-}{A_h} \quad \text{and} \quad \mathscr{A}_p = \frac{a_0^-}{A_p L}. \tag{4.2.32}$$

The magnitudes of these values, for two length to draft ratios ($L/d = 1$ and 3), are shown in Figure 4.2.2. These values are extracted directly from Figures 4 (a), (b) and (c) in Black et al. (1971). Solutions generated by our model are overlaid for comparison. In our numerical simulations, potentials are truncated at a value of $N = 100$. Results are virtually indistinguishable, thus confirming the validity of our solution.

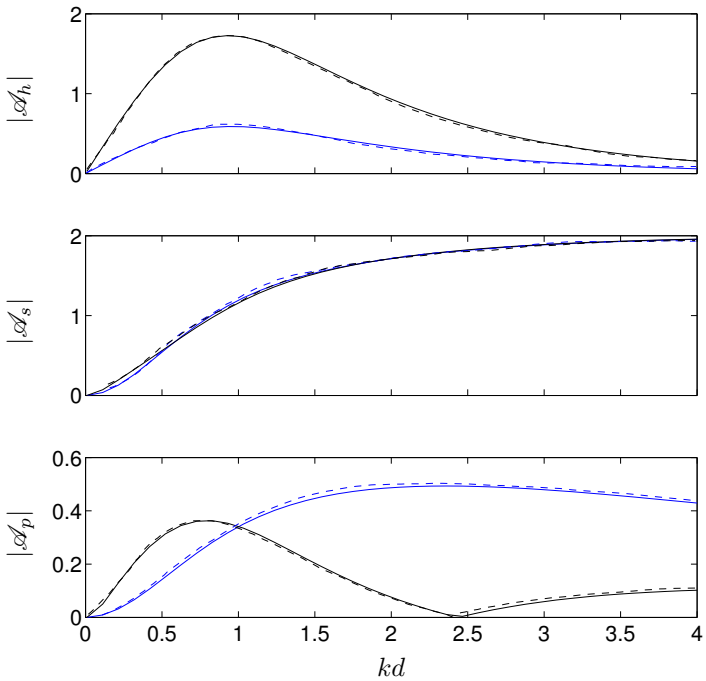

Figure 4.2.2: Comparison between potential-flow model (solid) and results from Black et al. (1971) (dashed). Magnitude of normalised radiated wave amplitudes for surge, heave and pitch problems (top to bottom panels, respectively), as a function of kd. Blue curves indicate $L/d = 3$, black curves indicate $L/d = 1$.

The final check confirms both diffraction and radiation solutions by associating their far-field solutions using the Bessho-Newman relations. Bessho (1965) and Newman

(1975) derived the following identity

$$\mathcal{D}^{+} + \bar{\mathcal{D}}^{+}\mathcal{R} + \bar{\mathcal{D}}^{-}\mathcal{T} = 0, \tag{4.2.33}$$

where $\mathcal{R} = a_0^-$ and $\mathcal{T} = b_0^+$ are the reflection and transmission coefficients from the diffraction problem, and $\mathcal{D}^+ = b_0^+$ and $\mathcal{D}^- = a_0^-$ are the radiated coefficients scaled with respect to the surge, heave and pitch amplitudes (A_s, A_h and A_p). The terms $\bar{\mathcal{D}}^{\pm}$ are the complex conjugates of $\mathcal{D}^{\pm}$. Note that this check can only be used once the surge, heave and pitch amplitudes have been calculated (see § 4.3).

4.2.4 Accuracy and convergence

The accuracy of the solutions to the diffraction and radiation problems are determined by the size of the eigenfunction expansion. In other words, accuracy is defined by the value of N. Higher degrees of accuracy are obtained when N increases. However, computation time also increases with the number of modes extracted. Therefore, it is necessary determine the minimum value of N required to give sufficiently accurate solutions.

One way of quantifying accuracy is to compare the matching criteria at the interfacial boundaries at x_1 and x_2. By doing so, this will satisfy the continuity conditions. Figure 4.2.3 shows the absolute values of the potential, $|\phi|$, and horizontal velocity $|\partial_x \phi|$ from the diffraction problem, along the boundary x_1. Potentials and velocities are calculated, using the expressions of ϕ in Regions 1 and 2. Solutions are compared when $N = 3$ and $N = 20$. Simulation parameters for this example are $f = 0.5\,\mathrm{Hz}$ and $a = 1\,\mathrm{m}$. All other parameters are as with the example problem in § 3.2.

Figure 4.2.3 demonstrates how the error decreases with increasing N. When $N = 20$, the potentials are virtually the same in Regions 1 and 2. However, for the same value of N, differences between velocities in each region can still be identified.

Accuracy can be calculated by quantifying the error between potentials and velocities in each region along the interfacial boundary. The errors between potentials, $E_{|\phi|}$, and velocities $E_{|\partial_x \phi|}$, are calculated numerically by summing the differences at each z-interval and multiplying the total by the width of the z-interval. For sufficiently

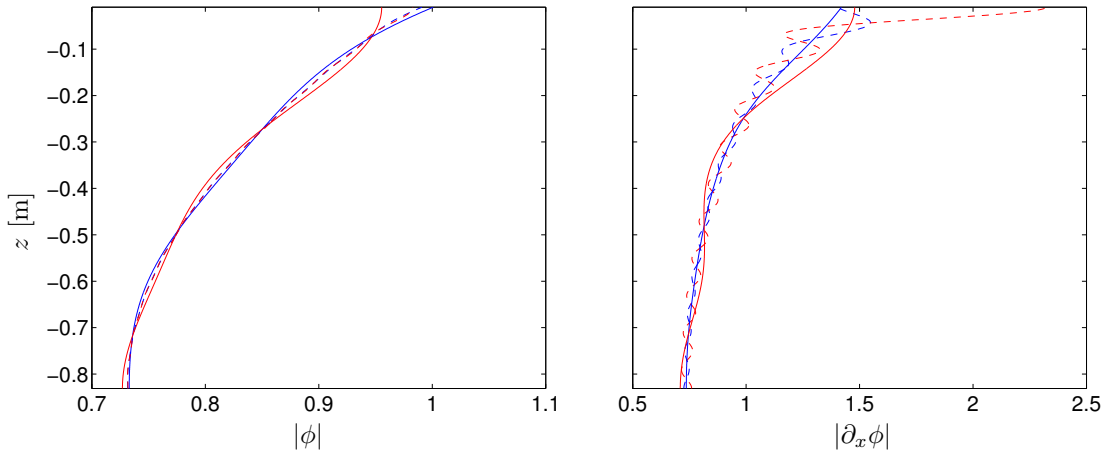

Figure 4.2.3: Absolute values of potentials (left panel) and horizontal velocities (right panel) along the vertical fluid interface at $x = -L$, for the diffraction problem. Potentials and velocities in Region 1 (blue) and Region 2 (red) are shown when $N = 3$ (solid) and $N = 20$ (dashed).

small widths, the error is approximately equal to the area between the red and blue curves in Figure 4.2.3. In the following examples, $z \in [-h, -d]$ is divided into 2000 equal intervals.

Figure 4.2.4 shows the error between the absolute values of potentials $|\phi|$ and velocities $|\partial_x \phi|$, for the diffraction problem, at the boundary x_1. Parameters for the example problem are used in this simulation, and a unit incident wave amplitude is prescribed. Errors are proportional to the incident amplitude, a, since the potential is linear with respect to a. Errors are calculated for modes ranging from $N = 20$ to 400, and for wave frequencies from $f = 0.5$ to 2 Hz. Frequencies are differentiated by colour gradients ranging from green to blue. Results are plotted on a semi-log scale for clarity.

Errors for both potentials and velocities are shown to increase with increasing wave frequency. When 100 modes are used, potentials have errors of less than $10^{-3}\,\mathrm{m}^2\,\mathrm{s}^{-1}$. Therefore, when incident wave amplitudes are $\mathrm{O}(10^{-2})\,\mathrm{m}$, which is in the range of those used in the single-floe experiments, we expect that errors between potentials will be $\mathrm{O}(10^{-5})\,\mathrm{m}^2\,\mathrm{s}^{-1}$. Figure 4.2.4 also confirms that errors are larger for velocities. When $N = 100$, errors in velocity are between $\mathrm{O}(10^{0}\text{-}10^{-2})\,\mathrm{m\,s}^{-1}$. Note that the computational time for 100 modes is approximately 0.3 seconds on a 2.7 GHz Intel Core i5 processor with a 8 GB 1600 MHz DDR3 RAM. In contrast, the computational time when $N = 400$ is approximately 8 seconds.

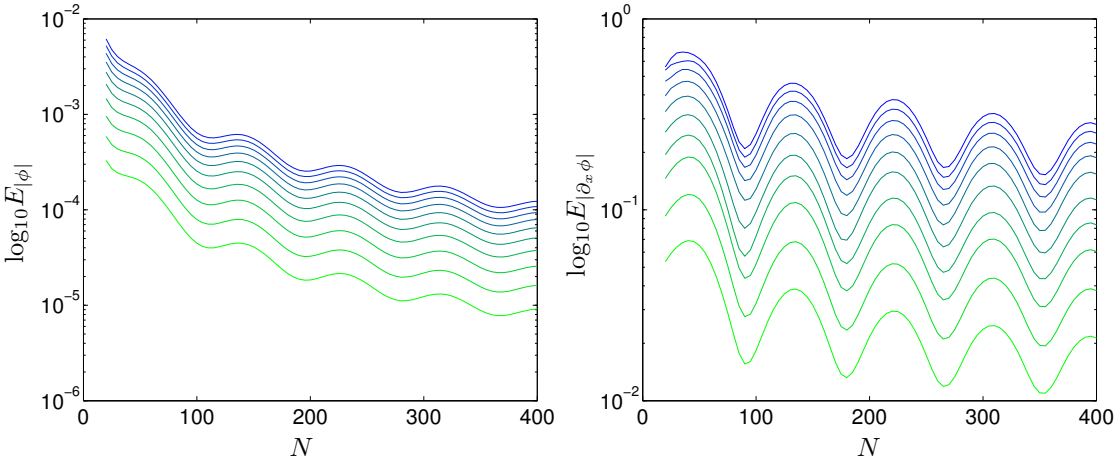

Figure 4.2.4: Error between potentials (left panel) and velocities (right), as a function of number of modes N, for incident wave frequencies ranging from $f = 0.5$ to 2 Hz (green to blue, respectively).

Another way of quantifying accuracy is to test for the convergence of diffracted and radiated coefficients. Numerical tests are performed for the diffraction problem, as an example. The same test parameters used in the previous examples are applied here. Figure 4.2.5 shows the convergence of the reflected and transmitted coefficients (C_R and C_T) for modes ranging from $N = 1$ to 200, and for wave frequencies from $f = 0.5$ to 2 Hz. The same colour gradient is used to indicate different frequencies. The quantity C_R is calculated by taking the difference between the real part of a_0^- at each successive value of N. Similarly, C_T is calculated using the difference of $\mathrm{Re}\{b_0^+\}$. Figure 4.2.5 shows that 100 modes is sufficient for reflection and transmission coefficients to converge to $\mathrm{O}(10^{-4})$ m.

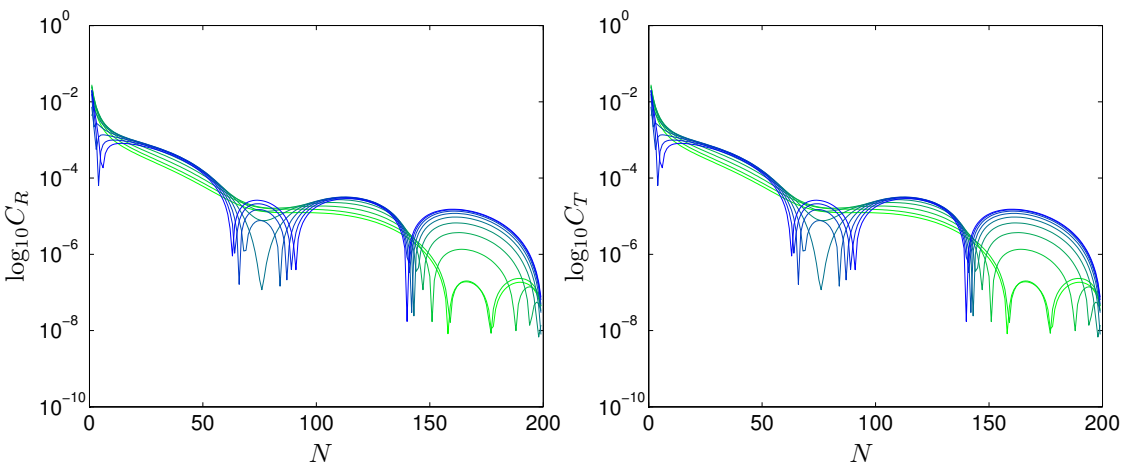

Figure 4.2.5: Convergence of reflected and transmitted coefficients (left and right panels, respectively), for wave frequencies between $f = 0.5$ to 2 Hz (green to blue).

Lee (1995) also used 100 modes to derive accurate analytical solutions to a heave-

radiation problem. Montiel (2012) studied the convergence of the eigenfunction matching method by analysing the reflection coefficient and free surface elevation, and deduced that 20-30 modes were sufficient for obtaining solutions with two significant digit accuracy.

4.3 Equations of motion

Once the diffraction and unit radiation potentials have been determined, the next step is to calculate the surge, heave and pitch amplitudes. The amplitudes A_s, A_h and A_p are calculated using the equations of motion, which are derived by applying the principles of conservation of linear momentum in the x and z directions, and conservation of angular momentum for rotations in the xz plane (John, 1949; Mei et al., 2005, § 8.2). The equations of motion are expressed as

$$-\omega^2 \mathbf{M} \begin{bmatrix} A_s \\ A_h \\ A_p \end{bmatrix} + \mathbf{C} \begin{bmatrix} A_s \\ A_h \\ A_p \end{bmatrix} = \rho g \int_{S_B} \phi \, \mathbf{n} \;\, \mathrm{d}S. \tag{4.3.1}$$

On the left-hand side, $\mathbf{M}$ and $\mathbf{C}$ refer to the mass and hydrostatic restoring force matrices, where

$$\mathbf{M} = \begin{bmatrix} m & 0 & 0 \\ 0 & m & 0 \\ 0 & 0 & I_{xx} + I_{zz} \end{bmatrix} \quad \text{and} \quad \mathbf{C} = \begin{bmatrix} 0 & 0 & 0 \\ 0 & 2\rho g L & 0 \\ 0 & 0 & \rho g \left(I_{xx}^A + I_z^V \right) \end{bmatrix}. \tag{4.3.2}$$

Note that the floe mass, m, is specified in units $\mathrm{kg\,m^{-1}}$, and is calculated as $m = 2Ld\rho$. Also, the units for fluid density ρ is $\mathrm{kg\,m^{-3}}$. The terms I_{xx} and I_{zz} are the moments of inertia with reference to the x and z axes, which are evaluated as,

$$\begin{aligned} I_{xx} &= \iint_{V_B} (x - X^c)^2 \;\, \mathrm{d}m = \frac{2}{3} L^3 d\rho, \\ I_{zz} &= \iint_{V_B} (z - Z^c)^2 \;\, \mathrm{d}m = \frac{1}{6} H^2 dL\rho, \end{aligned} \tag{4.3.3}$$

The terms I^A_{xx} and I^V_z are the moments of buoyancy due to rotations in the xz plane, which are evaluated as,

$$\begin{aligned} I^A_{xx} &= \int_{S_A} x^2 \ \ \mathrm{d}x = \frac{2}{3}L^3, \\ I^V_z &= \iint_{V_S} (z - Z^c)^2 \ \ \mathrm{d}x \ \mathrm{d}z = Ld(d - H). \end{aligned} \tag{4.3.4}$$

In the above equations, V_B is the cross-section of the entire body, V_S is the submerged cross-section and S_A is the length of the waterline.

The right-hand side of (4.3.1) contains the hydrodynamic forcing terms, which can be found by integrating the potential around the wetted surface S_B with respect to the normal $\mathbf{n} = [n_1 \ n_2 \ n_3]^{\mathrm{T}}$. The first two terms of $\mathbf{n}$ are the unit normal vectors in the x and z axes. The last term $n_3 = n_1(z - Z^c_z) - n_2 x$. The right-hand side of (4.3.1) can be expanded into its diffraction and radiation parts by applying Equation (4.2.1). This gives

$$\int_{S_B} \phi^d \begin{bmatrix} n_1 \\ n_2 \\ n_3 \end{bmatrix} \mathrm{d}S + \int_{S_B} \begin{bmatrix} n_1 \\ n_2 \\ n_3 \end{bmatrix} \begin{bmatrix} \phi^r_s \\ \phi^r_h \\ \phi^r_p \end{bmatrix}^{\mathrm{T}} \begin{bmatrix} A_s \\ A_h \\ A_p \end{bmatrix} \mathrm{d}S. \tag{4.3.5}$$

Surge, heave and pitch amplitudes are obtained by substituting (4.3.5) into (4.3.1), and solving the system of linear equations for $[A_s \ A_h \ A_p]^{\mathrm{T}}$.

Solutions to the equations of motion can be obtained via `https://github.com/AdelaideUniversityMathSciences/SingleFloeModels/tree/master/PotentialFlow`.

4.4 Analytical proofs in the long-wavelength limit

In the single-floe experiments (§ 2.3, Figure 2.3.2), we observed that incident wave-field remains unmodified by a floe in the long-wavelength regime. Under this condition, the potential ϕ in Equation (4.3.1) can be approximated by the incident mode, $\phi_I = a^+_0 \mathrm{e}^{\mathrm{i}k_0 x}\psi_0(z)$. For convenience, all subscripts and superscripts are dropped.

The horizontal equation of motion becomes

$$\begin{aligned} -\omega^2 m A_s &\approx \rho g \int_{-d}^{0} \left[a \mathrm{e}^{\mathrm{i}kx} \frac{\cosh k(z+h)}{\cosh kh} \right]_{x_2}^{x_1} \mathrm{d}z \\ &= -\mathrm{i}agk\ 2Ld\rho + \mathrm{O}\left((kL)^2\right). \end{aligned} \tag{4.4.1}$$

Since the wavenumber $k \to 0$ in long waves, only leading orders of kL are considered. The complex surge amplitude is therefore approximately

$$A_s = \frac{\mathrm{i}kga}{\omega^2} = \mathrm{i}a \coth kh. \tag{4.4.2}$$

The final expression is derived by applying Archimedes' formula $m = 2Ld\rho$, and the dispersion relation $k \tanh kh = \omega^2/g$. The absolute surge amplitude is therefore

$$a_s = |A_s| = a \coth kh. \tag{4.4.3}$$

This proof shows that the surge RAO will tend to 1 as $k \to 0$. Recall, a similar expression was obtained from the analytical long-wavelength approximation of the slope-sliding model (see § 3.5). The only difference is the inclusion of an added mass coefficient in the slope-sliding model. Analytical solutions for the linear potential-flow model are found to be within 10% of the full solution when λ/D is approximately greater than 4.5. The error decreases to 5% when $\lambda/D \approx 6.7$.

4.5 Model-data comparisons

The left panels of Figures 4.5.1 to 4.5.3 compare the surge, heave and pitch RAOs predicted by the linear potential-flow model with data from single-floe experiments (as presented in Figure 2.3.3). RAOs are expressed as a function of nondimensional wavelength. Data from both Floes B and NB are shown. Error bars are included for each data point. The right panels of the same figures highlight the differences, δ-RAO, between the single-floe data and the potential-flow model, as functions of nondimensional wavelength, i.e. $\delta\text{-RAO} = \text{RAO}_{\text{experiment}} - \text{RAO}_{\text{model}}$. In these panels, the mean RAOs, with respect to incident wavelength, of Floes B and NB are shown.

Error bars mark the overall maximum and minimum RAOs of each floe, at each incident wavelength. Figure 4.5.1 also includes the surge RAOs predicted by the slope-sliding model for comparison. Solutions are generated using zero drag $c_d = 0$ and an added mass $c_m = 0.1$.

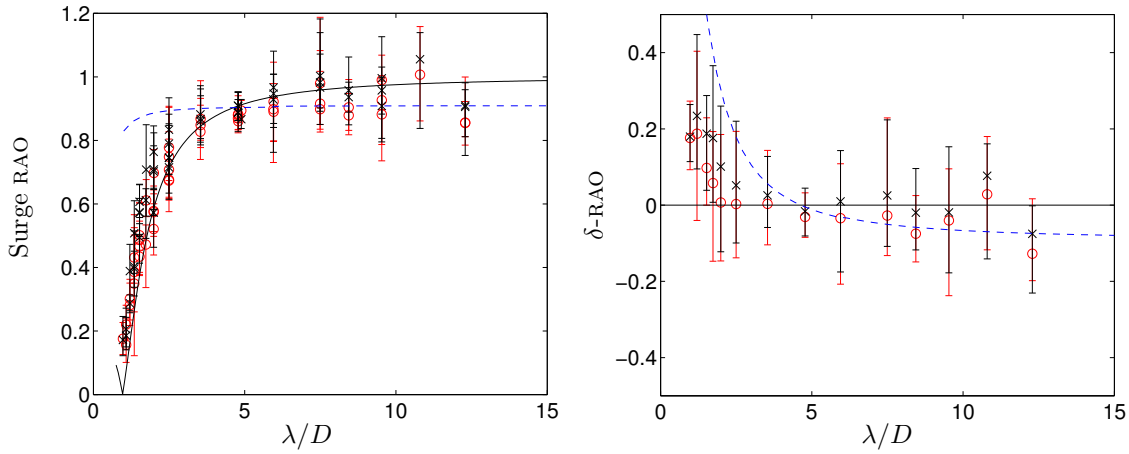

Figure 4.5.1: Left panel: Comparison of surge RAOs predicted by the potential-flow model (−) and slope-sliding (- -) model when $c_d = 0$ and $c_m = 0.1$, and experimental data from Matrix 1 (Floe B, × and Floe NB, ○). Right panel: Differences between potential-flow model and slope-sliding model (- -) and experimental data when grouped according to incident wavelength and floe. Symbols represent group means. Error-bar limits represent overall group maximum and minimum differences.

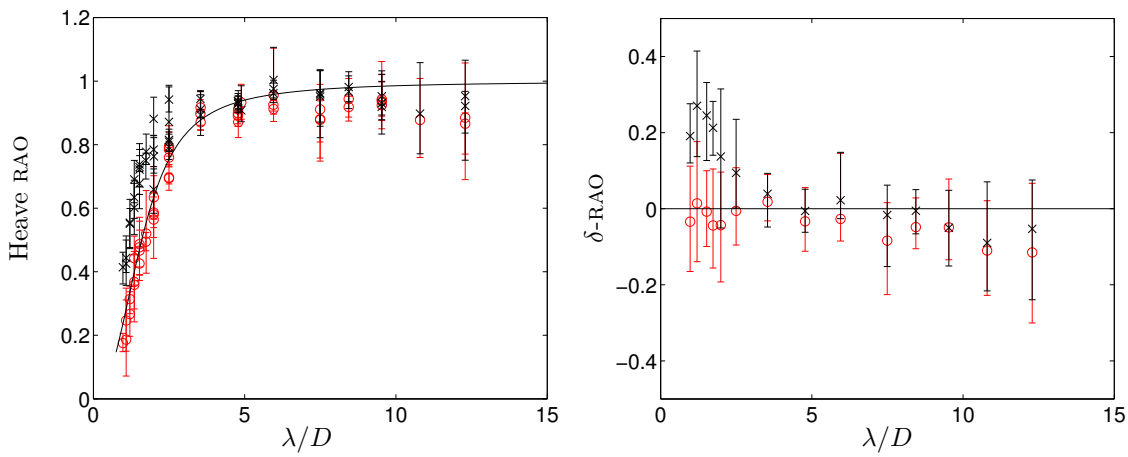

Figure 4.5.2: As per Figure 4.5.1 but for heave.

The potential-flow model is generally accurate over the range of incident wavelengths considered. This is especially evident for predictions of surge, which lie within the overall limits of error in wavelengths $\lambda/D > 1.74$ for Floe B, and $\lambda/D > 0.98$ for Floe NB. For heave, the predicted RAOs lie outside the range of error of Floe B only when $\lambda/D < 1.74$. For pitch, the same occurs only when $\lambda/D = 1.74$ and 0.98. The

potential-flow model tends to underpredict the RAOs of Floe B when $\lambda/D < 1.74$. When compared with Floe NB, the model generally overpredicts the mean RAOs for pitch and underpredicts the mean RAOs for surge when $\lambda/D < 1.74$. This coincides with the increasing divergence of RAOs of Floes B and NB when λ/D decreases in the short-wavelength regime. The divergence is greatest in heave and pitch.

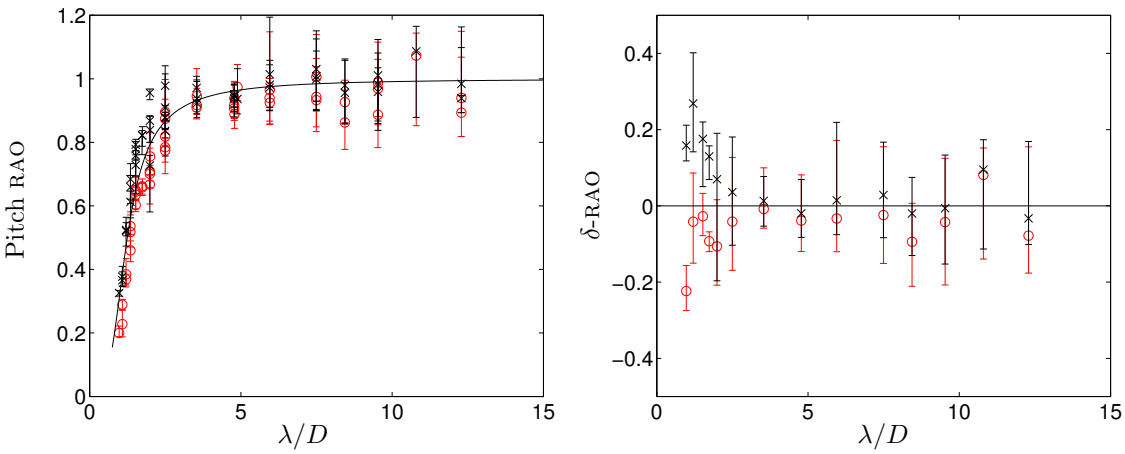

Figure 4.5.3: As per Figure 4.5.1 but for pitch.

Differences between the mean RAOs of each floe and the potential-flow model are relatively small. For Floe B, the largest average difference over the range of incident wavelengths considered is 0.07 units for heave, and the smallest is 0.04 units for pitch. For Floe NB, the largest average difference is -0.04 units for heave, and the smallest is 0.02 units for surge. Differences, however, are slightly larger in the short-wavelength regime. For example, when comparing the heave RAOs of Floe B with the model, the average difference is 0.19 units when $\lambda/D < 3$, and -0.01 units when $\lambda/D > 3$. The potential-flow model consistently overpredicts the RAOs of Floe B in the long-wavelength regime, and underpredicts its RAOs in the short-wavelength regime. The model generally overpredicts the RAOs of Floe NB in both regimes. The only exception is underprediction of the surge in the short-wavelength regime.

In the long-wavelength regime, the slope-sliding model is more accurate than the potential-flow model. Recall, the higher accuracy was achieved by tuning the added mass to $c_m = 0.1$. In the short-wavelength regime, experimentally measured surge RAOs are more closely aligned with the potential-flow model.

Figure 4.5.4 compares the surge RAOs of the potential-flow model with data from the second test matrix of the single-floe experiments. RAOs are presented in terms

of their relative deviation, Δ_{RAO}, and expressed as a function of wave steepness, as was done in Figure 2.3.4. Here, the relative deviation is calculated as

$$\Delta_{\text{RAO}} = \frac{\text{RAO}_{\text{experiment}} - \text{RAO}_{\text{model}}}{\text{RAO}_{\text{model}}} \tag{4.5.1}$$

For the longer wavelength, $\lambda/D = 2.50$, the model mostly underpredicts the surge RAOs for both floes. The mean deviation is 11.5% for Floe B and 2.1% for Floe NB. For the shorter wavelength, $\lambda/D = 1.73$, the model underpredicts the surge RAOs of Floe B over all wave steepnesses considered. The mean deviation for Floe B is 9.7%. The model however underpredicts the surge RAO of Floe NB for the lowest steepness only. For larger steepnesses, the decrease in surge RAOs results in the model overpredicting surge. The largest deviation for Floe NB is −15.8%, and occurs at $ka = 0.16$.

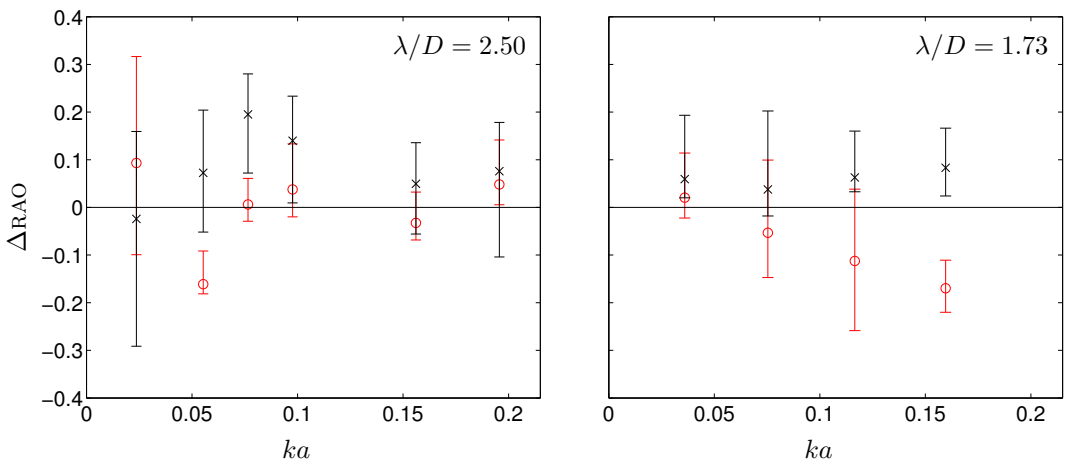

Figure 4.5.4: As per Figure 2.3.4, but for deviation of experimental data from the potential-flow model.

4.6 Summary

A two-dimensional model based on linear potential-flow theory was formulated to calculate the surge, heave and pitch motions of a solitary floe in waves. Linearisation allows the problem to be separated into diffraction and radiation parts. The model first solved for the potentials of the diffraction and radiation problems using the eigenfunction matching method, in which potentials and velocities are matched at

the vertical boundaries between the open-water and floe-covered regions. Surge, heave and pitch amplitudes were then calculated using the equations of motion in the horizontal, vertical and rotational axes.

A thorough convergence analysis was performed to deduce the number of eigenmodes required to generate accurate solutions. Accuracy was quantified according to the error between potentials and velocities at interfacial fluid boundaries, and the convergence of diffracted and radiated wave amplitudes. Approximately 100 modes gave sufficiently accurate solutions, without compromising computational time. To our knowledge, detailed studies of the convergence of the eigenfunction matching method according to these criteria have not been conducted thus far.

An analytical proof was presented to show that the surge amplitudes predicted by the potential-flow model in long-wavelength limit is identical to that of the slope-sliding model, except for the added mass term, which is absent from the potential-flow model. If the added mass in the slope-sliding model is set to zero, both models predict a unit surge response (with respect to water particle displacements) in the long-wavelength limit.

The potential-flow model was then compared against the slope-sliding model and data from the single-floe experiments. RAOs predicted by the potential-flow model were shown to be more accurate than the slope-sliding model in the short-wavelength regime (which was defined in Chapter 2 as wavelengths less than 3 times the floe length). The potential-flow model, however, slightly overpredicted the experimental RAOs in the long-wavelength regime.

The potential-flow model could not account for the decrease in RAOs with increased wave steepnesses in short wavelengths. Models incorporating overwash will likely improve the accuracy of the model in the short-wavelength regime.

Chapter 5

Two-floe non-rafting experiments

The second round of wave basin experiments was again implemented in the Model Test Basin (MTB) facility at the Australian Maritime College immediately following the completion of the single-floe experiments. In this round of experiments, the collisions of two identical adjacent floes are investigated in regular waves. Edge barriers were used to prevent floes from rafting, therefore investigations here are restricted to non-rafting collisions only. This chapter describes the methods and results obtained from our experiments.

5.1 Objectives

The main objectives the two-floe non-rafting experiments were to:

1. simulate non-rafting collisions between two adjacent floes;
2. determine the wave conditions necessary for collisions to occur;
3. quantify collision behaviours over a range of wavelengths and wave amplitudes.

To simulate collisions, floes were positioned at close proximity, in line with the direction of incident waves. Collisions are analysed by measuring and interpreting the surge and drift motions of both floes.

5.2 Experimental method

5.2.1 Floe properties

Tests were performed using two model floes. Figure 5.2.1 shows a photo of the two floes in their initial setup. Both floes are identical to Floe B, which was used in the single-floe experiments (see § 2.2.2 for details). Edge barriers on both floes inhibited rafting, and consequently, prevented overwash.

The mooring system was modified from the single-floe experiments. Nylon wires were used in place of elastic tethers. The function of the mooring lines were to limit drift motions, induce multiple collisions, and reset the floes to their initial configurations after each test. Both floes were moored to the sides of the basin. In general, the mooring system in these experiments were more restrictive than the elastic tethers in the single-floe experiments. Figures 5.2.1 and 5.2.2 show how the mooring system was set up.

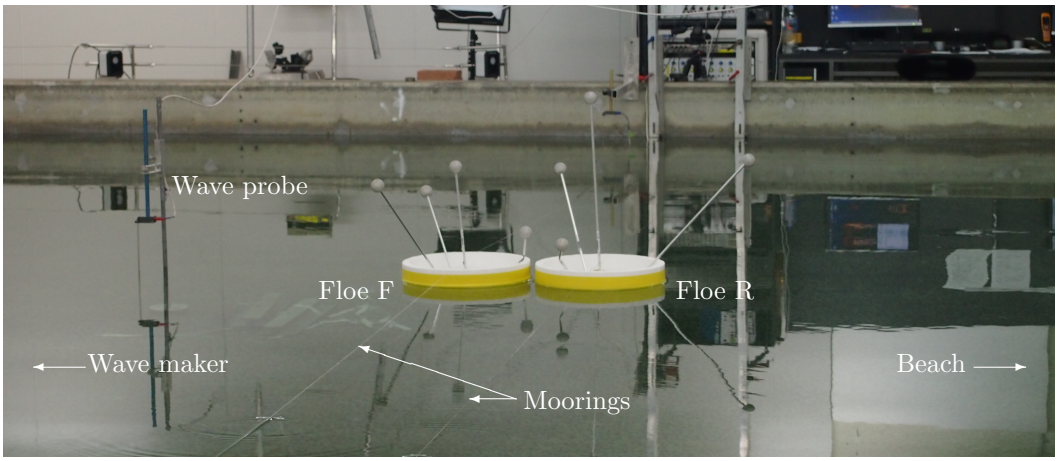

Figure 5.2.1: Photo of Floes F and R in their initial positions.

5.2.2 Setup and instrumentation

Figure 5.2.2 shows a schematic plan view of the MTB during the two-floe experiments. We adopt the same Cartesian coordinate system (x, y, z) used in the single-floe experiments (see § 2.2.3) to define locations in the basin. The only difference is the origins of the x and y axes are now set to coincide with the axisymmetric centre of the front floe (closest to the wave maker). The front and rear floes are denoted as

Floe F and Floe R, respectively. The location of the geometric centre for Floe F is $X_F(t)$, and $X_R(t)$ for Floe R. Floe F was positioned approximately 16 m down the MTB, and 6 m from either side of the basin.

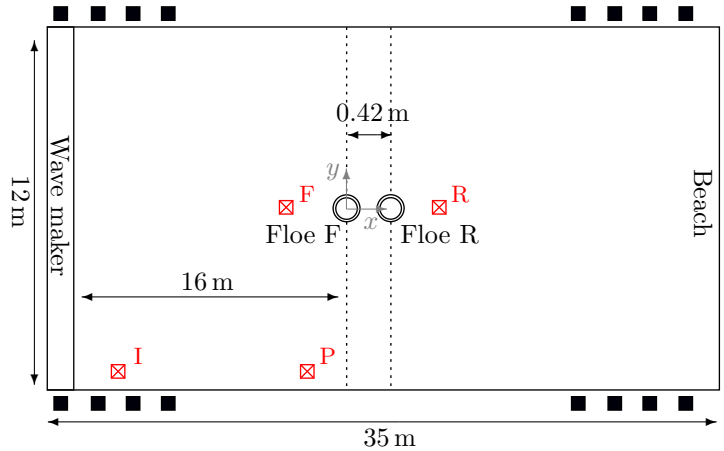

Figure 5.2.2: Schematic plan view of MTB for two-floe experiments. Concentric circles represent floes and dashed lines represent mooring lines. Symbols indicate wave probes (⊠) and motion tracking cameras (■).

The function $s(t)$ is used to denote the instantaneous separation between floes. Separation is defined as the distance between Floes F and R at their closest points. Both floes were separated by an initial distance of $s_0 \equiv s(0) = 20\,\text{mm}$. The initial positions are therefore $(X_F(0), Y_F(0), Z_F(0)) = (0, 0, 0)$ for Floe F, and $(X_R(0), Y_R(0), Z_R(0)) = (0.42, 0, 0)\,\text{m}$ for Floe R.

The Qualisys system was again utilised to record the motions of each floe in over a 60 s test interval. § 2.2.4 describes how the system operates. Because of the closer proximities of the two floes, longer aluminium rods were used to mount the infrared (IR) markers. This was done to maximise the separation between the markers and thus prevent their signals from overlapping on the IR image. However in spite of this, it was still quite common for the markers of one floe to interfere with the other. When this occurred, Qualisys gave erroneous measurements of the six-degree-of-freedom motions. Attempts were made to repeat any tests affected by this issue.

Incident wave amplitudes and frequencies were again measured at specific locations throughout the wave basin, using a series of four wave probes. Figure 5.2.2 shows their locations. As with the single-floe experiments, two probes were installed along the sides of the basin – one measured the wavefield close to the wavemaker, the other

measured the wavefield approximately 15 m down the wave basin. These probes are denoted as Probes I and P, respectively. Two other probes were positioned approximately 2 m in front of Floe F, and 2 m behind Floe R. These probes, which are respectively labelled as Probes F and R, measure the wavefield in the vicinity of the floes without obstructing the motions of the floes.

Measured wave frequencies were consistent with target frequencies. The maximum difference was less than 2% of the target value. Wave amplitudes measured at all four wave probes were, however, observed to be slightly smaller than target values. Amplitudes measured at Probe F were on average 14% smaller than target values. Similar differences were also noted in the single-floe experiments.

5.2.3 Test conditions

Three target wave amplitudes $a_{\text{target}} = 10\,\text{mm}$, 20 mm and 40 mm, equivalent to ones used in the single-floe experiments, were tested. Eight wave frequencies between $f = 0.5\,\text{Hz}$ to $1.5\,\text{Hz}$ were also tested. The corresponding nondimensional wavelengths ranged from $\lambda/D = 1.7$ to 12.3. Compared to the single-floe experiments, a narrower range of wavelengths was selected to increase the resolution of results in the regimes where collisions occurred. These regimes were roughly determined in preliminary tests. Table 5.2.1 gives the wave conditions for all tests. The corresponding target wave steepnesses ranged from $ka = 0.013$ to 0.364. In the single-floe experiments, wave breaking was observed when ka exceeded 0.21, approximately. In Table 5.2.1, tests with wave steepnesses greater than 0.21 are highlighted in red. These tests were still performed as they constitute a significant portion of the collision regime. Again this was established through preliminary tests.

f [Hz]	0.5	0.75	1	1.1	1.2	1.3	1.4	1.5
λ [m]	4.91	2.67	1.56	1.29	1.08	0.92	0.8	0.69
$a = 10\,\text{mm}$	•	•	•	•	•	•	•	•
$a = 20\,\text{mm}$	•	•	•	•	•	•	•	•
$a = 40\,\text{mm}$	•	•	•	•	•	•	•	

Table 5.2.1: Summary of test matrix for two-floe non-rafting experiments. Red bullets indicate tests with target wave steepnesses, $ka > 0.21$.

A total of 23 combinations of wave amplitudes and frequencies were tested. Each wave condition in Table 5.2.1 was repeated at least once. Overall, 62 tests (which is inclusive of 39 repeated tests) were conducted. However, only data from 47 tests were extracted. A number of tests were unsuccessful due to erroneous Qualisys data. As mentioned previously, this resulted from markers frequently merging on the IR image due to the close proximities of the floes. In a number of short-wavelength tests, floes collided with the wave probes due to strong drift. When this occurred, wave probes were repositioned, and tests were repeated.

5.2.4 Data processing

Qualisys records the motions of each floe relative to their respective initial positions. Therefore each floe has its own coordinate system. The two coordinate systems can be combined into one by considering the initial separation s_0 between floes. Collision events are then determined from this combined coordinate system by comparing the motions of Floes F and R in the x-axis at their closest edges. In general, a collision event occurs when the x-coordinates of their edges are equivalent, or slightly overlap. Note that the overlap is to account partly for the fact that s_0 may not be exactly 20 mm due to small disturbances in the basin.

The x-coordinate of the trailing edge of Floe F is denoted as $\widehat{X}_F(t)$, and is simulated using the position of its geometric centre, i.e. $\widehat{X}_F(t) \approx X_F(t)$. This approximation allows the horizontal location of the edge to be derived directly from the x-displacement of the floe without considering pitch. The position of leading edge of Floe R is also approximated as $\widehat{X}_R(t) \approx X_R - D$. Small changes to the x-coordinates at the edges, due to rotations in pitch, are not significant. For the steepest waves tested ($ka = 0.364$, which corresponds to a maximum pitch angle of 20 degrees), $\widehat{X}_F$ and $\widehat{X}_R$ are calculated to be within 6% of the actual x-coordinates at their respective trailing and leading edges.

A collision detection algorithm is implemented to merge the two coordinate systems and correctly identify collision events. The following is a simplified version of the algorithm proposed by Bennetts et al. (2014). For tests where collisions occurred (based on recorded observations), the following steps are applied.

1. Calculate the instantaneous separation, $s(t) = \widehat{X}_F(t) - \widehat{X}_R(t)$, where $\widehat{X}_R(t) = X_R(t) - D + \varepsilon$. Assume that the tuning parameter $\varepsilon = 0$.

2. Provisionally identify collision times t_c. Collisions occur when $s(t) \leq 0$.

At this point, some collision events may not be correctly identified. This depends on whether $\widehat{X}_F$ and $\widehat{X}_R$ are too close or too far apart. As discussed previously, small errors are introduced when approximating the x-coordinates of the edges of Floes F and R. Additional errors may also be introduced if $X_F(0) \neq 0$ and/or $X_R(0) \neq 0.42\,\mathrm{m}$ at the start of each test.

Figure 5.2.3 shows an example of too many collision events being identified as a result of the signals being too close together. Four collision events (red bullets) are identified when only one event should have occurred. This is confirmed via video recordings.

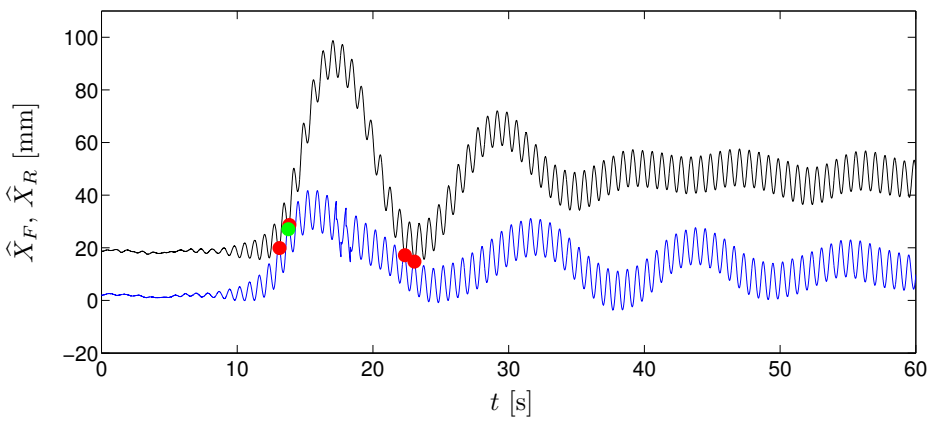

Figure 5.2.3: Example of falsely acquired collision events (•) due to over-merged signals of Floes F (−) and R (−). Only one actual collision event (•) should occur.

The following steps are applied to adjust the separation between Floes F and R by tuning $\widehat{X}_R$ via the parameter ε.

3. Increase or decrease ε until $\widehat{X}_F(t_c) - \widehat{X}_R(t_c)$ is within a tolerance of 5 mm at all collision times t_c.

4. Merge all collision times within a 2 s radius interval. Identify merged collision times as a single collision event.

5. Confirm that the number of collision events n_c from step 4 corresponds with the number of collisions from recorded observations.

6. If n_c is different from observations, manually adjust ε until their values are consistent.

For the example in Figure 5.2.3, the single recorded collision event (green bullet) is correctly identified when a tuning parameter $\varepsilon = 3\,\text{mm}$ is introduced.

5.3 Results

The following link contains the complete dataset for the non-rafting experiments: `https://github.com/AdelaideUniversityMathSciences/TwoFloeCollisionModels/tree/master/TwoFloeExperiments/NonRaftingExperiments`.

5.3.1 Collision regimes

Collision behaviours are qualitatively analysed with respect to incident wave conditions. Three distinct collision behaviours were observed in the experiments:

(i) Floes did not come into contact at all throughout a given test. This generally occurred in the longest and shortest wavelengths.

(ii) Floes collided repeatedly at near constant time intervals. This occurred throughout a wide spectrum of wavelengths. Collisions were mostly characterised by forceful impacts. Weak collisions occurred only in a handful of tests.

(iii) Floes collided 1 to 3 times in the initial phases, and remained separated thereafter. The mean steady-state separation was noted to be approximately constant. This behaviour predominantly occurred in very short wavelengths, and was associated with large amounts of scattered waves.

The collision behaviours for all tests are shown in Figure 5.3.1. Here, collision regimes are distinguished according to the number of collision events over a 60 s interval. Tests with 1 to 3 collisions are differentiated from tests with more than 3 collisions and tests with no collisions. Results are plotted as functions of measured incident wave amplitudes (taken from Probe F) and nondimensional wavelength.

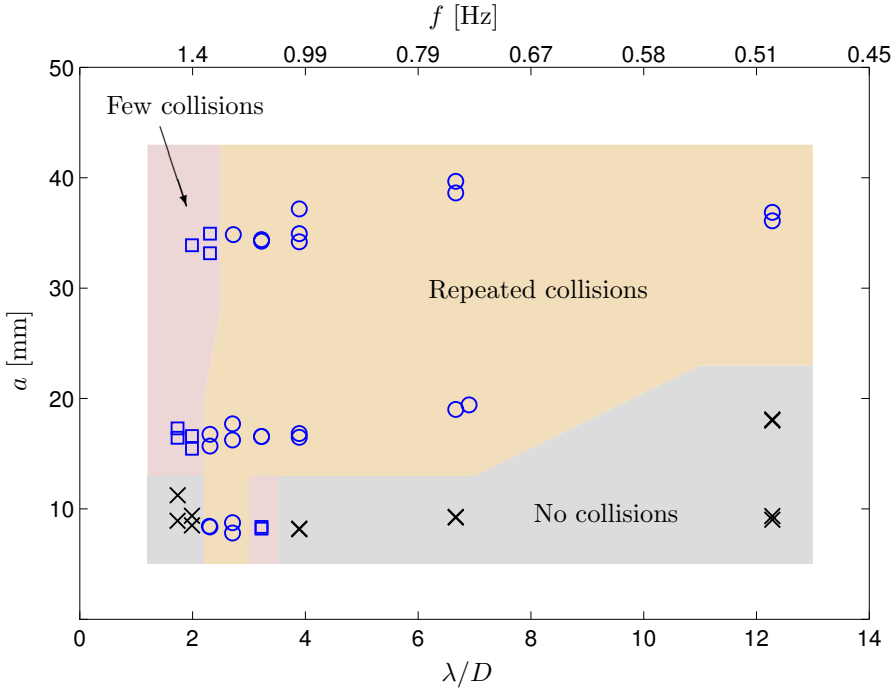

Figure 5.3.1: Collision regimes as a function of incident wave amplitude and nondimensional wavelength. Tests with more than 3 collisions (○), 1 to 3 collisions (□), and no collisions (×).

For the smallest wave amplitudes tested ($a_{\text{target}} = 10\,\text{mm}$), no collisions occur in the shortest two and longest three wavelengths. Floes therefore exhibit behaviour (i). In short waves, surge amplitudes are small compared to the floe separation, therefore collisions do not occur. In long waves, collisions do not occur because of the approximately synchronous surge motions. Collisions only occur between $\lambda/D = 2.3$ to 3.2. In the case of $\lambda/D = 3.2$, only a single collision event was observed. This regime represents the transition between repeated collisions and no collisions.

When the target wave amplitude is increased to $a_{\text{target}} = 20\,\text{mm}$, collisions occur over a larger range of wavelengths. Figure 5.3.1 shows that collisions occur in all but the longest wavelength $\lambda/D = 12.3$. In the shortest two wavelengths, $\lambda/D = 1.7$ and 2, collisions are unsustained and exhibit behaviour (iii).

Further increasing a_{target} to 40 mm causes collisions to occur in all wavelengths considered. In wavelengths less than $\lambda/D = 2.7$, collisions do not exceed 3 events. Repeated collisions only occur in the long-wavelength regime.

Figure 5.3.2 shows examples of the three collision behaviours. In the figure, $\widehat{X}_F$ and $\widehat{X}_R$ are plotted over a 60 s interval. Results for two target wave amplitudes

(a_{target} = 10 and 20 mm) and four wave frequencies (f = 1.5, 1.2, 1.1 and 0.5 Hz) are shown. The corresponding nondimensional wavelengths are λ/D = 1.7, 2.7, 3.2 and 12.3.

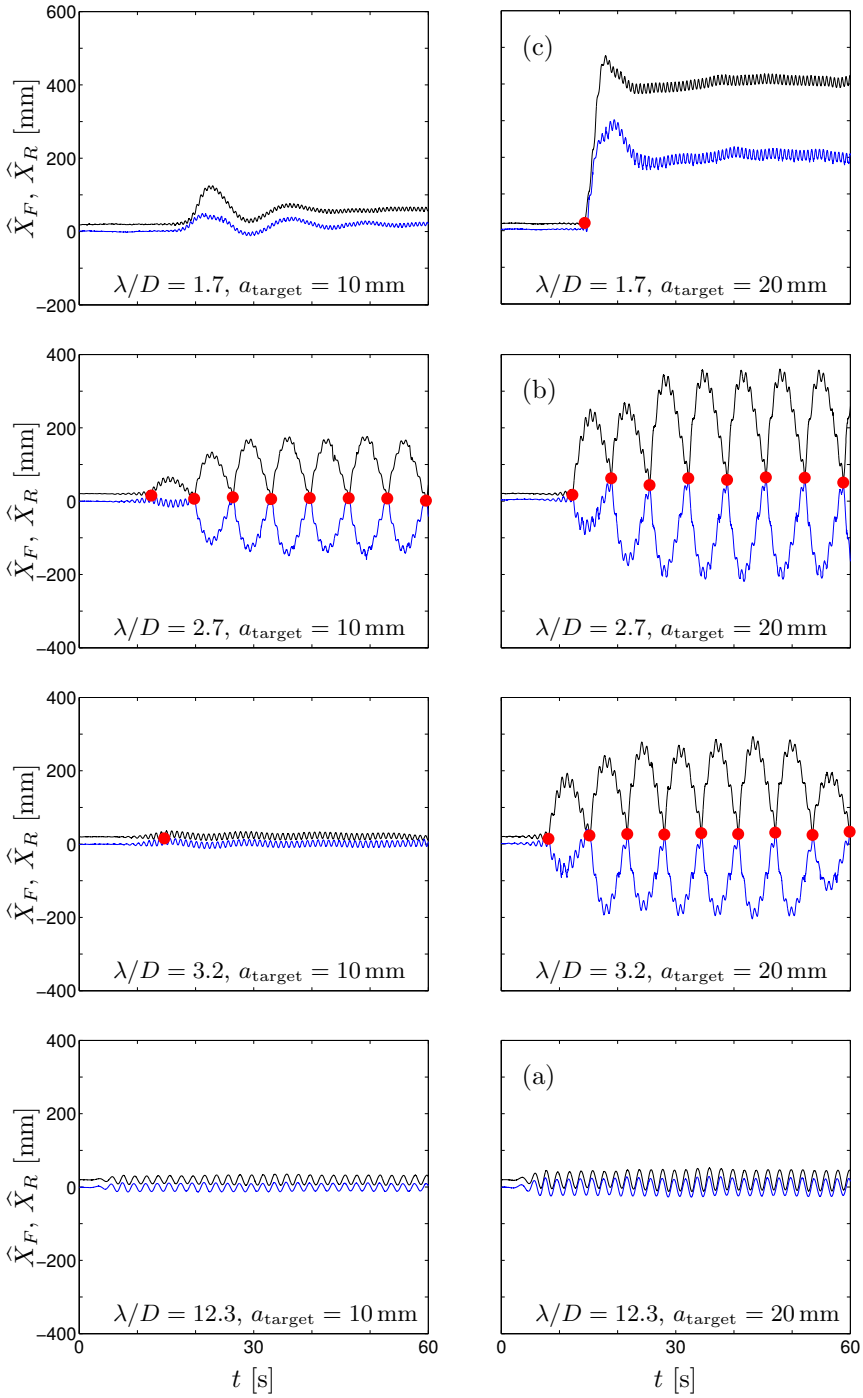

Figure 5.3.2: Motions of Floes F (−) and R (−) in the x-axis for target wave amplitudes $a = 10$ mm (left panels), $a = 20$ mm (right), and incident wave frequencies f = 1.5, 1.2, 1.1, 0.5 Hz (top to bottom panels, respectively). Collision events are indicated (•). Tests (a), (b), and (c) are example cases which relate to the images in Figure 5.3.3.

For the smallest wave amplitude $a_{\text{target}} = 10\,\text{mm}$ and wavelength $\lambda/D = 1.7$, no collisions occur during the test. Floe-floe interactions are characterised by behaviour (i). Surge amplitudes are visibly small compared to the initial separation. The mean steady-state surge amplitude, which is calculated using the procedure outlined in § 2.2.6, is $a_s = 4.68\,\text{mm}$ for Floe F and 4.91 mm for Floe R. Collisions do not occur in this test because the average surge amplitude is less than half of the initial separation, i.e. $a_s < s_0/2$.

However, a collision event almost occurs at $t \approx 20\,\text{s}$. At their closest, the separation between both floes was 2.8 mm. The reason for this small separation is due to drift. Note that surge amplitudes are relatively small compared to the initial separation. In § 2.3.2, it was shown that drift velocities were largest in the short-wavelength regime, and increased with wave steepness. The top- and bottom-most panels in Figure 5.3.2 also demonstrates this for two floes. In the longest wavelengths considered, drift is virtually absent.

Moving on from the top-left panel of Figure 5.3.2, when the incident wave amplitude is increased to 20 mm, a single collision event occurs. This test is labelled example (c) in Figure 5.3.2. Collision behaviour (iii) best describes this test. After the initial collision, the floes drift in the direction of the incident wave for about 4 s, then approach an equilibrium separation of approximately 200 mm after 24 s. This separation is considerably larger than s_0. A larger equilibrium separation also occurs when $a_{\text{target}} = 10\,\text{mm}$ and $\lambda/D = 1.7$. In this wavelength regime, significant amounts of scattered waves develop between the floes. Recall that in the single-floe experiments, wave scattering was observed to increase with decreasing wavelength (see § 2.3.1 and Figure 2.3.2). The bottom panel of Figure 5.3.3 shows the surrounding wavefield for example (c). Larger separations are attributed to strong wave forces between the floes due to scattered waves. In this regime, wave forces are, to a certain degree, strong enough to overcome the restoring forces from the mooring system.

As wave scattering diminishes with increasing incident wavelengths, wave forces between floes decrease. The top-right panel of Figure 5.3.3 shows the wavefield for example (b) in Figure 5.3.2. Here, $\lambda/D = 2.7$ and $a_{\text{target}} = 20\,\text{mm}$. In this example, wave forces are weak enough for restoring forces to influence floe motions and induce

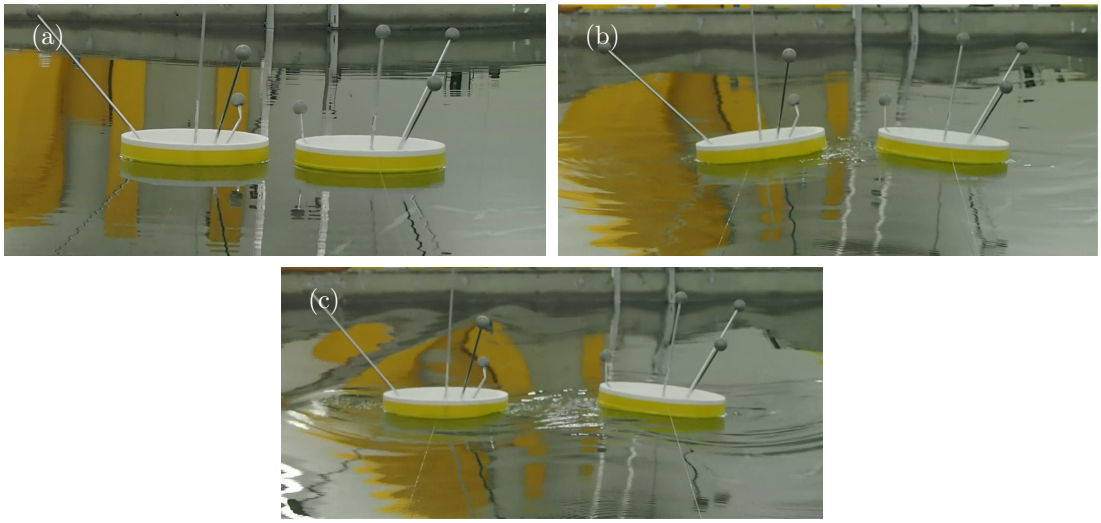

Figure 5.3.3: Images of floes and surrounding wavefields in wave conditions correspond to tests (a), (b) and (c) in Figure 5.3.2.

repeated collisions.

Floe-floe interactions in example (b) exhibit behaviour (ii), i.e. floes collide repeatedly. Collisions generally occur at regular intervals in tests with repeated collisions. In this test, the periods between successive collisions are fairly consistent, with the maximum and minimum periods at 6.68 s and 6.59 s, respectively. The average period over the 60 s window is 6.65 s. This behaviour is also evident when a is decreased to 10 mm.

Further increasing wavelengths to $\lambda/D = 3.2$ (whilst $a_{\text{target}} = 10\,\text{mm}$) results in collisions transitioning to behaviour (iii). However in this scenario, wave scattering is minimal and floes do not have large mean steady-state separations. In this test, the average steady-state surge amplitude is 8.51 mm, which is below the value of $s_0/2$. This implies that drift rather than surge is responsible for causing floe collisions. Floes collide only once with minimal force. In § 5.3.2, we will quantify and investigate collision forces in greater detail.

When a_{target} increases to 20 mm (whilst $\lambda/D = 3.2$), the average surge amplitudes increase to 16.17 mm. This value was extracted from the discrete Fourier transform of $\widehat{X}_F$ and $\widehat{X}_R$, using the `fft` package on MATLAB. Note that the smoothing method employed in Chapter 2 (see § 2.2.6) is not suitable here due to the nature of the post-collision displacements. Since a_s is now larger than $s_0/2$, surge becomes the dominant motion affecting collisions. As a result, collisions transition from a single

event (when $a = 10\,\text{mm}$) to repeated collisions (when $a = 20\,\text{mm}$).

For the largest wavelengths considered in Figure 5.3.2, no collisions occur for both wave amplitudes. These tests are another example of behaviour (i). Despite surge amplitudes being larger than the initial separation, Floes F and R do not come into contact because both floes surge approximately in phase with each other. This phenomenon is commonly observed in the long-wavelength regime. The test with the largest wavelength and wave amplitude is denoted as example (a) in Figure 5.3.2. The top-left panel of Figure 5.3.3 shows the corresponding wavefield. In this example, there are no visible modifications to the wavefield.

Video recordings of examples (a), (b) and (c) can be downloaded through the link `https://github.com/AdelaideUniversityMathSciences/TwoFloeCollisionModels/tree/master/TwoFloeExperiments/NonRaftingExperiments/Videos`.

5.3.2 Collision frequency and velocity

In the preceding section, we saw that collision behaviours were defined by the number of collisions and forcefulness of impacts. Collision behaviours are therefore quantified in terms of the mean collision frequency $\overline{f}_c$ and mean collision velocity $\overline{V}_c$. The mean collision frequency is calculated as $\overline{f}_c = 1/\overline{T}_c$, where $\overline{T}_c$ is the average period between successive collisions. The mean collision velocity, which is also an indicator of the strength of collisions, is calculated using the average relative pre-collision velocities of each floe, and averaged over all collisions in a single test. Pre-collision velocities are calculated as the slope of a linear regression of time-series motions in the x-direction, over 10 time steps prior to a collision (Bennetts et al., 2014).

In Figure 5.3.4, the mean collision frequencies and velocities are plotted as functions of incident wave frequency rather than wavelength, for clarity. However, for reference, the corresponding nondimensional wavelengths λ/D are indicated at the top of the horizontal axis. Dashed lines denote the boundary between the long- and short-wavelength regimes, when $\lambda/D = 3$. Results are grouped according to target wave amplitudes, with $a = 10$, 20 and 40 mm shown in the top, middle and bottom panels, respectively.

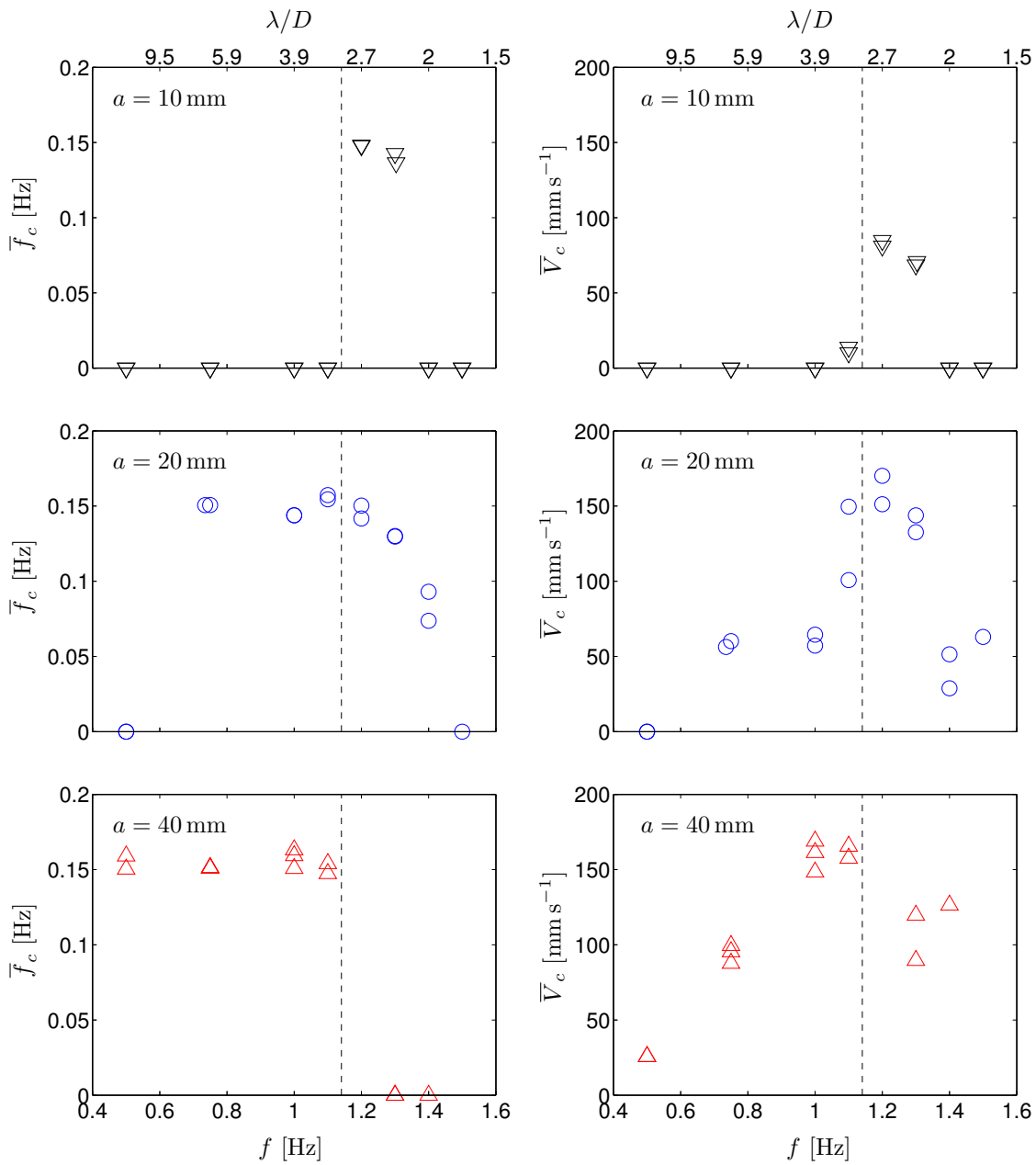

Figure 5.3.4: Mean collision frequencies (left panels) and collision velocities (right panel) as functions of incident wave frequency (and corresponding nondimensional wavelength). Top to bottom panels are for $a = 10$, 20 and 40 mm.

When $a = 10\,\mathrm{mm}$, collisions only occur between $\lambda/D = 2.3$ and 3.2. For $\lambda/D = 3.2$, only one collision event was recorded. In this case, the collision frequency is indicated as zero. For the other two tests, collision frequencies range from 0.137 Hz to 0.148 Hz.

When wave amplitudes are increased to $a = 20$ and 40 mm, more collisions occur over the range of incident wavelengths. Collisions do not occur in the longest wavelength when $a = 20\,\mathrm{mm}$. When collisions occur in the long-wavelength regime, frequencies are relatively consistent. Collision frequencies range from 0.144 Hz to 0.157 Hz. Frequencies for all tests do not exceed 0.163 Hz.

In the short-wavelength regime, when $a = 20\,\mathrm{mm}$, collision frequencies increase with increasing wavelength. Frequencies range from 0.074 Hz (when $\lambda/D = 2$) to 0.15 Hz (when $\lambda/D = 2.7$). When a increases to 40 mm, only one collision event occurs for $\lambda/D = 2$ and 2.3.

The right panels of Figure 5.3.4 show the mean collision velocities over a range of wave frequencies. Collision velocities are indicated as zero when no collisions occur. Collision velocities approach peak values between $\lambda/D = 2.3$ to 3.9. Mean collision velocities are lowest in the longest and shortest wavelengths. For example, when $a = 20\,\mathrm{mm}$, velocities are least when $\lambda/D = 2$ and 6.9. Low collision velocities can be attributed to small surge amplitudes in short waves, and small relative surge motions in long waves. We can cross reference the former explanation to the results from the single-floe experiments, which show that when $\lambda/D = 2$, the surge RAO is approximately 0.67 (based on the trend line of Floe B – see § 2.3.1, Figure 2.3.3). As for the latter, explanations on relative surge will be discussed in the next section.

Collision velocities generally increase proportionally with wave amplitude. For example when $\lambda/D = 2.7$, mean velocities (with respect to wavelength) increase from 85 to 170 $\mathrm{mm\,s^{-1}}$ when a increases from 10 to 20 mm. This proportionality of collision velocities is also evident when a is increased from 20 to 40 mm. It is expected that collision velocities are proportional to wave amplitude due to the linearity of oscillatory motions with respect to wave amplitude (see § 2.3.1).

5.3.3 Surge

Figure 5.3.5 shows the comparison between surge RAOs of Floes F and R, and Floe B from the single-floe experiments. The trend line for Floe B, as per Figure 2.3.3, is also presented. RAOs for Floes F and R are calculated using the discrete Fourier transform (DFT) method, while the RAOs for Floe B were found using the smoothing method (see § 2.2.6). As mentioned previously, the smoothing method is not appropriate when displacements are affected by collisions. When collisions occur, horizontal motions due to drift and mooring forces are not as easily isolated from the full signal. In this situation, the DFT method is employed to extract the surge amplitudes from the frequency spectrum of x-displacements. Again, this process is performed using the `fft` package on MATLAB. Both DFT and smoothing methods gave comparable results. For example, the average difference between surge amplitudes of Floe B calculated using the DFT method was -7.5% that of the smoothing method.

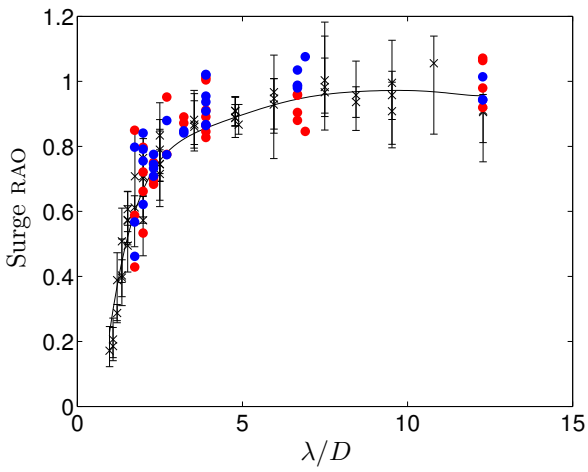

Figure 5.3.5: Surge RAOs of Floe F (•) and Floe R (•) in comparison to that of Floe B (×) from the single-floe experiments. Black curve represents the trend line of Floe B as presented in Figure 2.3.3.

Figure 5.3.5 shows that the RAOs for Floes F and R are generally consistent with Floe B. The mean RAOs (with respect to incident wavelength) of Floe F and Floe R are within 4.6% and 0.2% of the trend line, respectively. Despite using a tighter mooring system and positioning the floes close to each other, surge RAOs are still comparable. This result also indicates that surge motions are unaffected by the collision process.

In § 5.3.1, several examples were given to show how the relative phases of surge motions affect collision behaviours. In the long-wavelength regime, it was shown that no collisions occur due to small relative phases. Here, the relative surge motions of Floes F and R are quantified and compared with the occurrence of collisions.

Relative surge (ΔSurge) is calculated as

$$\Delta\text{Surge} = \left|\overline{a}_s(\mathrm{e}^{\mathrm{i}\varphi_F} - \mathrm{e}^{\mathrm{i}\varphi_R})\right|, \tag{5.3.1}$$

where φ_F and φ_R are, respectively, the phases of Floes F and R. For tests with collisions, the phases are calculated using the local maxima of $\widehat{X}_F$ and $\widehat{X}_R$ just before the first collision event occurs. Figure 5.3.6 shows an example of this. The local maxima of Floes F and R are indicated by the blue and black crosses respectively. The phase of Floe F is calculated as $\varphi_F = \omega t_{\max}$, where $t_{\max}$ denotes the time when $\widehat{X}_F$ is at its local maximum, and ω is the angular wave frequency. The phase of Floe R is calculated similarly. For tests without collisions, phases are calculated using a local maxima within the steady-state interval. Periods between successive peaks are consistent, therefore the relative surge calculated in (5.3.1) will not largely vary if different local maxima are chosen. For instance, in example (a) in Figure 5.3.2, the difference between the maximum and minimum period of Floe R is less than 2.5% of the mean period.

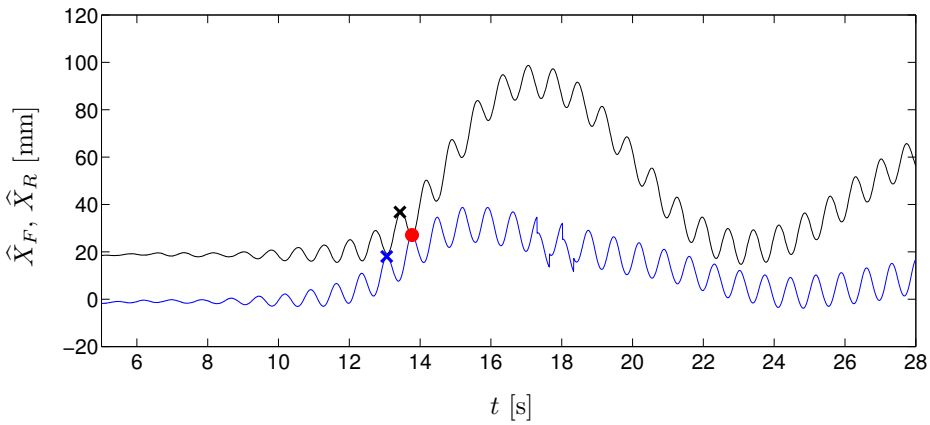

Figure 5.3.6: Example of how the relative surge is calculated using the local phases of Floes F (×) and R (×).

In Equation (5.3.1), the term $\overline{a}_s$ denotes the mean steady-state surge amplitude for both floes. This quantity is obtained from the DFT of steady-state displacements

of Floes F and R. Recall the steady-state intervals are calculated using the phase velocity $c = f\lambda$ (see § 2.2.6).

The relative surge calculated in Equation (5.3.1) corresponds to the maximum difference between the surge only signals of Floes F and R over one wave period, i.e. $\widetilde{X}_F - \widetilde{X}_R$. Here $\widetilde{X}_F = \mathrm{Re}\{\overline{a}_s \mathrm{e}^{\mathrm{i}(\varphi_F + \omega t)}\}$ and $\widetilde{X}_R = \mathrm{Re}\{\overline{a}_s \mathrm{e}^{\mathrm{i}(\varphi_R + \omega t)}\}$ are the surge only signals of $\widehat{X}_F$ and $\widehat{X}_R$.

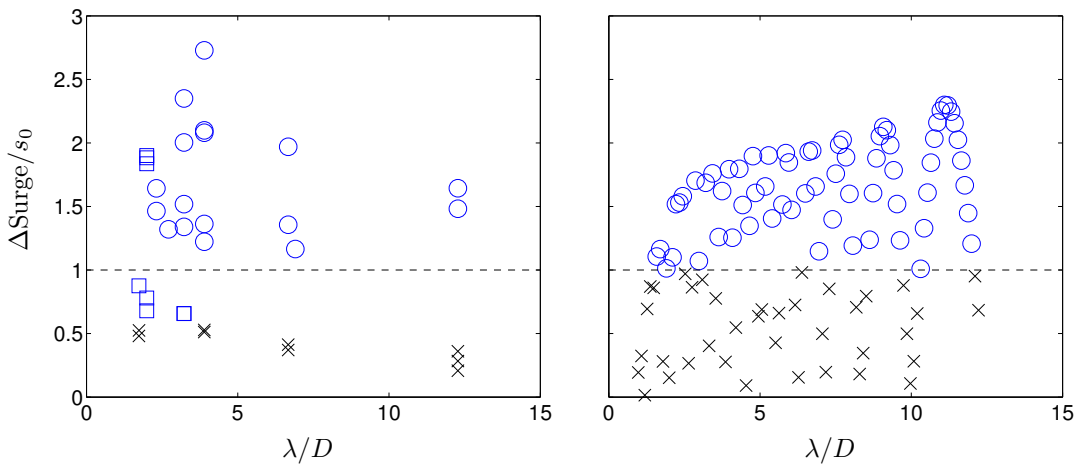

Figure 5.3.7: Normalised relative surge as a function of nondimensional wavelength. Left panel: Data from non-rafting experiments. Symbols as with Figure 5.3.1. Right panel: Data from two-floe simulations using surge RAOs from the single-floe experiments. Here ○ and × simply denote the occurrence of collisions and no collisions, respectively.

Figure 5.3.7 shows the relative surge as a function of nondimensional wavelength. Relative surge is normalised with respect to the initial separation s_0, such that when $\Delta\mathrm{Surge}/s_0 = 1$, the curves $\widetilde{X}_F$ and $\widetilde{X}_R + s_0$ intersect. This indicates collisions due to surge. The left panel of Figure 5.3.7 shows results from the experiments. Tests are categorised according to the number of collision events in each test, as per Figure 5.3.1.

Results from the single-floe experiments are also used to predict the occurrence of collisions. Relative surge is calculated by using the surge amplitudes of Floe B in place of $\overline{a}_s$ in Equation 5.3.1. Surge amplitudes are obtained from the trend line of Floe B in Figure 5.3.5. The phases of Floes F and R are also modified such that $\varphi_F = 0$ and $\varphi_R = k(s_0 + D)$. This accounts for the phase shift due to the separations of the floes. The right panel of Figure 5.3.7 shows the normalised relative surge calculated over 103 intervals from $\lambda/D = 1$ to 12.2. Collision events are noted when

the curves $\widetilde{X}_F$ and $\widetilde{X}_R + s_0$ intersect. The right panel of Figure 5.3.7 shows that all instances of collisions are associated with the relative surge being larger than the initial separation.

In the experiments, when wavelengths $\lambda/D > 3.8$, $\Delta\text{Surge}/s_0$ is always greater than 1 when collisions occur, and less than 1 when collisions do not occur. The top panel of Figure 5.3.8 shows an example of collisions due to surge. This test corresponds to example (b) in Figure 5.3.2, however, here, the time-scale is enlarged around the first collision event. In this figure, the steady-state surge signals $\widetilde{X}_F$ and $\widetilde{X}_R + s_0$ are overlaid. Both curves intersect, implying that surge is large enough and sufficiently out of phase to cause collisions. The relative surge here is $\Delta\text{Surge}/s_0 = 1.28$.

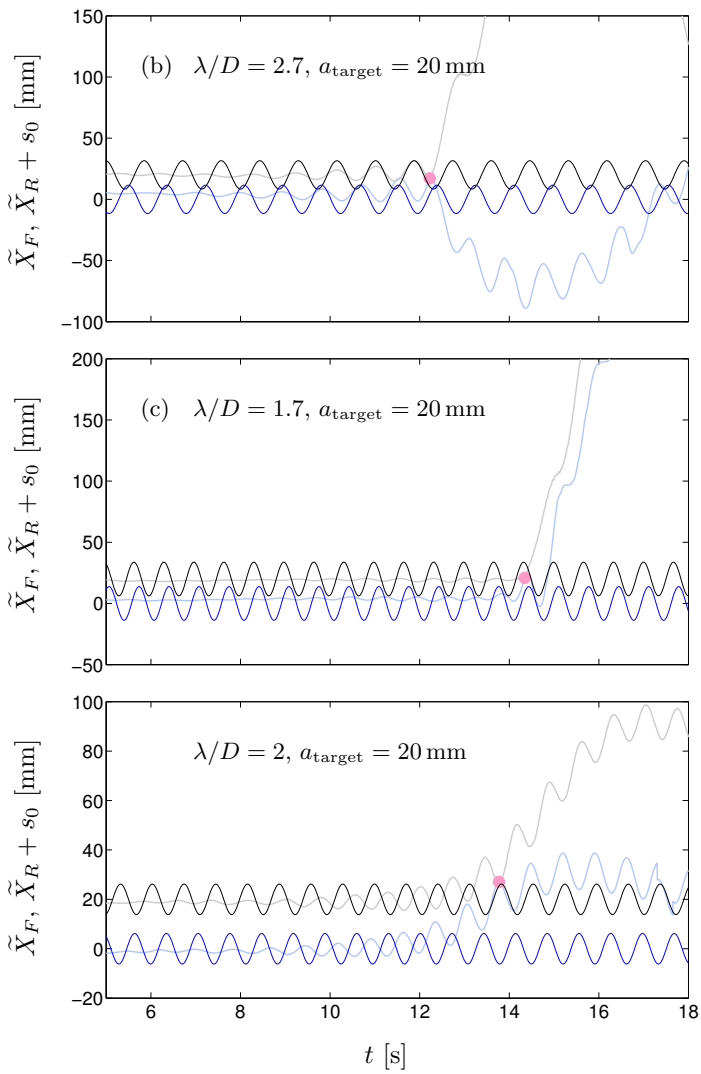

Figure 5.3.8: Examples of collisions caused by surge (top panel) and drift (middle and bottom). Shaded curves denote full signals, as per Figure 5.3.2. Blue and black curves indicate steady-state surge signals for Floes F and R.

When $\lambda/D < 3.8$, $\Delta\text{Surge}/s_0$ was less than 1 for five tests in which collisions occurred. In each of these tests, the number of collision events were between 1 to 3. One of these tests is example (c) in Figure 5.3.2. The middle panel of Figure 5.3.8 shows the time-series of example (c) around the first (and only) collision event. Again, the surge signals $\widetilde{X}_F$ and $\widetilde{X}_R + s_0$ are overlaid. Both pairs of curves do not intersect. Although the relative surge $\Delta\text{Surge}/s_0 = 0.72$ is less than 1, a collision still occurs. The collision event here is attributed to the differential drift between floes. When the first incident wavefronts reach the floes, they interact with Floe F first. This causes Floe F to start drifting before Floe R.

The bottom panel of Figure 5.3.8 shows another example of collisions caused by drift. The effect of differential drift is much more evident. In this test, the surge amplitudes are clearly smaller than the initial separation. Furthermore the relative surge $\Delta\text{Surge}/s_0 = 0.61$. However a single collision event still occurs as a result of the differential drift in the first few seconds of the test.

5.4 Summary

The second round of wave basin experiments investigated non-rafting collisions between two adjacent floes. Both floes were identical to the ones used in the previous single-floe experiments. Both had edge barriers installed to prevent rafting. Tethers were installed on both floes to induce repeated collisions. The motions of both floes were recorded in incident wavelengths 1.7 to 12.3 times the floe diameter, and in wave steepnesses between 0.01 to 0.36.

Collision regimes were quantified in terms of incident wavelengths and wave amplitudes. Three specific collision behaviours were noted. Floes either (i) collided repeatedly, (ii) collided initially a few times and remained separated, or (iii) did not collide at all. Experimental results showed that:

1. In long wavelengths and small to intermediate wave amplitudes, no collisions occur because floes surge approximately in phase.

2. In short wavelengths and small wave amplitudes, no collisions occur since surge amplitudes are smaller than the initial separation.

3. Collisions occur over a larger range of wavelengths when incident wave amplitudes increase.

In the short-wavelength regime, it was observed that scattered waves prevented floes from colliding continuously. Scattered wave forces between the floes were more significant than the incident wave and mooring forces.

Collision frequencies and velocities were then quantified as functions of incident wavelength and wave amplitude. Results showed that:

1. In the short-wavelength regime, collision frequencies increase with wavelength.
2. In long waves, collision frequencies are fairly uniform with respect to wavelength, and are bounded by a maximum of 0.16 Hz.
3. Collision velocities are greatest in intermediate wavelengths between 2.3 and 3.9 times the floe diameter. Velocities are lowest in the longest and shortest wavelengths due to the relatively similar surge phases (in long waves) and small surge amplitudes (in short waves).
4. Collision velocities increase proportionally with wave amplitude.

Finally, the relative surge of the two floes were quantified with respect to the initial separation, to determine its relationship with the occurrence of collisions. In wavelengths longer than 3.8 times the floe diameter, all instances of collisions coincided with a relative surge greater than the initial separation. This implies that in long waves, collisions are caused by surge. In shorter wavelengths, collisions were caused by either surge or drift. When collisions were caused by drift, the relative surge was less than the initial separation. Collisions were also simulated using the surge amplitudes from the single-floe experiments, however they could not be used to predict collisions due to drift in the short-wavelength regime.

Chapter 6

The two-floe collision model

In this chapter, a theoretical two-floe collision model is developed to simulate the wave-induced motions of two adjacent floes. The following sections describe how the model is developed to replicate the two-floe system in the collision experiments of Chapter 5. Results from the two-floe non-rafting experiments are then used to validate the theoretical model.

6.1 Collision algorithm

A collision model is developed to simulate the wave-induced floe-floe collisions of a two-floe system. The main purpose of the model is to (i) predict the occurrence of collisions, and (ii) predict collision properties (collision frequencies and velocities) over a range of incident wave conditions. The model utilises a time-stepping algorithm, and is derived by coupling single-floe models together to simulate collisions.

The model is initialised by specifying the following input parameters:

1a. Define all physical parameters: incident wave conditions (wavelength, wave amplitude, water depth), and floe properties (diameter, thickness, density).

1b. Set initial conditions: initial displacements and velocities of each floe.

1c. Set simulation parameters: resolution and length of time step, and number of collisions to be extracted. A sufficiently high time-resolution of 100 Hz was

used to generate accurate simulations of collisions.

The motions of two floes are then simulated as follows:

2a. Use equations of motion to calculate the horizontal x-displacements of Floes F and R (X_F and X_R) separately, over 60 s. Recall, Floe F and Floe R refer to the front and rear floes with respect to the origin of the incident wave. (Note that all naming conventions are consistent with Chapter 5.)

2b. At each time step, compare the x-displacements of both floes at their closest edges to determine if a collision has occurred.

For the purposes of determining collision events, floes are visualised as one-dimensional planes. Figure 6.1.1 illustrates this. A collision event is defined to occur when the x-coordinate of the trailing edge of Floe F overlaps with the leading edge of Floe B. Translations in the x-axis and rotations about the centre of each floe (pitch) are taken into account when calculating edge locations.

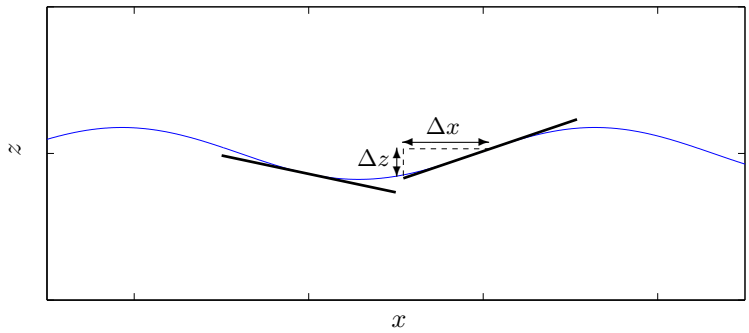

Figure 6.1.1: Visualising floes as 1-D planes.

If Δz and Δx denote the vertical and horizontal distances between a floe's centre and its edge, respectively, and $\Delta z/\Delta x = \tan\Theta$, where Θ is the pitch angle, then

$$\Delta x = \frac{R}{\sqrt{1+\tan^2\Theta}}, \qquad \text{where } R = \sqrt{\Delta x^2 + \Delta z^2} \tag{6.1.1}$$

is the floe radius.

Hence, the x-coordinate of the trailing of Floe F is

$$\widehat{X}_F(t) = X_F(t) + \frac{R}{\sqrt{1+\tan^2\Theta_F(t)}}, \tag{6.1.2}$$

and the x-coordinate of the leading edge of Floe R is

$$\widehat{X}_R(t) = X_R(t) - \frac{R}{\sqrt{1 + \tan^2\Theta_R(t)}}. \tag{6.1.3}$$

Note that $\Theta_F(t)$ and $\Theta_R(t)$ denote the instantaneous pitch angles of Floes F and R, respectively. Collisions therefore occur when $\widehat{X}_R(t) - \widehat{X}_F(t) \leq 0$.

If no collision events occur over 60 s, the simulation is stopped. If a collision event occurs, the following steps are performed:

3a. Save the time of collision t_c, and save the displacements (X_F and X_R) and velocities (V_F and V_R) of both floes at t_c. Velocities are calculated from the slope of the displacement time-series between t_c and one time step before t_c.

3b. Truncate X_F and X_R at t_c and save all displacements prior to t_c.

3c. Calculate the post-collision velocities of both floes.

Post-collision velocities and displacements at t_c are used as new initial conditions for simulations of floe motions after a collision event. The process of calculating the post-collision velocities is as follows.

In our model, floes are represented as rigid bodies, and their collisions are modelled after Herman (2011, 2012, 2013), who calculated the post-collision velocities of each floe using the conservation of linear momentum and kinetic energy equations. The pre- and post-collision velocities of two identical colliding floes are related through the conservation of momentum equation,

$$m(V_{Fi} + V_{Ri}) = m(V_{Ff} + V_{Rf}). \tag{6.1.4}$$

In Equation (6.1.4), V_F and V_R are the horizontal velocities of Floes F and R, respectively. The lower-case subscripts, i and f, refer to their initial and final states (i.e. pre- and post-collision).

If we assume that collisions are perfectly elastic (i.e. no energy is lost during a collision), conservation of kinetic energy requires that

$$\frac{1}{2}m(V_{Fi}^2 + V_{Ri}^2) = \frac{1}{2}m(V_{Ff}^2 + V_{Rf}^2). \tag{6.1.5}$$

If collisions are inelastic and energy is lost, a coefficient of restitution, ϵ, is defined so that

$$\epsilon = \frac{V_{Rf} - V_{Ff}}{V_{Fi} - V_{Ri}} \tag{6.1.6}$$

is satisfied in place of Equation (6.1.5). (For perfectly elastic collisions, $\epsilon = 1$. For perfectly inelastic collisions, $\epsilon = 0$.) Post-collision velocities are then calculated by solving Equations (6.1.4) and (6.1.6) simultaneously. This gives

$$V_{Ff} = \frac{(1-\epsilon)V_{Fi} + (1+\epsilon)V_{Ri}}{2} \quad \text{and} \quad V_{Rf} = \frac{(1+\epsilon)V_{Fi} + (1-\epsilon)V_{Ri}}{2} \tag{6.1.7}$$

For perfectly elastic collisions, this reduces to $V_{Ff} = V_{Ri}$ and $V_{Rf} = V_{Fi}$.

Once the post-collision velocities, and hence new initial conditions, are found, they are fed back into the equation of motion to simulate post-collision displacements. Steps 2a and 2b are repeated until the next collision event occurs. Simulations cease when no more collisions occur after an additional 60 s, or if a predefined number of collision events (defined in step 1c) have occurred. The final step is to combine all truncated signals for Floes F and R.

Figure 6.1.2 summarises the basic structure of the two-floe collision model using a process flowchart. The MATLAB code for this model is available at `https://github.com/AdelaideUniversityMathSciences/TwoFloeCollisionModels/tree/master/NonRaftingCollisionModel`.

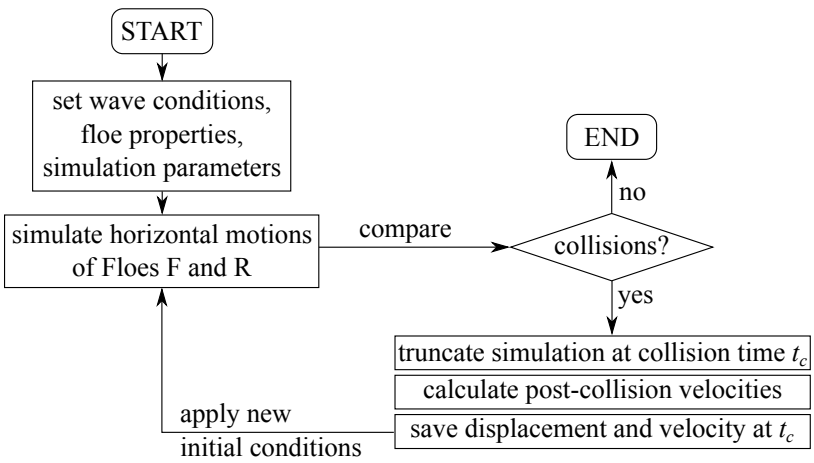

Figure 6.1.2: Flowchart summarising the collision algorithm.

6.2 Simulating floe displacements

6.2.1 Equation of motion

The horizontal motions of each floe are simulated by applying the slope-sliding model described in Chapter 3. This model is integrated into the simulation kernel (step 2a, § 6.1) of the collision model. The slope-sliding model is chosen over the linear potential-flow model for several reasons. First, the current linear potential-flow model can only be used to predict oscillatory surge, heave and pitch motions. Drift, which was shown in § 5.3.3 to be an important part of the collision process, is not inherent to the linear potential-flow model (due to the assumptions of small floe-motions relative to incident wavelength). At present, drift can only be simulated using the slope-sliding model. Note that Faltinsen (1990, Chapter 5) describes how drift forces can be calculated from solutions to the linear potential-flow problem using Maruo's formula, however this thesis does not investigate how this method might be used to integrate drift into the potential-flow model. Another reason for using the slope-sliding model is the inclusion of tuning parameters for added mass and drag, both of which are not available in the potential-flow model. Recall (from § 3.4) that added mass affects surge motions and drag influences drift.

The slope-sliding equation of motion (3.1.1) is modified to account for resistive forces in the two-floe experiments due to the mooring system. These forces are a combination of spring and damping forces. The spring force is modelled using Hooke's law, $F_s = -K\check{X}$, where K is the spring constant and $\check{X} = X - X(0)$ is the displacement of the floe from its initial position. The damping force is proportional to the floe's velocity, i.e. $F_d = -CV$. The coefficient C denotes the damping constant. The modified equation of motion of each floe is therefore

$$m(1 + c_m)\frac{dV}{dt} = -mg\left[\frac{\partial \eta}{\partial x}\right]_{x=X} + \rho c_d W|\widehat{V}|\widehat{V} - K\check{X} - CV. \tag{6.2.1}$$

Note that in step 2b of the collision algorithm, pitch is required to calculate the x-displacements at the floes' edges. In the slope-sliding model, pitch is assumed to correspond with the local wave gradient, therefore $\arctan\Theta = \partial\eta/\partial x$.

6.2.2 Transients in wave forcing

A piecewise wave profile function is implemented to simulate the wave forcing parameters in the two-floe experiments. The incident wave forcing function $\eta(x,t)$ is partitioned into a transient phase and a steady-state phase. From observation, the transient wave profile generally appears to follow a power law function. Therefore in the transient phase, a time-dependent wave amplitude function $\hat{a} = \alpha t^{\beta}$ is used to model the gradual increase in wave amplitude over the initial period. In the steady-state phase, the mean steady-state wave amplitude a is used. Wave profile functions are parameterised through comparisons with wave probe data.

The piecewise wave profile function is defined as

$$\eta(x,t) = \begin{cases} \hat{a}\sin(kx - \omega t + \gamma) & \text{for} \quad 0 \leq t < t_s, \\ a\sin(kx - \omega t + \gamma) & \text{for} \quad t \geq t_s, \end{cases} \tag{6.2.2}$$

where t_s denotes the transient to steady-state time partition. An arbitrary phase angle γ is assigned to both sinusoidal functions. The parameters α, β and γ are obtained by fitting Equation (6.2.2) to wave probe data. This is done by applying the `fit` function in MATLAB. Data from Probe F (located in front of Floe F) is used, since it was closest to the floes. The time partition t_s is selected visually from wave probe data, then adjusted to match the steady-state amplitude. In other words, t_s satisfies the equation

$$\alpha t_s^{\beta}\sin(-\omega t_s + \gamma) = a\sin(-\omega t_s + \gamma). \tag{6.2.3}$$

Figure 6.2.1 shows an example of the parameterised incident wave profile overlaid onto data from Probe F. Wave conditions here are $a = 19.3\,\text{mm}$ and $f = 1\,\text{Hz}$. In this example, the time partition is estimated to occur at approximately 11 s. The first estimate of t_s is used to derive the parameters α, β and γ. The time partition is then fine-tuned to satisfy Equation (6.2.3). The final value of t_s is 10.1 s.

The parameterised incident wave profile provides a generally accurate representation of the measured wave profile. Only small differences are noted in the initial transient phase, due to irregular wave periods measured over the first 5 seconds.

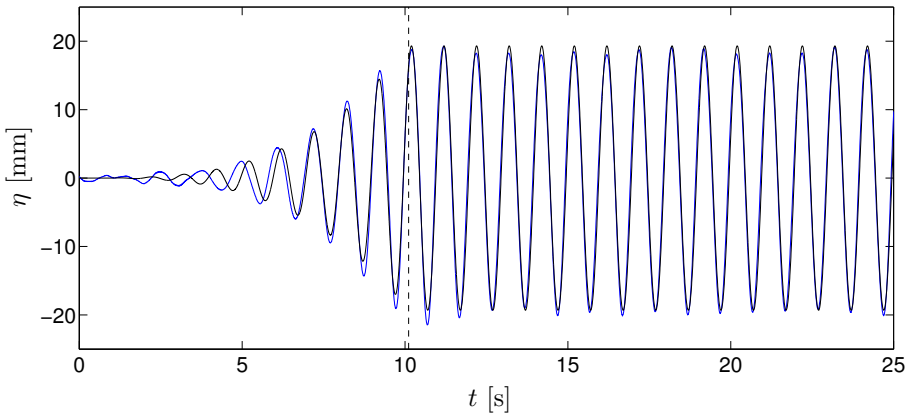

Figure 6.2.1: Parameterised transient and steady-state (−) wave profiles in comparison to measured wave profile (−) from Wave Probe F. Transient to steady-state time partition (- -). In this example $a = 19.3\,\text{mm}$ and $f = 1\,\text{Hz}$.

Once parameterised, the piecewise wave profile function is used to calculate $\partial\eta/\partial x$ and V_w in the equation of motion (6.2.1).

6.2.3 Mooring coefficients

Spring and damping constants, K and C, in Equation (6.2.1), are tuned by comparing simulated horizontal motions with measured x-displacements from the two-floe experiments. Only data from tests without collisions and tests in the long-wavelength regime ($\lambda/D > 3$) are used for tuning K and C. (The translations experienced when floes collide, rebound and drift back toward each other significantly complicate the tuning process. Also, recall that the slope-sliding model is not valid in the short-wavelength regime.) The two coefficients are tuned iteratively using data from these tests until an accurate fit is found. It is assumed that the mooring coefficients for both floes are the same.

The spring constant determines the amplitude of oscillations about the floe's equilibrium position. A larger spring constant implies a stiffer spring system. This translates to smaller oscillatory amplitudes. The top panel of Figure 6.2.2 shows an example of how a floe's simulated response changes when different values of K are used. The measured displacements of Floe F are also shown for comparison. In this test, $a = 8.4\,\text{mm}$ and $f = 1\,\text{Hz}$ ($\lambda/D = 3.9$). The damping coefficient is kept at a constant value of 0.5. The responses of two values of K are shown. The figure shows that the amplitude of long period oscillations is larger when $K = 0.32$ (black curve)

as compared to $K = 0.6$ (magenta). The difference between the overall maximum and minimum is 21.7 mm when $K = 0.32$, and 20.8 mm when $K = 0.6$.

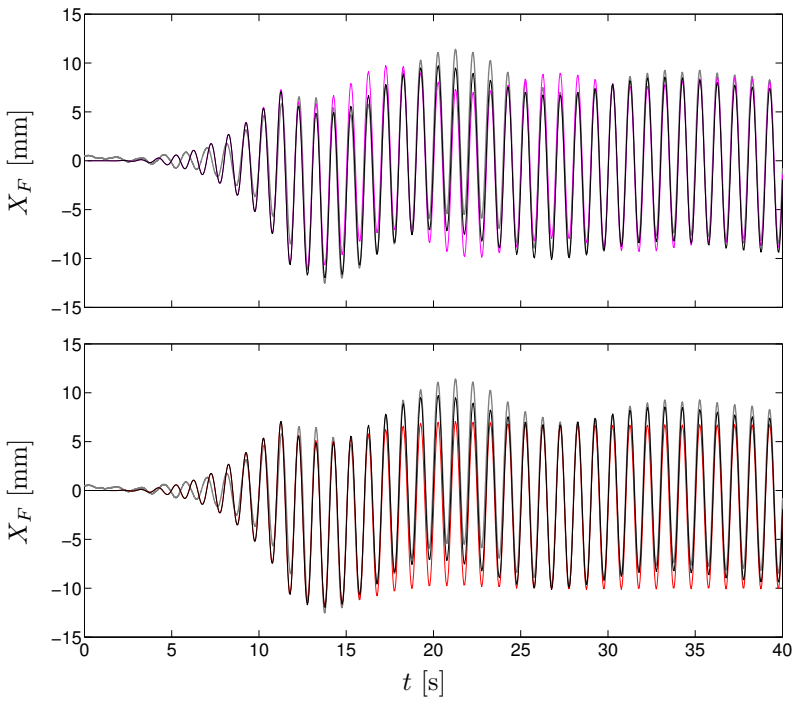

Figure 6.2.2: Effect of spring constant K (top panel) and damping constant C (bottom) on horizontal displacements. Floe displacements simulated using $K = 0.6$ and $C = 0.5$ (−, top panel), $K = 0.32$ and $C = 0.8$ (−, bottom panel), and $K = 0.32$ and $C = 0.5$ (−, both panels) Experimentally measured displacements (−) are shown for comparison. Here, $\lambda/D = 3.9$ and $a = 8.4$ mm.

The damping constant determines the rate of decay of long period oscillations due to the mooring. The larger the damping constant, the less time it takes for the floe to return to a steady periodic response. A steady periodic response occurs when a floe oscillates at a constant amplitude and frequency. The bottom panel of Figure 6.2.2 shows an example of the effect of the damping constant on floe motions. Wave conditions in this test are the same as the top panel. Two values of C are considered, while K is kept at 0.32. When $C = 0.8$ (red), oscillations reach a steady periodic equilibrium after approximately 17 s. When $C = 0.5$ (black), long period oscillations continue beyond 40 s.

Both mooring coefficients were tuned using a total of six tests. Across these six tests, the parameters $K = 0.32$ and $C = 0.5$ gave the best fits to the experimental data.

6.2.4 Hydrodynamic coefficients

In § 3.6, we compared the surge RAOs from the single-floe experiments with predictions using the slope-sliding model and found that an added mass coefficient of $c_m = 0.1$ gave the best model-data agreement in the long-wavelength regime. Since the surge RAOs of Floes F and R are comparable with Floe B (see § 5.3.3), $c_m = 0.1$ is adopted for all two-floe simulations. As for the drag coefficient c_d, surge was shown to be insensitive to changes in c_d, and drift velocities were slightly sensitive to c_d.

Figure 6.2.3 shows an example of the effect of c_d on the horizontal motions of a two-floe system when surge is dominant. Wave conditions for this example are the same as Figure 6.2.2 ($\lambda/D = 3.8$ and $a = 8.4$). Experimentally measured displacements from the corresponding test are shown for reference. In this test, we are considering motions in the long-wavelength regime when no collisions occur. The displacements of Floes F and R are therefore almost identical, hence only the x-displacement of the front floe is shown.

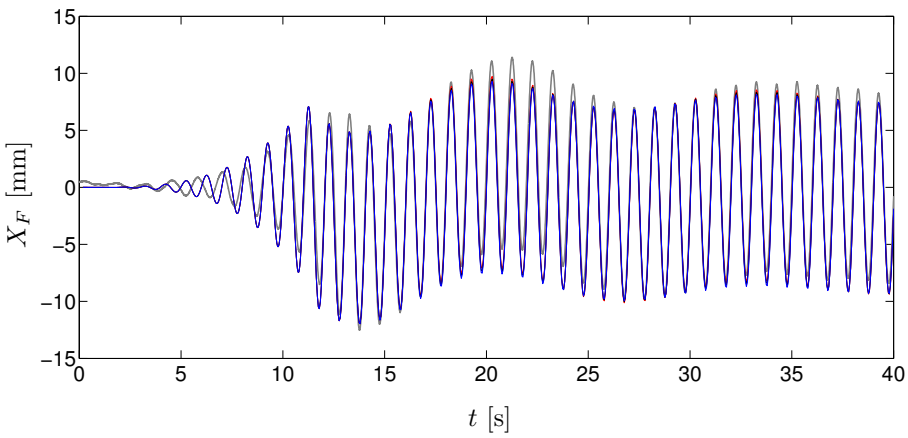

Figure 6.2.3: Effect of the drag coefficient c_d on floe displacements when surge is dominant. Three drag coefficients are considered: $c_d = 0$ (−), 0.05 (−) and 0.1 (−). In all cases, $c_m = 0.1$. Results are indistinguishable. Experimental measurements (−) are shown for comparison. Here, $\lambda/D = 3.9$ and $a = 8.4$ mm.

Solutions are generated using three drag coefficients ranging from $c_d = 0$ to 0.1. These values are chosen based on the findings of Madsen and Bruno (1987), who performed experiments to measure the mean drag coefficients of ice floes. Figure 6.2.3 shows that the drag coefficient has a minimal effect on the floe's motions. The predicted x-displacements, using the three values of c_d, are indistinguishable

from each other. This result agrees with our findings in § 3.4, which demonstrate that drag has no significant effect on surge.

When collisions occur, the effect of c_d becomes more significant. This is mainly due to the drift experienced when floes rebound after a collision and return back towards each other under the action of the mooring lines. Figure 6.2.4 shows an example of the effect of drag when collisions occur. The incident wave frequency is similar to Figure 6.2.3 however the wave amplitude is increased to $a = 16.5\,\text{mm}$. Collisions are simulated using two drag coefficients: the first is $c_d = 0.005$, and the second is an order of magnitude larger at $c_d = 0.05$. Experimental results are overlaid for comparison.

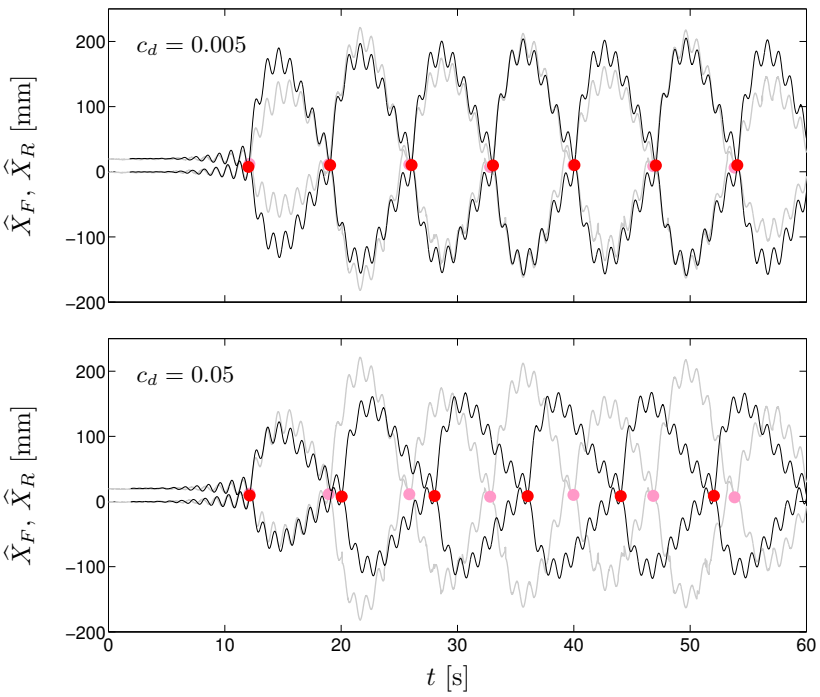

Figure 6.2.4: Effect of drag coefficient c_d on floe displacements when collisions occur. Two drag coefficients are considered: $c_d = 0.005$ and 0.05 (top and bottom panels, respectively). In both simulations $c_m = 0.1$ and $\epsilon = 1$. Collisions events are indicated (●). Shaded curves and bullets represent experimental data. Here, $\lambda/D = 3.9$ and $a = 16.5\,\text{mm}$.

The top panel of Figure 6.2.4 demonstrates good agreement between the experiments and model predictions when $c_d = 0.005$. The model predicts collision frequencies to be 0.143 Hz, which is within 1% of the experimental results. The average maximum (post-collision) separation predicted by the model is also within 1% of the experimental results. Post-collision separations can be tuned by adjusting the coefficient

of restitution ϵ. Decreasing the restitution will result in smaller post-collision velocities and smaller maximum separations. A coefficient of restitution of $\epsilon = 1$ is used to obtain the simulations in Figure 6.2.4. This value gives good agreement in terms of post-collision separations.

In the non-rafting experiments, we attempted to quantify the coefficient of restitution by comparing the pre- and post-collision velocities (recall, velocities are calculated as the slope of a linear regression of time-series motions in the x-direction, over 10 time steps prior to a collision), however we observed large variances in results. The coefficient of restitution had a median value of $\epsilon = 0.91$ and a standard deviation of 0.54. The large variances were likely caused by non-planar motions such as pitch, which complicates the calculation of the restitution coefficient. Since good agreement was obtained when $\epsilon = 1$, as shown previously and in several other tests, we applied this coefficient to all simulations. We expect that when two relatively non-deformable bodies collide, minimal kinetic energy is lost after a collision.

When drag is increased to $c_d = 0.05$ (in the bottom panel of Figure 6.2.4), the increased resistive forces cause the average maximum separations to decrease. A larger drag coefficient also translates to a decrease in drift velocity as the fluid resistance increases. Previously, Grotmaack and Meylan (2006) showed that a larger drag coefficient increases the drift velocity of a solitary free-floating body. However, in this particular setup, when floes experience a restoring force due to the mooring system, the post-collision drift velocity decreases as drag is increased. The smaller drift velocity also increases the time taken for floes to rebound and drift back towards each other. This effect is revealed in the decrease of mean collision frequencies to 0.125 Hz.

Drag coefficients were tuned for every experimental test condition. Figure 6.2.5 shows the empirically determined drag coefficients from tests which gave good model-data agreement. Results from tests which had no significant sensitivity to changes in c_d (i.e. test with no collisions and dominant surge), and tests with poor model-data agreement (e.g. short-wavelength tests), are excluded from the figure.

Results show that the drag coefficient varies with incident wavelength and wave amplitude. Drag coefficients range from a minimum of $c_d = 0$ when $\lambda/D = 12.3$

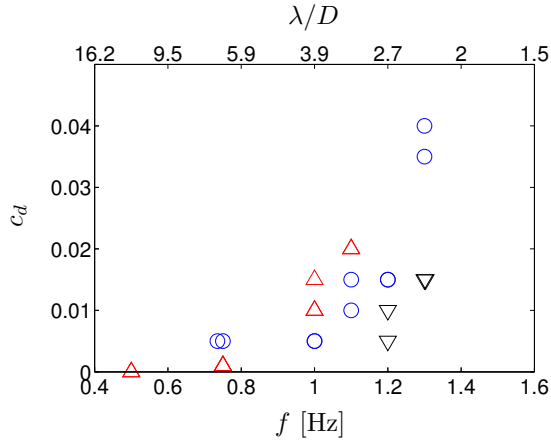

Figure 6.2.5: Empirically determined drag coefficients as functions of incident wave frequency (and corresponding nondimensional wavelength) and wave amplitude. Symbols denote target wave amplitudes: $a = 10\,\text{mm}$ (▽), $20\,\text{mm}$ (○), $40\,\text{mm}$ (△).

and $a = 40\,\text{mm}$, to a maximum $c_d = 0.04$ when $\lambda/D = 2.3$ and $a = 20\,\text{mm}$. In general, drag increases with decreasing wavelength, and increases with increasing wave amplitude. In other words, drag increases with increasing wave steepness. A possible explanation for this is the increase in form drag as floes increasingly dip in and out of the water surface in shorter and steeper waves. Recall that in long wavelengths, floes essentially move like water particles on the water surface (see § 2.3.1), therefore their bodies are static in relation to the wave. In shorter wavelengths, floes heave and pitch less with respect to the wave, therefore their relative motions are large in comparison to wave motions. As a result, their submerged profile in the yz-plane increases. Since their body profile increases, we can expect their form drag to increase.

6.3 Comparison with two-floe experiments

The accuracy of the collision model is determined using three metrics: (i) average post-collision separation, (ii) mean collision frequency, and (iii) mean collision velocity. In § 6.2.4, examples were given to demonstrate how the post-collision separations are used to tune the drag coefficient. In this section, we will focus on quantifying accuracy based on metrics (ii) and (iii).

In the collision model, mean collision frequencies $\overline{f}_c$ are calculated as per the method in § 5.3.2. Recall, $\overline{f}_c$ was evaluated as the reciprocal of the average period between

successive collisions. Mean collision velocities, on the other hand, are calculated slightly differently to § 5.3.2. Here, instead of deriving the collision velocity from the x-displacements over the last 10 time-steps before a collision, we simply use the slope of the displacement time-series immediately before a collision event as per step 3a of the collision algorithm. The former method was employed to account for noise in the experimental signals.

The three metrics are used to replicate the results of the two-floe non-rafting experiments. Figure 6.3.1 shows a comparison of the experimental and theoretical mean collision frequencies and velocities. Results are presented as functions of incident wave frequency and corresponding wavelength, as with Figure 5.3.4, and are grouped according to target wave amplitudes. Symbols denote experimental data while bullets denote model predictions. The drag coefficients in Figure 6.2.5 are used to generate these solutions.

Note that all simulated results in Figure 6.3.1 are also obtained using a restitution coefficient $\epsilon = 1$. In § 6.2.4, we saw how the model simulated collisions accurately using this coefficient. We expected that the coefficient of restitution is independent of wave conditions, therefore a consistent value of $\epsilon = 1$ is used in all simulations.

The comparison in Figure 6.3.1 incorporates the data from Figure 5.3.1, which indicates the occurrence of collisions over the range of incident wavelengths and wave amplitudes considered. Comparisons show that the collision model predicts the occurrence of collisions accurately in incident wavelengths larger than $\lambda/D = 2.7$ ($f = 1.2\,\mathrm{Hz}$). In this wavelength regime, both model and experiments agree on when collisions occur in all but two identical cases (repeated tests). For both cases, $\lambda/D = 3.2$ ($f = 1.1\,\mathrm{Hz}$) and $a = 10\,\mathrm{mm}$. The collision model predicted that no collisions occur, however in the experiments a single weak collision occurs.

The model also predicts the mean collision frequencies and velocities fairly accurately in mid- to long-wavelength regime. When collisions occur, the average difference in collision frequencies is 7.4%. The average difference is calculated using the differences between mean values of $\overline{f}_c$ from the experiments and the model at each wavelength and wave amplitude. Differences range from 18.7% when $\lambda/D = 12.3$ ($f = 0.5\,\mathrm{Hz}$) and $a = 40\,\mathrm{mm}$, to less than 1% when $\lambda/D = 3.9$ ($f = 1\,\mathrm{Hz}$) and

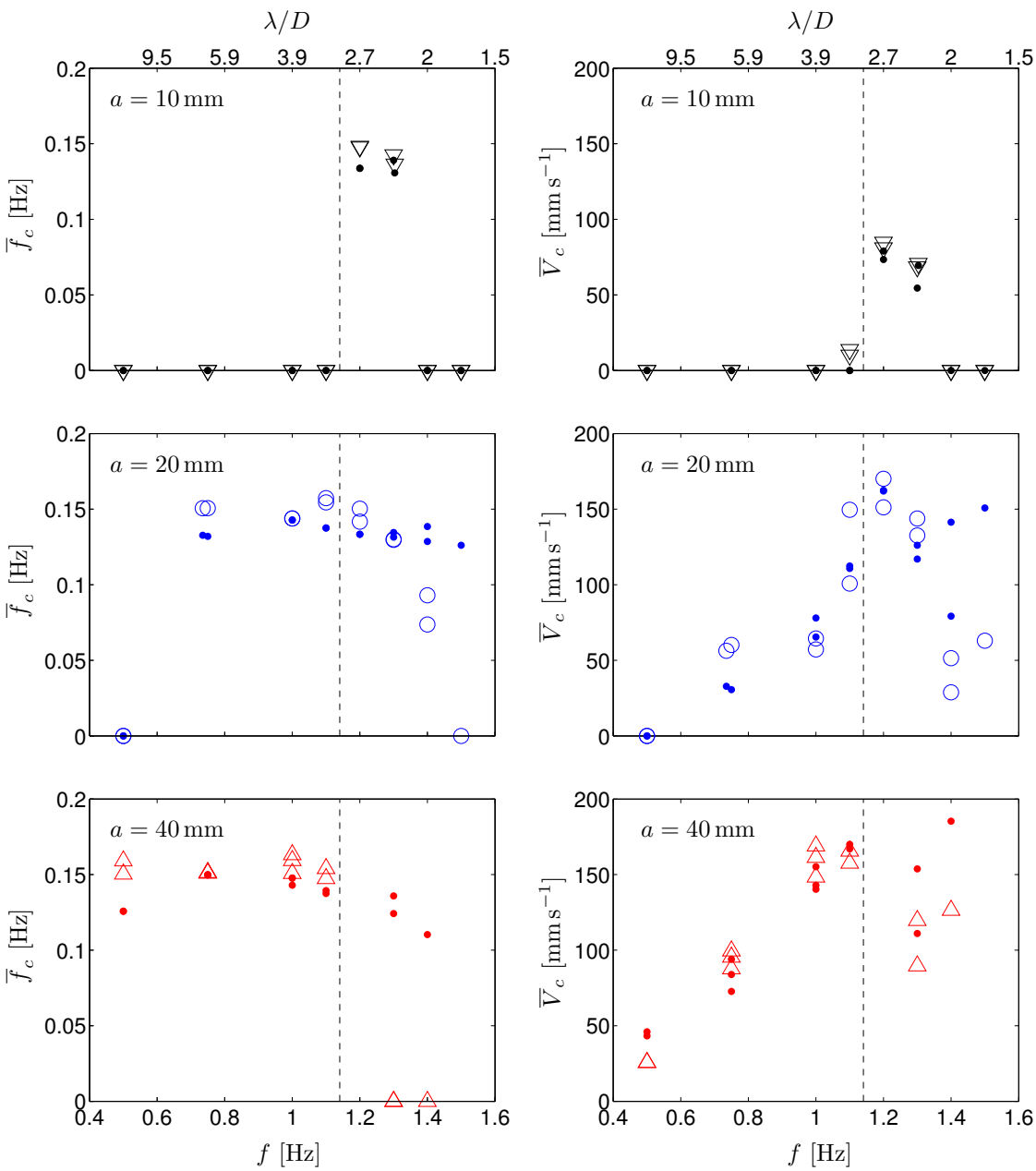

Figure 6.3.1: As with Figure 5.3.4 but with model predictions (bullets) included.

$a = 20\,\mathrm{mm}$.

When collisions occur, theoretical collision velocities are, on average, within 15.9% of the experimental results. The largest error is 73.7% when $\lambda/D = 12.3$ and $a = 40\,\mathrm{mm}$. It should be noted that the measured collision velocity for this test is small ($\overline{V}_c = 25.7\,\mathrm{mm\,s^{-1}}$) compared to other tests, therefore the percentage error would be large. The absolute difference, however, is $19\,\mathrm{mm\,s^{-1}}$, which is comparable to the differences in other tests.

Theoretical predictions are largely inaccurate in wavelengths less than $\lambda/D = 2$ ($f \geq 1.4\,\mathrm{Hz}$) when $a = 10$ and $20\,\mathrm{mm}$, and in wavelengths less than $\lambda/D = 2.3$ ($f \geq 1.3\,\mathrm{Hz}$) when $a = 40\,\mathrm{mm}$. In this regime, the model is invalid due to the assumptions and limitations of slope-sliding theory. Note that for $a = 10\,\mathrm{mm}$, both model and data agree that no collisions occur when $f \geq 1.4\,\mathrm{Hz}$, however simulated floe displacements in those tests were very different to the measured displacements. The collision model was, in general, unable to simulate the large drift behaviour in the short-wavelength regime. Figure 6.3.2 shows an example of this when $\lambda/D = 1.7$ and $a = 33\,\mathrm{mm}$. The model does not simulate floe displacements accurately even when a large drag coefficient of $c_d = 1$ is applied.

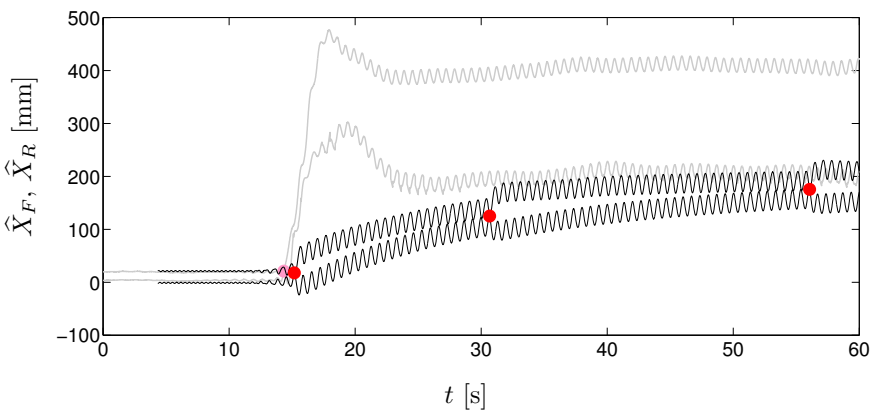

Figure 6.3.2: Example of the collision model not being able to simulate floe behaviour in short wavelengths. In this test, $f = 1.5\,\mathrm{Hz}$ ($\lambda/D = 1.7$) and $a = 33\,\mathrm{mm}$. Theoretical predictions (−) of x-displacements versus experimental measurements (−). A drag coefficient of $c_d = 1$ is used in this simulation.

6.4 Summary

In this chapter a time-stepping collision algorithm is developed to simulate the wave-induced interactions of a two-floe system. The model replicates the conditions of the two-floe non-rafting experiments described in Chapter 5. In the model, floes are visualised as one-dimensional planes, and their collisions are determined by considering each floe's horizontal and rotational motions. Motions are simulated by applying slope-sliding theory.

The slope-sliding equation of motion accounts for transient wave amplitudes and coefficients for spring and damping (due to the mooring system), and added mass and drag (due to hydrodynamic forces). A coefficient of restitution is also included in the model to account for inelastic collisions. A parameter study was conducted to investigate the effects of these coefficients on the horizontal motions predicted by the model. Spring and damping coefficients determined the amplitude of oscillations and the decay rate of transient oscillations, respectively. The effect of the drag coefficient was shown to be insignificant when surge was dominant. The drag coefficient, however, became more important in the regimes where collisions occurred. Changes to the drag coefficient affected the maximum post-collision floe separation, and the mean collision frequencies and velocities.

Mooring, hydrodynamic and restitution coefficients were tuned empirically using data from the two-floe experiments. A restitution coefficient $\epsilon = 1$ gave good model-data agreement in most wave conditions. An added mass coefficient $c_m = 0.1$ was used in all simulations, in consideration of the findings of Chapter 3. Drag coefficients were shown to increase with wave steepness. We hypothesised that this was related to the increase in form drag.

Theoretical predictions of mean collision frequencies and velocities were compared with data obtained from the two-floe experiments. Results showed that the model can be used to accurately predict collision behaviours in incident wavelengths greater than 2.7 times the floe diameter. In shorter wavelengths, predictions were unreliable and could not simulate the large drift velocities in that regime.

Chapter 7

Extension to rafting

In this chapter, we extend our investigation of floe collisions by considering the wave-induced rafting between two floes. Rafting is a subset of the collision process. As mentioned in Chapter 1, rafting occurs when two floes collide out of plane and overlap each other. In the first part of this chapter, we will discuss how rafting is simulated using wave basin experiments. Rafting is then modelled theoretically by extending the two-floe collision model of Chapter 6.

7.1 Two-floe rafting experiments

7.1.1 Experimental method

The third round of wave basin experiments was conducted at the State Key Laboratory of Coastal and Offshore Engineering (SLCOE) at the Dalian University of Technology (DUT), China. The objectives of these experiments differ slightly to the non-rafting experiments. Here the focus is on determining which collision regime leads to rafting. More specifically, the goal is to identify (i) the wave conditions necessary for rafting, (ii) the motions responsible for causing rafting, and (iii) investigate how the rafting process develops over time. Previously, rafting was suppressed

through the use of edge barriers. In these experiments barriers are removed to allow for rafting.

Figures 7.1.1 and 7.1.2 show an image and a schematic diagram of the DUT wave basin. The basin measures 40 m by 24 m and was filled with fresh water to a depth of $h = 0.5$ m. Monochromatic waves are produced by the wave maker, which is located at the forward end of the basin. A sloping beach at the rear end dissipates reflected waves in the basin.

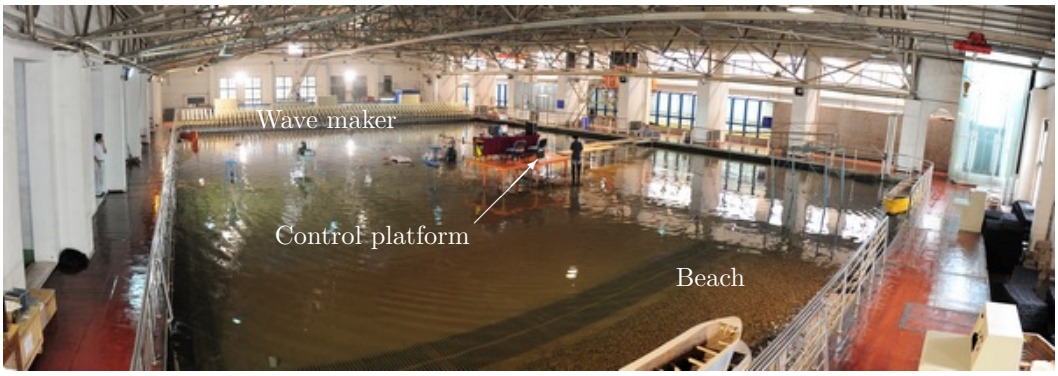

Figure 7.1.1: Image of the DUT wave basin facility (`http://slcoe.dlut.edu.cn`).

Figure 7.1.2 also shows a schematic of the experiment setup. Two identical PVC disks (floes) were tested in the experiments. The dimensions of both floes are unchanged from the previous experiments. Recall, the floe diameter $D = 400$ mm and its thickness $H = 15$ mm. Their masses, however, are slightly smaller, at $m = 0.95$ kg. Hence, their densities are $\rho_b \approx 504\,\mathrm{kg\,m^{-3}}$. (Previously $\rho_b \approx 636\,\mathrm{kg\,m^{-3}}$).

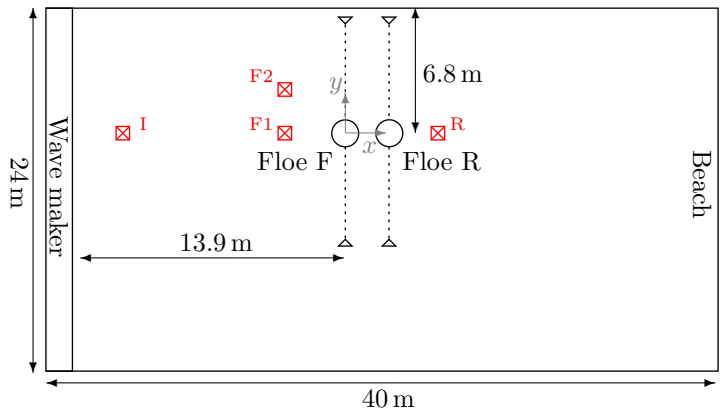

Figure 7.1.2: Schematic plan view of the DUT wave basin during the two-floe rafting experiments. Symbols (⊠) denote approximate locations of wave probes.

Floes were arranged in a similar configuration to the non-rafting experiments. Here, the front and rear floes are again designated as Floe F and Floe R, respectively.

Floe F was positioned approximately 13.9 m down the wave basin to allow sufficient distance for incident waves to develop fully. Both floes were positioned closer (approximately 6.8 m) to the right edge of the basin to allow easy access to the floes and measuring systems via a raised control platform.

Figure 7.1.2 also shows the Cartesian coordinate system (x, y, z) in the wave basin. The origin of the coordinate system is located at the intersection between the radial axis of symmetry of Floe F and the equilibrium water surface. The direction of each axis is consistent with all previous experiments.

Tests were conducted using three target incident wave amplitudes $a_{\text{target}} = 20$, 30 and 40 mm, and up to seven wave frequencies between $f = 0.67$ to 1.82 Hz. Compared to the non-rafting experiments, a narrower range of wave frequencies were tested to achieve greater resolution of results within the transition regimes of collisions. Preliminary tests were conducted to determine the regimes where rafting, non-rafting collisions and no collisions occurred. Wave frequencies were also chosen such that the intervals are evenly spaced with respect to incident wavelength. The range of target wave amplitudes differs slightly from the non-rafting experiments due to the performance of the wave maker. (Previously $a_{\text{target}} = 10$, 20 and 40 mm.) When $a_{\text{target}} = 10$ mm, the wave maker produced waves of irregular amplitudes. A minimum amplitude $a_{\text{target}} = 20$ mm was therefore chosen.

Table 7.1.1 lists the target wave amplitudes, wave frequencies and corresponding wavelengths tested in the rafting experiments. The two largest wave frequencies for $a = 40$ mm were not tested, since waves conditions were clearly within the breaking limit of $ka > 0.21$. Recall, this limit was determined in the single-floe experiments (see § 2.2.5). Tests with wave steepnesses above 0.21 are highlighted in red. As with the non-rafting experiments, these tests were still performed because they form a large part of the rafting regime. The overall range of wave steepnesses tested was between $ka = 0.045$ to 0.4.

The effect of separations between floes was also investigated by considering two initial separations, s_0. Test conditions in Table 7.1.1 were repeated for $s_0 = 30$ mm and 60 mm. In total, 28 tests were conducted for each initial separation. This is inclusive of 9 repeated tests at every alternate wavelength interval wherever possible.

f [Hz]	0.67	0.77	0.87	1	1.25	1.67	1.82
λ [m]	2.85	2.31	1.92	1.51	1	0.56	0.47
$a = 20\,\mathrm{mm}$	•	⊙	•	⊙	•	⊙	•
$a = 30\,\mathrm{mm}$	•	⊙	•	⊙	•	⊙	•
$a = 40\,\mathrm{mm}$	•	⊙	•	⊙	⊙		

Table 7.1.1: Summary of test matrix for two-floe rafting experiments. Encircled bullets denote repeated tests. Red bullets denote tests with target wave steepnesses, ka, greater than 0.21.

Wave conditions for repeated tests are indicated in Table 7.1.1.

Figure 7.1.3 shows an image of the initial setup when $s_0 = 30\,\mathrm{mm}$. A mooring system, which consists of a pair of thin rubber cords on either side of each floe, was used to tether the floes transversely. The ends of the cords were secured to a set of tripod stands, which were positioned 5.1 m apart. All tethers were engaged (i.e. stretched out) at the start of each test, thereby ensuring that the spring and damping forces act on the floes throughout the test. Compared to the non-rafting experiments, the mooring lines used here were slightly more elastic, and hence less restrictive on the motions of the floes.

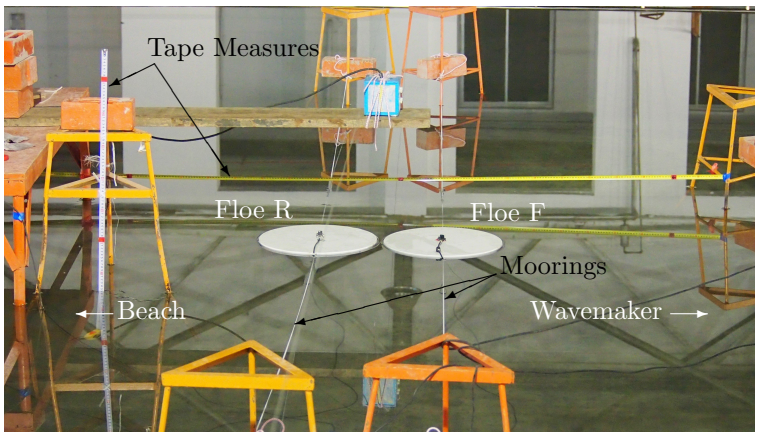

Figure 7.1.3: Photo of rafting experiment setup, showing the initial positions of Floes F and R, mooring lines and tape measures for video measurements.

A magnetic motion capture system was used to record the six-degree rigid-body motions of both floes in time. Song et al. (2014) and Huang et al. (2016b) previously utilised this system to measure the motions of a submerged tunnel-pontoon system. Figure 7.1.4 shows an image of the system during our experiments. The motion capture system utilises of a pair of electromagnetic sensors and a transmitter unit,

which generates a magnetic field. The transmitter is positioned directly above the floes via a wooden platform. Sensors are attached to the top surfaces of the floes and aligned with their radial centres. The transmitter and sensors are connected to a electronic control unit using neutrally buoyant cables. It is assumed that the cables do not significantly affect floe motions. The control unit reads the strength of the magnetic field at each sensor and calculates the locations of both floes at a rate of 50 Hz. For each test, at least 40 s of data was collected.

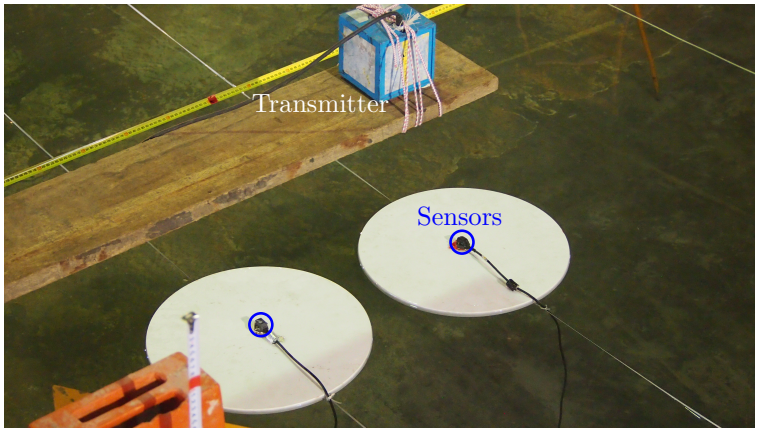

Figure 7.1.4: Image of the magnetic motion tracking system.

A pair of tape measures were used to calibrate the motion capture system at the start and end of the experimental campaign. Figure 7.1.3 shows how the tape measures were set up. One tape measure was positioned vertically behind Floe R and another was placed horizontally above both floes. The tape measures also allowed visual confirmation of all other length scales (e.g. wave amplitudes) via video recordings. All tests were recorded on video from the viewpoint of Figure 7.1.3.

Four wave probes were installed around the wave basin to record the wave frequencies and amplitudes in the vicinity of the floes and the wave maker. Wave probes are denoted as Probes I, F1, F2 and R. Figure 7.1.2 shows their approximate locations. Probe I measured the incident wavefield 6.8 m from the wave maker. Probes F1 and R measured the wavefields 1.2 m in front of Floe F and 2 m behind Floe R, respectively. Probe F2, which was positioned approximately 1 m to the right and transversely inline with Probe F1, was installed as a redundancy.

After completing the experiments, we analysed the data from the four probes and found a series of erroneous results with regards to measured wave amplitudes. (Fig-

ure 7.1.5 shows the measured wave amplitudes from all four wave probes.) Firstly, wave amplitudes measured at Probe I are, on average, largely different to the other probes. This however was expected since incident waves near the wave maker were not yet fully developed. Secondly, wave amplitudes measured at Probes F1 and F2 are largely inconsistent, with errors ranging from -37% to 34%. We expected that wave amplitudes at Probes F1 and F2 would be nearly identical since they were both equidistant from the wave maker. Thirdly, wave amplitudes measured at Probes F1 and F2 are inconsistent with Probe R in the long-wavelength regime. Based on the findings of Bennetts and Williams (2015), full transmission was expected in wavelengths longer than $\lambda/D = 4$, approximately. Figure 7.1.5 shows that in the smallest three wave frequencies ($f = 0.67$, 0.77 and $0.87\,\mathrm{Hz}$), measured wave amplitudes at Probe F1 are consistently smaller than at Probe R, with the average error at -10%. Probe F2 generally measured larger amplitudes than Probe R, with the average error at 18%.

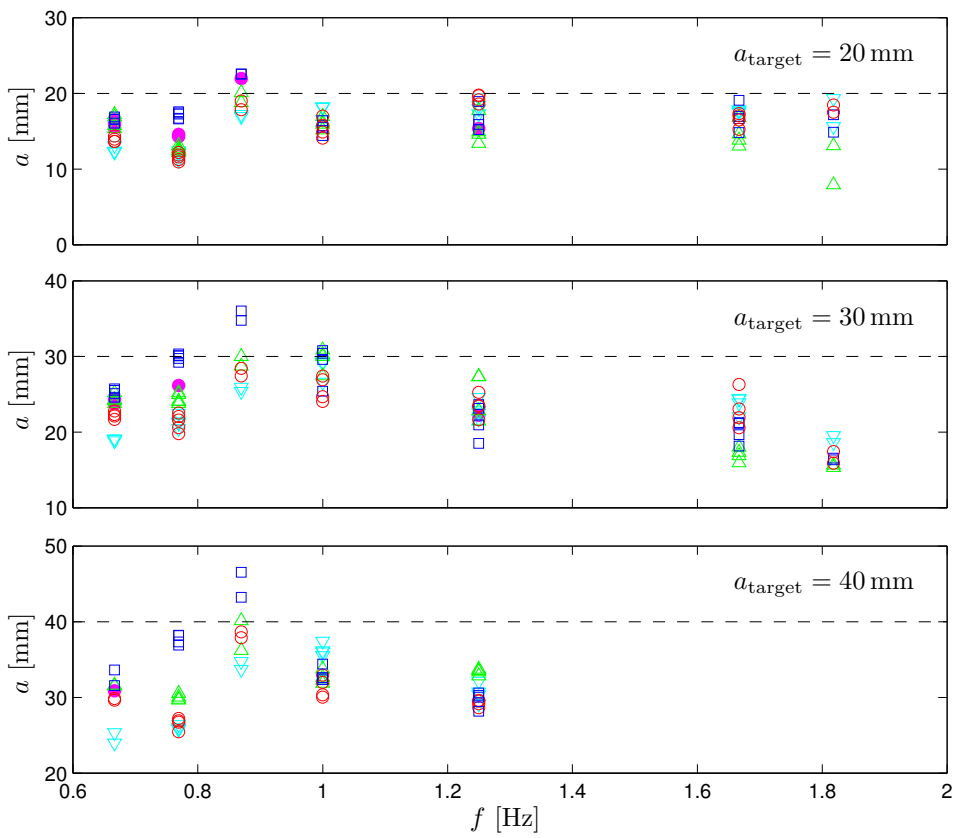

Figure 7.1.5: Measured wave amplitudes when target amplitudes $a_{\mathrm{target}} = 20\,\mathrm{mm}$, $30\,\mathrm{mm}$ and $40\,\mathrm{mm}$ (top, middle and bottom panels, respectively). Symbols denote measured amplitudes at Probes I (▽), F1 (○), F2 (□), R (△), and from video recordings at the vertical tape measure (●).

Video measurements were used to verify wave probe data in wave frequencies between $f = 0.67$ to $1.25\,\text{Hz}$. Wave amplitudes were extracted from video recordings using the open-source program, Tracker (`http://physlets.org/tracker/`). Amplitudes were measured using the waterline at the vertical tape measure (positioned behind Floe R). Data could only be extracted from several tests due to the quality of video recordings (the waterline could not be acquired when the video was out of focus). These data points are overlaid in Figure 7.1.5.

Video measurements of wave amplitudes confirm that Probe R is accurate. Because of the discrepancy between Probes F1, F2 and Probe R, we deduced that Probes F1 and F2 were both faulty. Data from these probes are therefore disregarded. Only Probe R was useful in estimating the incident wave amplitudes, however this applies only in regimes where full transmission occurs. In regimes where wave scattering exists, measured waves amplitudes are expected to be different in front and behind the floes. For this reason, all wave probe measurements are disregarded, and all subsequent incident wave amplitudes are reported in terms of target quantities.

7.1.2 Results

The following link contains the complete experimental dataset, from which results in this section are derived: `https://github.com/AdelaideUniversityMathSciences/TwoFloeCollisionModels/tree/master/TwoFloeExperiments/RaftingExperiments`.

Collision and rafting regimes

Figure 7.1.6 shows the regimes of rafting and non-rafting collisions over the range of wave amplitudes and wavelengths tested. Results in the top and bottom panels are for initial separations $s_0 = 30\,\text{mm}$ and $60\,\text{mm}$, respectively. Red triangles indicate tests with at least one rafting event. Blue circles indicate tests where only non-rafting collisions occurred. Black crosses indicate tests without collisions. Smaller and concentric symbols denote repeated tests.

Rafting regimes are separated into three groups, which are indicated in Figure 7.1.6 using different coloured regions. In the green regions, which are labelled “Rafting

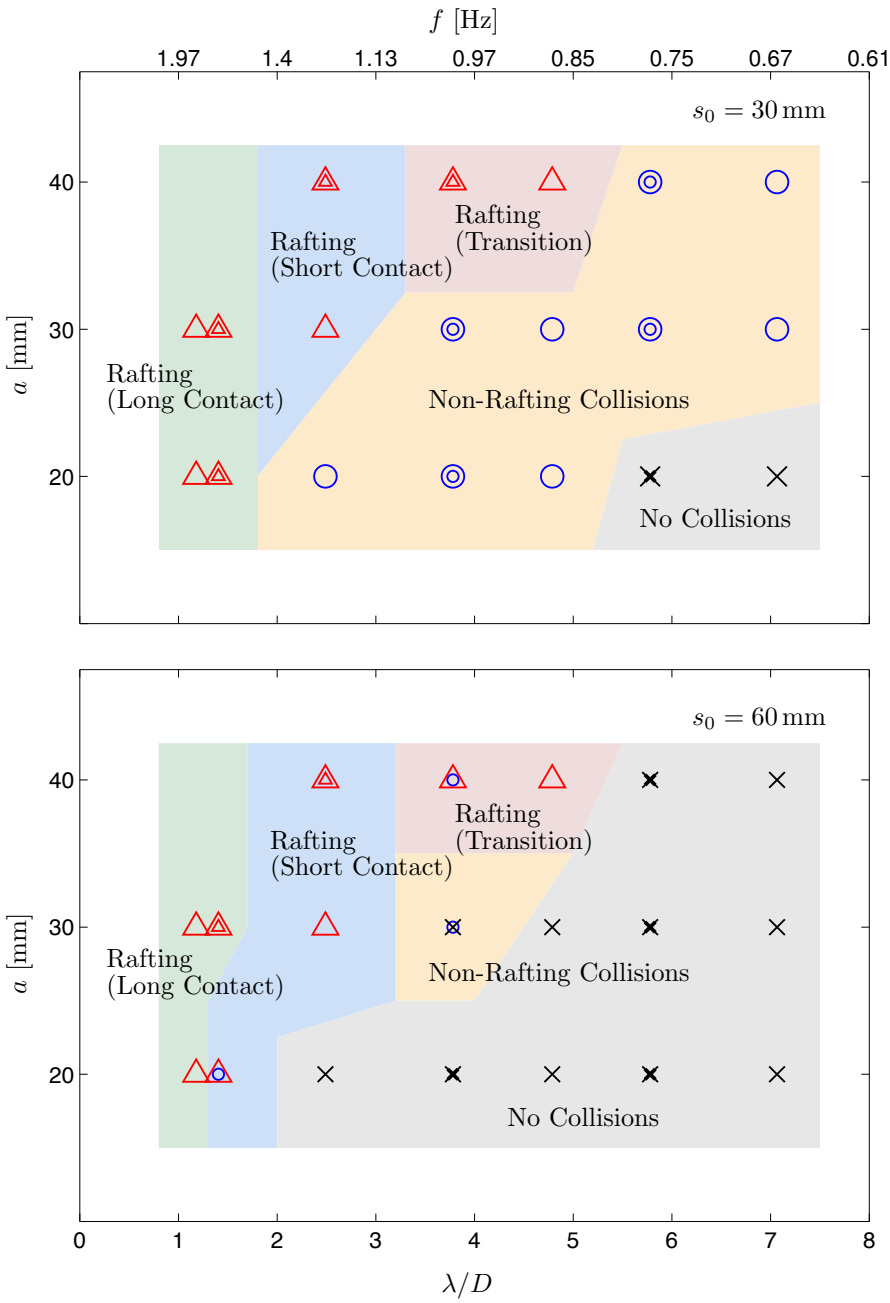

Figure 7.1.6: Collision and rafting regimes as a function of target incident wave amplitude and nondimensional wavelength, for tests with initial separation $s_0 = 30\,\mathrm{mm}$ (top panel) and $s_0 = 60\,\mathrm{mm}$ (bottom). Symbols indicate tests where rafting (△), non-rafting collisions (○) and no collisions (×) occurred. Smaller symbols denote repeated tests.

(Long Contact)", floes initially raft once or twice, then remain rafted for the rest of the test. Figure 7.1.7 shows an example of the motions in the x-axis when this rafting behaviour occurs. The long-contact behaviour is related to the wave characteristics as well as floe surface conditions. For example the characteristics and orientation of the floe surface will affect the friction between floes. In these experiments, the friction between the two floes was relatively small given their smooth surfaces. However the effects of water surface tension (due to the thin film of water between the horizontal surfaces of each floe) were visible in certain tests, and resulted in the floes appearing to 'adhere' together when their upper and lower surfaces were flushed against each other. This effect was more noticeable when the horizontal overlap increased (note that this effect was less obvious in the test shown in Figure 7.1.7, which had a mean horizontal overlap of 92 mm). The angle of contact also determined if the floes were likely to raft for long periods. In this regime, the pitch angles of both floes were generally equivalent (see right panel of Figure 7.1.7). Floes motions in this regime are also characterised by large drift while they are rafted together. Similar behaviours also occurred in the non-rafting experiments (see § 5.3.1). Floes eventually reach a mean steady-state displacement when drift and mooring forces are in equilibrium. In this example, floes reach a steady-state displacement approximately 10 s after the first contact.

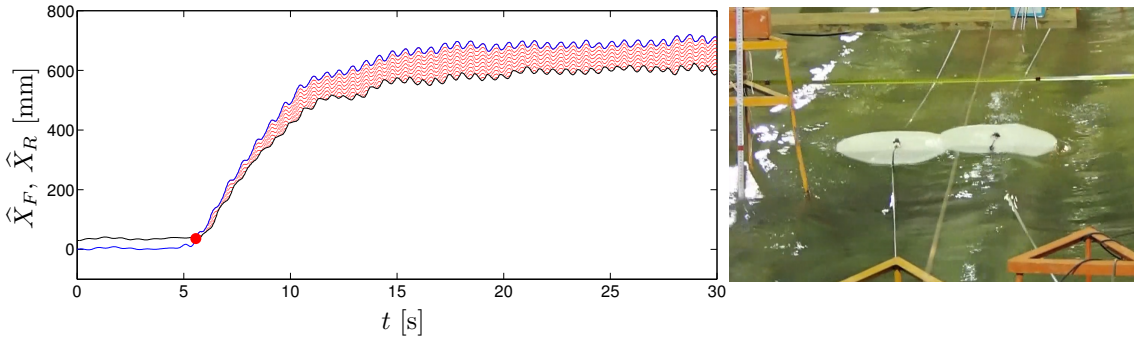

Figure 7.1.7: Example of long contact rafting. Left panel: x-displacements of Floe F (−) and R (−) when $f = 1.67$ Hz ($\lambda/D = 1.4$) and $a = 30$ mm. Red bullet indicates first instance of overlap. Red shaded region denotes periods where floes are rafted. Right panel: Image of floes in corresponding test.

In Figure 7.1.6, the blue regions, labelled "Rafting (Short Contact)", are by definition characterised by short-contact rafting behaviours. Figure 7.1.8 shows an example of the horizontal motions in this regime. Floes overlap for short durations but do not stay continuously rafted. This is because the contact angles of floes are

larger (see right panel of Figure 7.1.8). This is also likely due to the fact that mean drift forces, which are proportional to the amplitude of reflected waves (Faltinsen, 1990, Chapter 5), are smaller in long waves. Restoring forces from the mooring system therefore become more influential than drift forces and cause the floes to separate after rafting. The steady-state behaviour in this regime resembles the short wavelength, intermediate wave amplitude behaviour in the non-rafting experiments (see example (c) in Figure 5.3.2), in which floes approach a mean equilibrium separation.

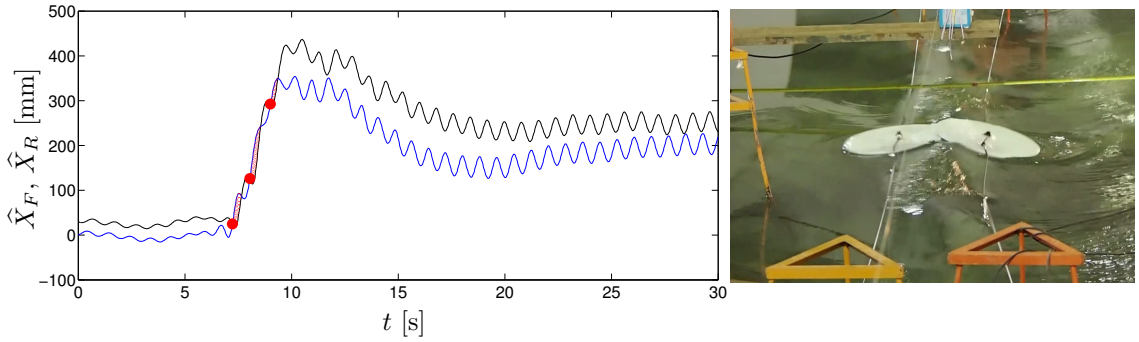

Figure 7.1.8: Example of short contact rafting. As with Figure 7.1.7 but for $f = 1.25\,\text{Hz}$ ($\lambda/D = 2.5$) and $a = 40\,\text{mm}$.

Collision behaviours in the red regions, labelled "Rafting (Transition)", contain both short-contact rafting and non-rafting events, and are characterised by repeated collisions at near-regular intervals throughout the test. This region is therefore a transient regime between the rafting and non-rafting collision regimes.

For initial separations $s_0 = 30\,\text{mm}$, the long-contact rafting regime occurs between $\lambda/D \approx 1.2$ to 1.4 and from $a \approx 20$ to $30\,\text{mm}$. For larger wave amplitudes in excess of $30\,\text{mm}$ (not tested), it is expected that the same prolonged rafting behaviour will occur since drift forces increase, and thus become more dominant than mooring forces. The short-contact rafting regime occurs in wavelengths of $\lambda/D \approx 2.5$, and in medium to large wave amplitudes. The transient regime between rafting and non-rafting collisions occurs when $a \approx 40\,\text{mm}$ and within the ranges of $\lambda/D \approx 3.8$ to 4.8. The general trend is for rafting to occur in short wavelengths and steeper waves. Non-rafting collisions occur in the remaining mid- to long-wavelength regimes, and are more prevalent in medium to low amplitude waves. No collisions occur when $a \approx 20\,\text{mm}$ and $\lambda/D > 5.8$, approximately.

When the initial separation increases to 60 mm, the no-contact regime expands to intermediate wavelengths and larger amplitude waves. The occurrences of collisions decrease, as expected, because of the larger separations between floes. Rafting regimes however remain relatively unchanged, apart from short-contact rafting occurring when $\lambda/D \approx 1.4$. Non-rafting collisions only occur when $\lambda/D \approx 3.8$ and $a = 30$ mm.

Note that for an initial separation $s_0 = 30$ mm, all repeated tests produced identical results, in terms of the occurrence of collisions and rafting events. However, when $s_0 = 60$ mm, results were different in 3 out of 9 repeated tests. Differences are attributed to sensitivity to slight changes in wave conditions. For example, when $a = 30$ mm and $f = 1$ Hz ($\lambda/D = 3.8$), non-rafting collisions occurred in the first test and no collisions occurred in the repeated test. Wave amplitudes were observed to be slightly smaller in the repeated test, consequently surge amplitudes were reduced. No collisions occurred since surge amplitudes were less than the initial separation. When $a = 20$ mm and $f = 1$ Hz, collision behaviours differed only by a single event. (Recall, tests are considered to be in the rafting regime if at least one rafting event occurs.) In the first test, 4 non-rafting collision events occurred over a 40 s interval. In the repeated test, 4 out of 5 collision events were non-rafting collisions. Only a single short-contact small-overlap rafting event occurred. A similar reason explains the difference in collision behaviours when $a = 20$ mm and $f = 1.67$ Hz ($\lambda/D = 1.4$). A single short-contact rafting event occurred in the first test, while a single non-rafting collision event occurred in the repeated test. Since accurate measurements of wave amplitudes are not available, the results in Figure 7.1.6 therefore only provide a general estimate of the rafting and collision regimes.

Video recordings of examples in the various regimes of rafting and collisions can be downloaded via the link: `https://github.com/AdelaideUniversityMathSciences/TwoFloeCollisionModels/tree/master/TwoFloeExperiments/RaftingExperiments/Videos`.

Relative surge

In the non-rafting experiments, the relative surge, ΔSurge, of Floes F and R was quantified (see § 5.3.3) to determine the effect of surge and drift on non-rafting collisions. Recall, in the long-wavelength regime, we found that surge was responsible for causing collisions. In the short-wavelength regime, either surge or drift could cause collisions. When collisions were caused by drift, the relative surge was less than the initial separation. Here, the same analysis is performed to validate those findings. Relative surge is calculated using the same method described in § 5.3.3. Recall, $\Delta\text{Surge} = \left|\overline{a}_s(\mathrm{e}^{\mathrm{i}\varphi_F} - \mathrm{e}^{\mathrm{i}\varphi_R})\right|$, where $\overline{a}_s$ is the mean steady-state surge amplitude for both floes (calculated using the DFT method), and φ_F and φ_R are the phases of Floes F and R just before a collision/rafting event.

Figure 7.1.9 shows the normalised relative surge, $\Delta\text{Surge}/s_0$, as a function of nondimensional wavelength. All instances of non-contact between floes correspond with values of $\Delta\text{Surge}/s_0 < 1$. This result was also obtained in the non-rafting experiments.

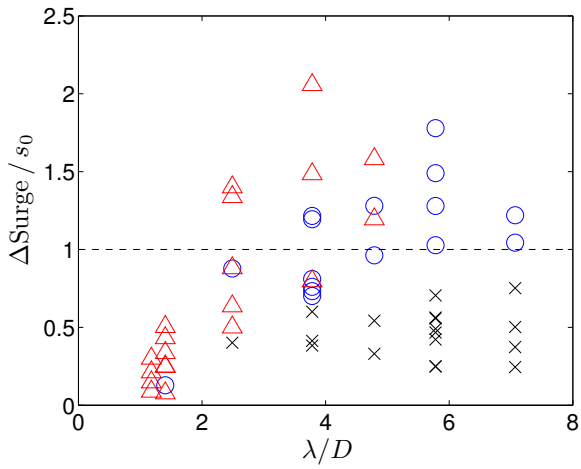

Figure 7.1.9: Relative surge (ΔSurge), normalised with respect to initial separation s_0, as a function of nondimensional wavelength. Symbols as with Figure 7.1.6.

In the non-rafting experiments, collisions due to surge occurred in wavelengths of $\lambda/D > 3.8$. In these experiments, the same occurs for $\lambda/D > 5.7$. In this wavelength regime, $\Delta\text{Surge}/s_0$ is always greater than 1 when collisions occur. For shorter wavelengths, some instances of rafting and non-rafting collisions occur when $\Delta\text{Surge}/s_0$ is less than 1. In these tests, collisions and rafting are caused by drift.

In the rafting experiments, collisions due to drift occur in a larger range of wavelengths compared to the non-rafting experiments. The reason for this difference may due to the characteristics of the mooring systems employed in each experiment. In the rafting experiments, thin elastic cords were used as mooring lines. In the non-rafting experiments, a tighter mooring system, consisting of nylon wires, was used. As a result, the mooring system in the non-rafting experiments exerts more suppression on drift. This causes collisions due to drift to occur over a smaller range of wavelengths.

Overlap

The occurrence of rafting can be determined by quantifying the overlap when floes come into contact. Overlap, $\Delta\widehat{Z}$, is calculated as the difference in vertical coordinates at the trailing edge of Floe F and the leading edge of Floe R. Since the six-degree motions were measured at the top surface of the floes, we calculate the vertical coordinates with respect to the top edges of both floes.

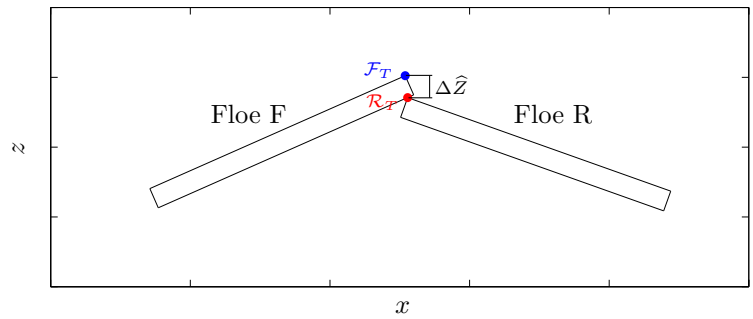

Figure 7.1.10: Overlap, $\Delta\widehat{Z}$, calculated as the difference in z-coordinates at the trailing edge of Floe F, $\mathcal{F}_T$, and leading edge of Floe R, $\mathcal{R}_T$.

Figure 7.1.10 illustrates how overlap is calculated. The surge, heave and pitch signals of both floes are considered when calculating the overlap. If the vertical coordinate of the trailing edge of Floe F is denoted as $\mathcal{F}_T(z)$ and the leading edge of Floe R is $\mathcal{R}_T(z)$, then the overlap $\Delta\widehat{Z} = |\mathcal{F}_T(z) - \mathcal{R}_T(z)|$. The subscript T refers to the top edges of the Floes F and R, which have the z-coordinates

$$\mathcal{F}_T(z) = Z_F + R\sin(\Theta_F) \quad \text{and} \quad \mathcal{R}_T(z) = Z_R - R\sin(\Theta_R). \tag{7.1.1}$$

The parameters Z_F and Θ_F respectively refer to the heave and pitch signals of Floe F

at the time of contact t_c (i.e. when $\widehat{X}_F \geq \widehat{X}_R$). Likewise, Z_R and Θ_R refer to the same quantities for Floe R.

Figure 7.1.11 shows the overlap normalised with respect to the floe thickness H. Results from tests with non-rafting collisions and rafting events are plotted as a function of nondimensional wavelength. A value of $\Delta\widehat{Z}/H \approx 1$ indicates that the overlap is sufficiently large for floes to raft. The figure shows that all instances of rafting coincides with an overlap of $\Delta\widehat{Z}/H > 1$, and all non-rafting collision events occur when $\Delta\widehat{Z}/H < 1$.

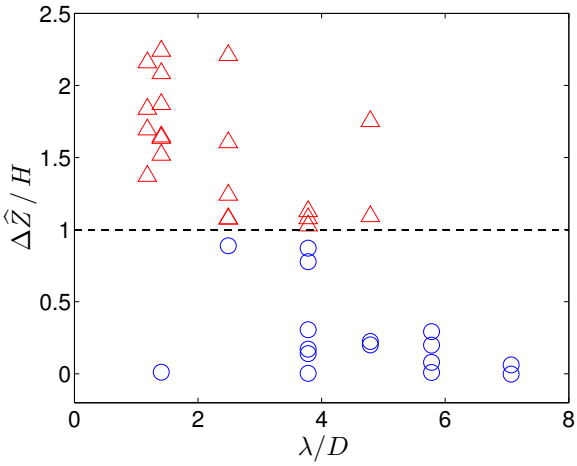

Figure 7.1.11: Overlap, $\Delta\widehat{Z}$, normalised with respect to floe thickness H, as a function of nondimensional wavelength. Symbols as with Figure 7.1.6.

7.2 Extending the two-floe collision model

The collision model of Chapter 6 is modified to predict the occurrence of rafting. The following section describes the modifications to the collision algorithm. This model is available via: `https://github.com/AdelaideUniversityMathSciences/TwoFloeCollisionModels/tree/master/RaftingCollisionModel`.

7.2.1 Criteria for rafting

For the purpose of modelling rafting, floes are visualised as two-dimensional cross-sections on the xz-plane as per Figure 7.2.1. The locations of the top and bottom

corners of Floe F are denoted as $\mathcal{F}_T$ and $\mathcal{F}_B$, respectively. Likewise, the corners of Floe R are denoted as $\mathcal{R}_T$ and $\mathcal{R}_B$.

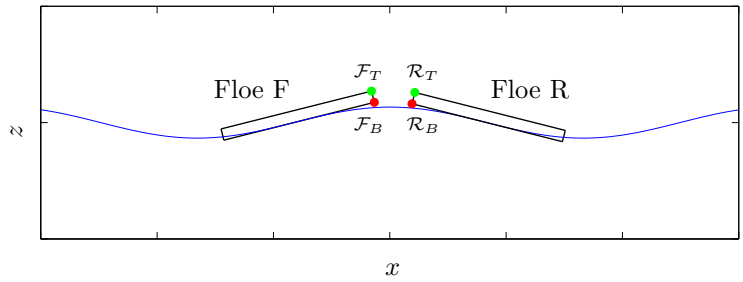

Figure 7.2.1: Floes visualised as 2-D cross-sections. Bullets indicate the locations of points $\mathcal{F}_B$ and $\mathcal{R}_B$ (●), and $\mathcal{F}_T$ and $\mathcal{R}_T$ (●).

The coordinates of $\mathcal{F}_B$ and $\mathcal{R}_B$ are

$$\mathcal{F}_B(x,z) = (\widehat{X}_F, \widehat{Z}_F) \quad \text{and} \quad \mathcal{R}_B(x,z) = (\widehat{X}_R, \widehat{Z}_R). \tag{7.2.1}$$

Recall, $\widehat{X}_F$ and $\widehat{X}_R$ are the x-coordinates of the trailing and leading edges of Floes F and R, respectively, and are defined by Equations (6.1.2) and (6.1.3). Similarly, $\widehat{Z}_F$ and $\widehat{Z}_R$ are the corresponding z-coordinates of Floes F and R, which are calculated using Equation (6.1.1) to give

$$\widehat{Z}_F(t) = Z_F(t) + \frac{R\tan\Theta_F(t)}{\sqrt{1+\tan^2\Theta_F(t)}} \tag{7.2.2}$$

and

$$\widehat{Z}_R(t) = Z_R(t) - \frac{R\tan\Theta_R(t)}{\sqrt{1+\tan^2\Theta_R(t)}}, \tag{7.2.3}$$

with R denoting the floe radius, Z_F and Z_R the heave signals of Floes F and R, and Θ_F and Θ_R the pitch signals of the same.

The coordinates of $\mathcal{F}_T$ and $\mathcal{R}_T$ are therefore

$$\mathcal{F}_T(x,z) = (\widehat{X}_F - H\sin\Theta_F, \widehat{Z}_F + H\cos\Theta_F) \tag{7.2.4}$$

and

$$\mathcal{R}_T(x,z) = (\widehat{X}_R - H\sin\Theta_R, \widehat{Z}_R + H\cos\Theta_R), \tag{7.2.5}$$

where H is the floe thickness. If slope-sliding theory is used to model floe motions,

then pitch will be equivalent to the wave angle ($\Theta = \arctan \partial\eta/\partial x$), and heave will be equivalent to the wave profile ($Z = \eta$).

Figure 7.2.2 shows the collision algorithm when rafting is included. Modifications to the previous model in § 6.1 are highlighted in red. Previously, collisions were defined based on the difference in x-coordinates of the trailing and leading edges of Floes F and R. Collision events are now defined to occur when the boundaries of Floes F and R intersect.

If the boundaries of both floes intersect, the coordinates of points $\mathcal{F}_T$, $\mathcal{F}_B$, $\mathcal{R}_T$ and $\mathcal{R}_B$ are compared at the time of contact, t_c, to determine if rafting has occurred. A rafting event is noted when either (i) the z-coordinates of $\mathcal{F}_T$ is less than $\mathcal{R}_B$, which implies Floe R is on top of Floe F, or (ii) the z-coordinates of $\mathcal{F}_B$ is greater than $\mathcal{R}_T$, which implies Floe F is on top of Floe R. When a rafting event occurs, the simulation ends. If a non-rafting collision event is noted, the simulation proceeds as usual.

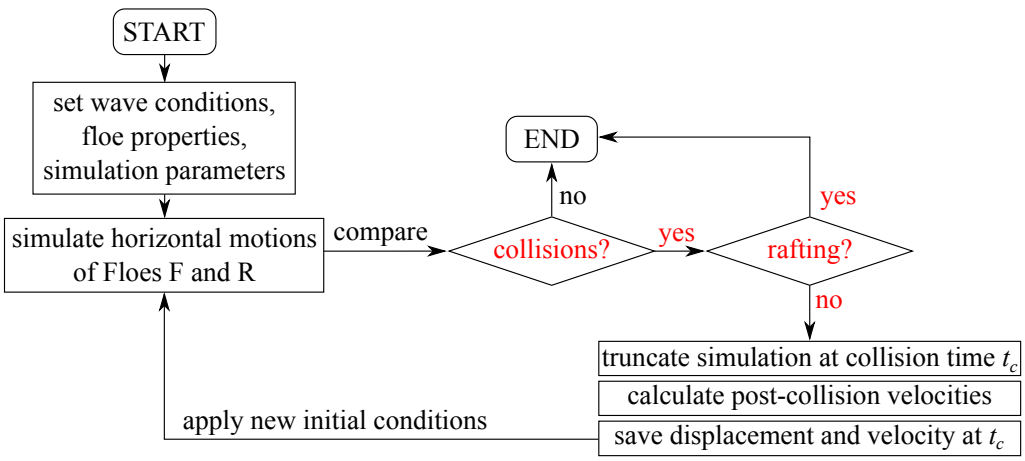

Figure 7.2.2: Flowchart for collision and rafting algorithm.

7.2.2 Tuning parameters

In the modified version of the collision model, spring and damping coefficients were tuned using data from a set of mooring tests. In these tests, a single floe was extended by a set distance $X(0)$ and released in calm waters. These tests, which were not performed in the non-rafting experiments, provide an alternative and more straightforward method for tuning the mooring coefficients, especially since wave

forcing is excluded from the simulations. Recall, in the non-rafting experiments, mooring coefficients were tuned using the x-displacements of floes in long-wavelength tests where collisions did not occur (see § 6.2.3).

Mooring tests were performed using 4 extension lengths ranging from approximately 0.4 m to 1 m. Extension lengths were confirmed via video measurements. Tests for the longest extension, $X(0) = 1\,\mathrm{m}$, were repeated to ensure accuracy of the motion-capture system. A total of 5 mooring tests were performed.

Figure 7.2.3 shows the floe's measured x-displacement when $X(0) = 0.65\,\mathrm{m}$. Overlaid are horizontal motions simulated using the slope-sliding equation of motion (6.2.1), but with wave forcing terms $\partial\eta/\partial x = V_w = 0$. For consistency with all previous results, an added mass coefficient of $c_m = 0.1$ is used in all simulations.

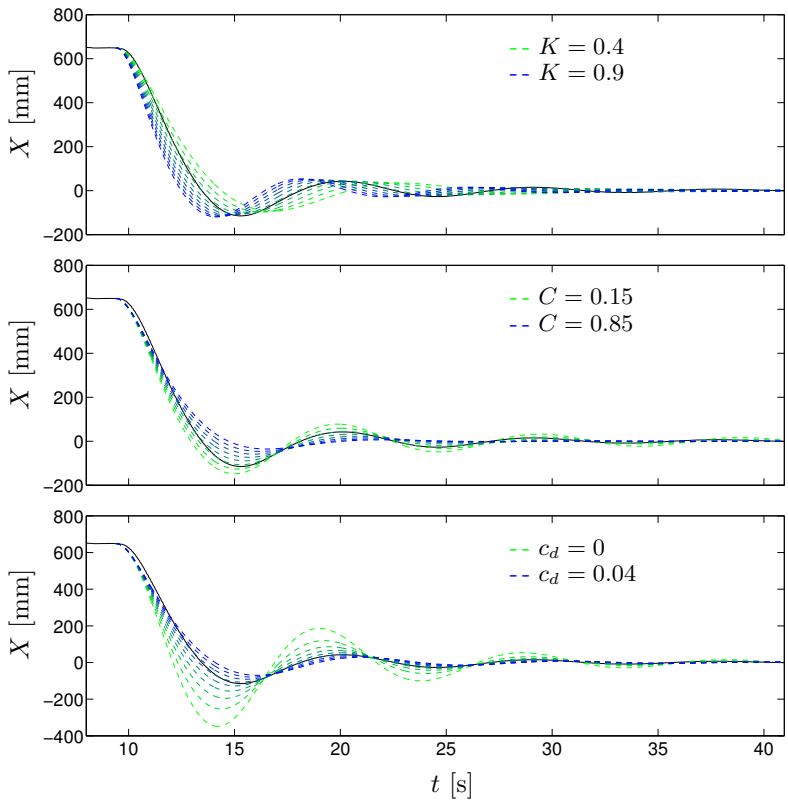

Figure 7.2.3: Effect of spring coefficient K, damping coefficient C and drag coefficient c_d (top to bottom panels, respectively) on horizontal motions. Except where otherwise specified, $K = 0.6$, $C = 0.35$, $c_d = 0.025$ and $c_m = 0.1$. Experimental data from mooring test (−) overlaid for comparison.

The effect of the spring coefficient K is demonstrated in the top panel of Figure 7.2.3. Here, spring coefficients ranging from $K = 0.4$ to 0.9 are considered. Other param-

eters are kept constant at $C = 0.35$ and $c_d = 0.025$. The spring coefficient affects (i) the amplitude of oscillations about the equilibrium, and (ii) the frequency of oscillations. The former is akin to the effect demonstrated in the tope panel of Figure 6.2.2 (see § 6.2.3 for discussion). A larger value of K results in smaller oscillation amplitudes and higher oscillation frequencies.

In the middle panel of Figure 7.2.3, the effect of the damping coefficient C is shown through simulations of floe displacements over a range of $C = 0.15$ to 0.85. All other parameters, apart from $K = 0.6$, remain unchanged from the previous example. The figure demonstrates how the damping coefficient affects the decay envelope of oscillations about the equilibrium. The larger the damping coefficient, the larger the rate of decay. Motions therefore return to a steady-state equilibrium in a shorter amount of time. Again, this is consistent with the results in § 6.2.3.

The effect of the drag coefficient is also investigated using data from the mooring tests. The bottom panel of Figure 7.2.3 shows the floe displacements when c_d is increased from 0 to 0.04. Recall, this range of drag coefficients was determined by parameterising the collision model using data from the non-rafting experiments (see § 6.2.4). Larger values of drag are shown to decrease the amplitude and period of oscillations, however its effect is only significant in the first 25 s when the floe's velocity is large. Recall that the drag force is proportional to the square of the velocity of the floe in comparison to the fluid velocity.

Overall, the values $K = 0.6$, $C = 0.35$, $c_d = 0.025$ and $c_m = 0.1$ gave the best agreement with data from all five mooring tests. The spring coefficient is noted to be larger than in the non-rafting experiments ($K = 0.32$). This translates to a larger restoring force. The damping coefficient, however, is smaller ($C = 0.5$, previously), therefore motions decay to a steady-state equilibrium at a slower rate. The responses of both mooring systems are compared in Figure 7.2.4. Floe motions are simulated in the absence of waves, as with the mooring tests. Consistent drag ($c_d = 0.025$) and added mass ($c_m = 0.1$) coefficients are used. Figure 7.2.4 demonstrates how the mooring system in the non-rafting experiments is more restrictive to the horizontal motions of a floe. When the mooring coefficients of the non-rafting experiments are applied, floes drift at lower velocities, oscillate with smaller amplitudes and decay to a steady-state equilibrium at a faster rate. This simulation validates our explanation

of why collisions caused by drift occur over a smaller range of wavelengths in the non-rafting experiments (see 7.1.2).

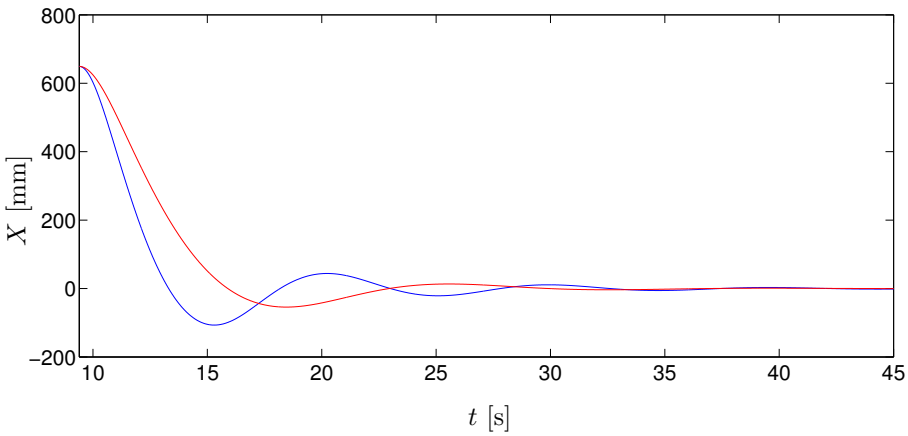

Figure 7.2.4: Floe responses simulated using the mooring coefficients of the non-rafting experiments (−) and rafting experiments (−).

7.3 Model-data comparisons

To confirm the collision and rafting behaviours observed in the experiments, it is important that all input parameters in the collision model are tuned to be as close as possible to the experiments. Because of the inaccuracies of wave probe measurements, all wave probe data was disregarded, therefore transient wave amplitudes could not be parameterised. Recall that parameterisation of the transient wave function is important for tuning the drag coefficient accurately (see § 6.2). To resolve this issue, we applied the following parameters to the transient wave profile function $\eta = \alpha t^{\beta} \sin(kx - \omega t + \gamma)$, for $0 \leq t < t_s$:

$$\alpha = a/t_s^{\beta}, \qquad \beta = 3, \qquad \gamma = 0 \qquad \text{and} \quad t_s = 5\,\text{s}. \tag{7.3.1}$$

Recall, t_s is the transient to steady-state time partition. In the above, we assume that the transient wave amplitude follows a cubic relationship with time, therefore $\beta = 3$. A drag coefficient $c_d = 0.025$ is also applied to the model. Recall, this value was derived by tuning the model using data from the mooring tests. This coefficient is therefore representative of drag in calm waters. In the presence of waves, we expect the drag coefficient to increase, especially in the short-wavelength regime

(see § 6.2.4). Again, because of the issues with the wave probes, it was difficult to determine values of c_d without accurate inputs for wave amplitudes.

Bearing in mind these considerations, the collision model was used to simulate the collision and rafting behaviours of a two-floe system. Figure 7.3.1 shows the occurrence of rafting, non-rafting collisions and no collisions as predicted by the collision model, in comparison to experimental results as per Figure 7.1.6. Two-floe interactions are simulated over the same range of wavelengths as the experiments, and at every 2.5 mm interval for wave amplitudes between 10 to 50 mm. This is done in order to test the model's sensitivity to changes in wave amplitudes.

Model predictions are generally accurate for wavelengths larger than $\lambda/D \approx 2.5$. In this range of wavelengths, only 4 out of 22 tests for $s_0 = 30$ mm and 3 out of 22 tests for $s_0 = 60$ mm did not agree with the model. The overall accuracy over this range of wavelengths is therefore 84%. In terms of predicting rafting events, the model agrees with experiments in 6 out of 11 tests.

For wavelengths less than $\lambda/D \approx 1.5$, only 3 out of 12 tests (from both initial separations) agreed with model predictions. This is expected, given the limitations of slope-sliding theory in the short-wavelength regime, and the large differences between model and data from the non-rafting experiments as described in § 6.3.

Note that a certain degree of caution is required when interpreting the accuracy of the collision model based on Figure 7.3.1. The figure indicates the occurrence of rafting and collisions only, and does not reflect the accuracy in terms of floe displacements. Figure 7.3.2 shows an example of the model and experiments agreeing on the occurrence of rafting, but with poor agreement for horizontal displacements. In this example, $a = 40$ mm and $\lambda/D = 2.5$. The model predicts a single non-rafting collision occurring at $t = 7.2$ s, and a rafting event occurring at $t = 12$ s (simulations end thereafter). Both displacements and collision behaviours are very different to the corresponding experiment. Discrepancies are likely caused by differences in wave amplitudes and the inaccurate tuning of the drag coefficient.

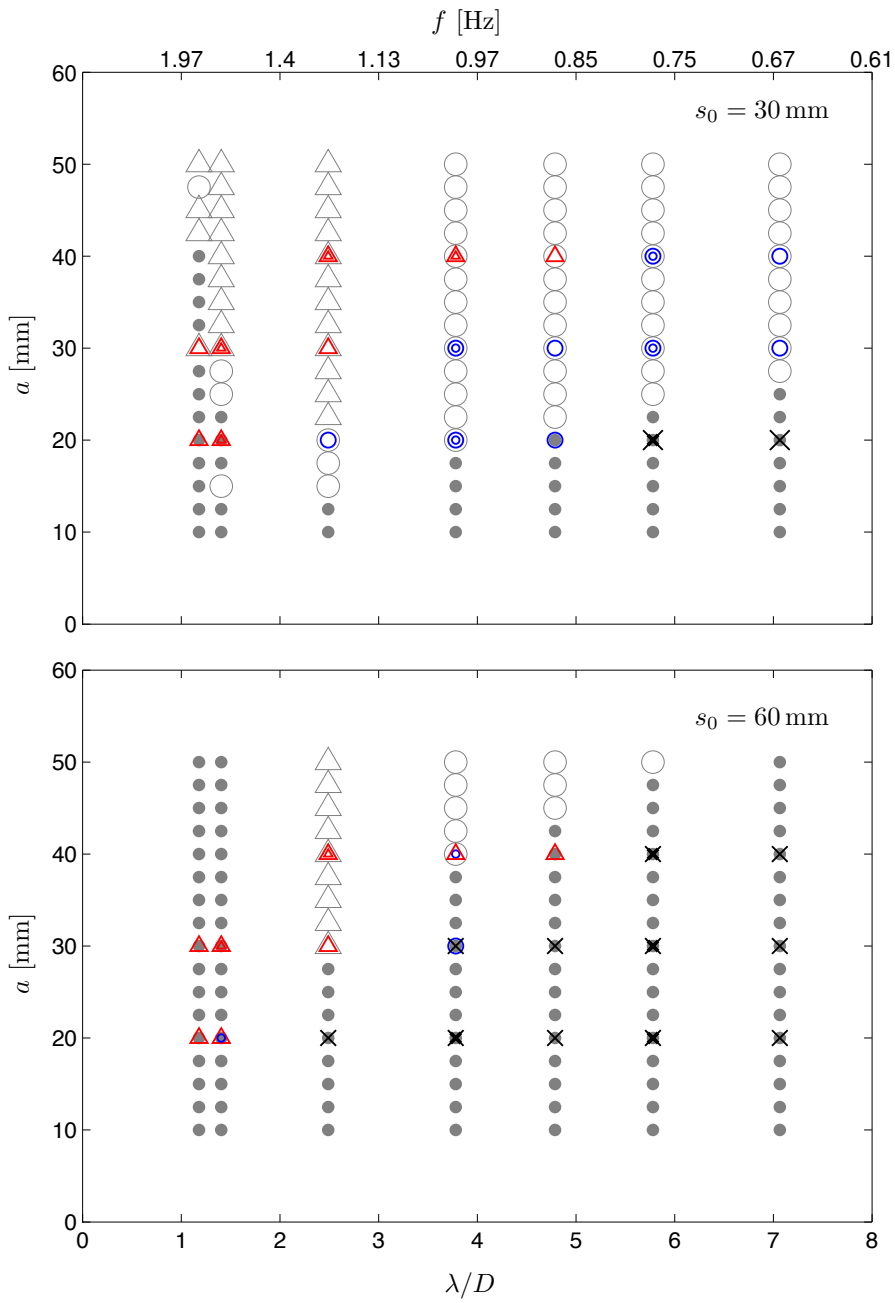

Figure 7.3.1: As with Figure 7.1.6 but with model predictions (in grey) overlaid onto experimental data. Symbols denote simulations with rafting (△), non-rafting collisions (○) and no collisions (•).

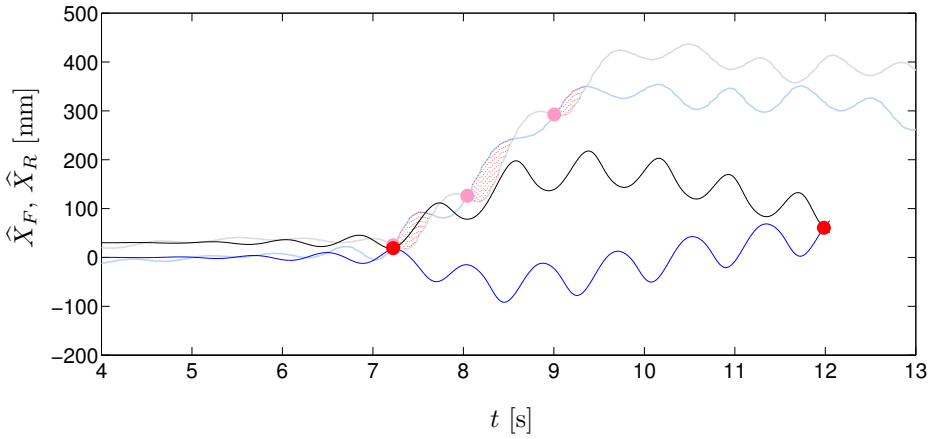

Figure 7.3.2: Example of rafting predicted by the collision model (black, blue curves and red bullets), with poor agreement for displacements. Experiment data (shaded curves and bullets) overlaid for comparison.

7.4 Summary

In this chapter, results from a third round of wave basin experiments were presented. The focus of these experiments was to investigate the occurrence of rafting between two floes in regular waves. Apart from the absence of edge barriers and a slightly smaller mass, floes were identical to the ones used in the previous two experiments. The motions of the two floes were recorded in nondimensional wavelengths between 1.2 and 7.1 (with respect to floe diameter), and in wave steepnesses from 0.04 to 0.4. Two initial separations (30 mm and 60 mm) were considered. It was noted that measured wave amplitudes were inaccurate, therefore all results were reported using target values.

The regimes of rafting, non-rafting collisions and no collisions were presented as a function of target wave amplitude and incident wavelength. Rafting was shown to occur in shorter wavelengths and in steeper waves. Three rafting behaviours exist: The first is defined by prolonged contact between floes. This occurs as a result of large drift forces from incident waves. This behaviour occurred in the shortest wavelengths. The second rafting behaviour is defined by short-contact rafting events, and occurred in slightly longer wavelengths. The third behaviour is a transition between short-contact rafting and non-rafting collisions, and contains both types of events. This transient regime occurred in intermediate wavelengths and large amplitude waves.

For a smaller initial separation, non-rafting collisions occurred in intermediate to large wavelengths and were more common in medium to low amplitude waves. No collision events were observed for the longest wavelengths and smallest wave amplitudes. When the initial separation was increased, the regime of no collisions expanded over shorter wavelengths. Rafting regimes generally remained unchanged.

The relative surge between the two floes was also quantified with respect to the initial separation. Results were similar to the non-rafting experiments. The only notable difference was that collision/rafting events caused by drift were present in longer wavelengths compared to the non-rafting experiments. This was due to the use of a more elastic mooring, which permitted drift in longer wavelengths.

Overlap was also quantified to confirm rafting events when floes collided. Overlap was calculated by considering the vertical coordinates at the closest edges of each floe. All instances of rafting coincided with an overlap larger than the floe thickness.

In the second part of the chapter, modifications to the two-floe collision model in Chapter 6 were presented. Floes were represented as two-dimensional cross-sections. Rafting and collision events were defined by the intersection of their boundaries. Comparisons with experimental data yielded accurate results for the occurrence of rafting and collisions, in wavelengths longer than 2.5 times the floe diameter. Large discrepancies were observed for shorter wavelengths, due to the invalidity of slope-sliding theory in this wavelength regime. It was shown that although the model could predict the occurrence of rafting correctly in some cases, there were instances when floe displacements were largely different to those in the experiments. Differences were attributed to the inaccuracies of wave amplitude data and drag coefficients.

Chapter 8

Conclusions

In this thesis, our goal was to model the wave-induced collisions of ice floes. Floe collisions were simulated by firstly developing theoretical and experimental models of solitary floes in waves. Chapter 2 described the experimental methods employed to simulate the oscillatory surge, heave and pitch, and drift motions of solitary floes in regular waves. Tests were conducted over a range of incident wavelengths and wave amplitudes, which corresponded to wave steepnesses within the linear wave regime. In the experiments, thin plastic disks were used to represent ice floes. Two floes of identical dimensions were tested – one had an edge barrier to prevent wave overwash, and the other had no barrier. The major findings from the single-floe experiments were:

1. Surge, heave and pitch amplitudes were linear with respect to wave amplitude, except in instances where overwash occurred.

2. Overwash, which occurred in short wavelengths and increased in depth with increasing wave steepnesses, damped the oscillatory motions of the floe without a barrier.

3. When oscillatory motions were normalised with respect to wave motions (and expressed as response amplitude operators, RAOs), we observed that in long wavelengths, RAOs were approximately unit valued, i.e. floes behaved like fluid particles at the free-surface, In short wavelengths, oscillatory motions decreased with decreasing wavelength.

4. Short- and long-wavelength regimes were defined by the oscillatory responses of floes with respect to wave motions. Wavelength regimes were delineated by an incident wavelength to floe diameter quotient $\lambda/D = 3$.

5. Drift velocities of both floes increased with wave steepness. We showed (through comparisons with other related experiments) that an inverse relationship exists between floe mass and drift velocity.

Two theoretical single-floe models were investigated. Chapter 3 presented a one-dimensional model based on slope-sliding theory. In the slope-sliding model, a floe is driven by wave forces proportional to the slope of an unmodified wavefield. This model applies the Froude-Kryloff assumption which states that wavefields are unaffected when the horizontal dimensions of submerged bodies are small in comparison to incident wavelengths. Horizontal floe displacements were calculated by solving an ordinary differential equation of motion.

Chapter 4 investigated a two-dimensional model (length and depth dimensions) based on linear potential-flow theory. The linearised model was derived based on the assumptions of small wave steepnesses and floe motions. In the model, floe motions are induced by hydrodynamic forces around the floe's wetted surfaces. Floe motions were calculated by solving a boundary value problem using the eigenfunction matching method. The model was used to calculate the surge, heave and pitch amplitudes of a solitary floe.

Both models were compared and validated using results from the single-floe experiments. It was found that:

1. When drag and added mass terms were ignored, the slope-sliding and potential-flow models gave identical solutions for surge RAOs in the long-wavelength limit. This was confirmed via analytical solutions.

2. The potential-flow model was more accurate than the slope-sliding model in the short-wavelength regime.

3. In the long-wavelength regime, the potential-flow model slightly overpredicted the RAOs. The slope-sliding model was more accurate in the long-wavelength regime due to the availability of a tuning coefficient for added mass. An

added mass coefficient $c_m = 0.1$ gave best model-data agreement in the long-wavelength regime.

In Chapter 5, results from a second round of wave basin experiments were presented. In these experiments, the non-rafting collisions of two adjacent floes were investigated in wave conditions similar to the single-floe experiments. Dimensions of both floes were identical to the ones used the first round of experiments. Both had edge barriers to prevent rafting.

Three collision behaviours were observed: (i) floes collided repeatedly; (ii) floes collided in the initial phase and remained separated; (iii) floes did not come into contact at all. Results from the non-rafting experiments showed that:

1. Floes do not collide in the longest and shortest wavelengths. In long waves floes do not collide because they surge approximately in phase. In short waves surge amplitudes are not large enough (relative to floe separations) to cause collisions.

2. Floes collide in intermediate wavelengths and collisions occur over a larger range of wavelengths when the incident wave amplitude is increased.

3. In long waves, collisions are caused by surge only. In short waves, collisions could be caused by surge or drift. The cause of collisions were determined by quantifying the relative surge with respect to initial separation.

To extend our investigation to rafting, a third round of wave basin experiments was conducted to simulate rafting and collisions between two adjacent floes. Edge barriers were removed to allow rafting to occur. Two initial separations (30 mm and 60 mm) were considered. Chapter 7 presented the results from these experiments.

Three rafting behaviours were observed in the experiments: (i) floes rafted for prolonged durations (long-contact); (ii) floes rafted for short durations (short-contact); (iii) floes transitioned between non-rafting collisions and short-contact rafting events throughout a given test. Experimental results showed that:

1. When the initial separation was 30 mm, non-rafting collisions occurred in intermediate to large wavelengths and were more common in medium to low

amplitude waves. No collisions occurred in the longest wavelengths and smallest wave amplitudes.

2. Long-contact rafting events occurred in the shortest wavelengths, and were correlated with strong drift motions. Short-contact rafting events occurred in slightly longer wavelengths. Transient rafting behaviours occurred in intermediate wavelengths and large amplitude waves.

3. When the initial separation increased to 60 mm, the occurrence of non-rafting collisions decreased and the regimes of no collisions increased over shorter wavelengths. Rafting regimes, however, were mostly unaffected by the increase in separation.

The relative surge was also quantified in Chapter 7 and results confirmed the findings of Chapter 5 that surge alone caused collisions in the long-wavelength regime, and surge and drift caused collisions/rafting in shorter wavelengths.

In Chapter 6, a collision model was developed to simulate the interactions of two floes. The model, which was based on modifications to the models of Shen and Ackley (1991) and Shen and Squire (1998), applied slope-sliding theory to calculate floe motions in time. A time-stepping algorithm was implemented to predict the occurrence of collisions. The two-floe collision model was extended in Chapter 7 to predict the occurrence of rafting. Model predictions were validated using data from both non-rafting and rafting experiments. Comparisons showed that:

1. Theoretical predictions were accurate in the long-wavelength regime. Accuracy was determined based on predictions of collision events and comparisons of mean collision frequencies and velocities.

2. Model accuracy was subject to proper tuning of the drag coefficient in the slope-sliding equation of motion. Drag coefficients increased with wave frequency. We hypothesised that this was associated with the increase in form drag as the submerged profile of floes increases with wave frequency.

3. In the short-wavelength regime, simulations of collisions and rafting were largely inaccurate. The main reason for this was the invalidity of slope-sliding theory in regimes where wave scattering is dominant.

This thesis has addressed the need for validation of collision models based on slope-sliding theory. We have shown that the slope-sliding model can be used to predict collisions accurately in intermediate to long wavelengths. In the short-wavelength regime, wave scattering significantly complicates the collision process. Experimental results have shown that a large part of the rafting regime occurs in short wavelengths. Therefore, more attention needs to be given to modelling collisions and rafting in the short-wavelength regime.

To further improve the collision model, linear potential-flow theory may be implemented such that the effects of wave scattering are considered. This can be done by simply modifying the simulation kernel of the two-floe collision model. However the potential-flow model will need to be solved in the time-domain and will need to be modified to account for drift and drag forces. Drag, as we have seen, has a significant effect on collision properties. Wave basin experiments have shown that drift motions are dominant in the short-wavelength regime and are responsible for causing collisions. Chapter 5 of Faltinsen (1990) lays the foundation for the inclusion of drift forces in the linear potential-flow model.

The collision model can also be improved by simulating the mechanical/hydrodynamic interactions of rafted floes. Currently, the collision model does not proceed with simulations after a rafting event has been noted. The development of rafting models would be considerably challenging. However, with the results and observations from the rafting experiments, we have a reference as to what physical effects will need to be accounted for in the rafting model.

Moving forward, the next natural progression would be to extend the collision model to simulate the interactions of larger groups of floes (in both longitudinal and transverse axes). Several multiple floe models, based on potential-flow theory, have been developed (e.g. Masson and LeBlond, 1989; Meylan et al., 1997; Bennetts et al., 2010), however none of these models consider the effects of floe collisions.

Bibliography

Bai, W., Zhang, T., and McGovern, D. J. (2016). Response of sea ice floes in regular waves: a comparison of numerical and experimental results. *Ocean Engineering*, 10.1016/j.oceaneng.2016.10.045.

Bailey, E., Feltham, D. L., and Sammonds, P. R. (2010). A model for the consolidation of rafted sea ice. *Journal of Geophysical Research: Oceans*, 115(4):1–14.

Bennetts, L. G., Peter, M. A., Squire, V. A., and Meylan, M. H. (2010). A three-dimensional model of wave attenuation in the marginal ice zone. *Journal of Geophysical Research*, 115(C12043).

Bennetts, L. G. and Squire, V. A. (2012). On the calculation of an attenuation coefficient for transects of ice-covered ocean. *Proceedings of the Royal Society A*, 468(2137):136–162.

Bennetts, L. G. and Williams, T. D. (2015). Water wave transmission by an array of floating disks. *Proceedings of the Royal Society A*, 471(20140698).

Bennetts, L. G., Yiew, L. J., Meylan, M. H., French, B. J., and Thomas, G. A. (2014). An experimental model of non-rafting collisions between ice floes caused by monochromatic water waves. In *Proceedings of the 19th Australasian Fluid Mechanics Conference*.

Bessho, M. (1965). On the wave-free distribution in the oscillation problem of the ship. *Journal of Zosen Kiokai*, 117:127–138.

Black, J. L., Mei, C. C., and Bray, M. C. G. (1971). Radiation and scattering of water waves by rigid bodies. *Journal of Fluid Mechanics*, 46:151–164.

Dai, M., Shen, H. H., Hopkins, M. A., and Ackley, S. F. (2004). Wave rafting and the equilibrium pancake ice cover thickness. *Journal of Geophysical Research*, 109(C07023).

Dean, R. G. and Dalrymple, R. A. (1991). *Water Wave Mechanics for Engineers and Scientists*. World Scientific.

Faltinsen, O. M. (1990). *Sea Loads on Ships and Offshore Structures*. Cambridge University Press, 1st edition.

Feltham, D. L. (2005). Granular flow in the marginal ice zone. *Philosophical Transactions of the Royal Society A*, 363(1832):1677–1700.

Feltham, D. L. (2008). Sea Ice Rheology. *Annual Review of Fluid Mechanics*, 40(1):91–112.

Frankenstein, S. (1996). *The Effects of Waves on Pancake Ice*. PhD thesis, Clarkson University.

Gao, L. (1991). *Ice Floe Collision under Wave Action in the Marginal Ice Zone*. PhD thesis, Memorial University of Newfoundland.

Grotmaack, R. and Meylan, M. H. (2006). Wave forcing on small floating bodies. *Journal of Waterway, Port, Coastal, and Ocean Engineering*, 132:192–198.

Herman, A. (2011). Molecular-dynamics simulation of clustering processes in sea-ice floes. *Physical Review E*, 84(056104).

Herman, A. (2012). Influence of ice concentration and floe-size distribution on cluster formation in sea-ice floes. *Central European Journal of Physics*, 10(3):715–722.

Herman, A. (2013). Numerical modeling of force and contact networks in fragmented sea ice. *Annals of Glaciology*, 54(62):114–120.

Hirsch, M. W., Smale, S., and Devaney, R. L. (2013). *Differential Equations, Dynamical Systems, and an Introduction to Chaos*. Elsevier, 3rd edition.

Hopkins, M. A., Tuhkuri, J., and Lensu, M. (1999). Rafting and ridging of thin ice sheets. *Journal of Geophysical Research*, 104:13605.

Huang, G., Huang, Z. H., and Law, A. W. K. (2016a). Analytical Study on the Drift of Small Floating Objects under Regular Waves. *Journal of Engineering Mechanics*, 142(6).

Huang, G., Law, A. W. K., and Huang, Z. (2011). Wave-induced drift of small floating objects in regular waves. *Ocean Engineering*, 38(4):712–718.

Huang, G., Zhang, N., Law, A. W.-K., Song, Y., and Lin, L. (2016b). Motion response of immersing tunnel element under random waves. *Ships and Offshore Structures*, 11(6):561–574.

John, F. (1949). On the motion of floating bodies I. *Communications on Pure and Applied Mathematics*, 2(1):13–57.

Keller, J. B. (1998). Gravity waves on water. *Journal of Geophysical Research*, 103(C4):7663–7669.

Kohout, A. L. and Meylan, M. H. (2008). An elastic plate model for wave attenuation and ice floe breaking in the marginal ice zone. *Journal of Geophysical Research: Oceans*, 113(9):1–17.

Langhorne, P. J., Squire, V. A., Fox, C., and Haskell, T. G. (1998). Break-up of sea ice by ocean waves. *Annals of Glaciology*, 27:438–442.

Law, A. W. K. and Huang, G. (2007). Observations and measurements of wave-induced drift of surface inextensible film in deep and shallow waters. *Ocean Engineering*, 34(1):94–102.

Lee, H. H., Chen, L. Y., Weng, W. K., and Shyue, S. W. (2007). The prediction of the dynamic and structural motions of a floating-pier system in waves. *Ocean Engineering*, 34(7):1044–1059.

Lee, J. F. (1995). On the heave radiation of a rectangular structure. *Ocean Engineering*, 22(1):19–34.

Lever, J. H., Reimer, E., and Diemand, D. (1988). A Model Study of the Wave-Induced Motion of Small Icebergs and Bergy Bits. *Journal of Offshore Mechanics and Arctic Engineering*, 110(1):101.

Linton, C. M. and McIver, P. (2001). *Handbook of Mathematical Techniques for Wave/Structure Interactions*. Chapman & Hall/CRC Press.

Liu, A. K. and Mollo-Christensen, E. (1988). Wave propagation in a solid ice pack. *Journal of Physical Oceanography*, 18:1702–1712.

Lu, Q. M., Larsen, J., and Tryde, P. (1989). On the role of ice interaction due to floe collisions in marginal ice zone dynamics. *Journal of Geophysical Research*, 94(C10):14525–14537.

Luk, C. H. (1987). Added mass and damping for ice floes by long water wave theory. *Journal of Waterway, Port, Coastal, and Ocean Engineering*, 113(5):523–539.

Madsen, O. S. and Bruno, M. S. (1987). A methodology for the determination of drag coefficients for ice floes. *Journal of Offshore Mechanics and Arctic Engineering*, 109:381–387.

Marchenko, A. V. (1999). The floating behaviour of a small body acted upon by a surface wave. *Journal of Applied Mathematics and Mechanics*, 63(3):471–478.

Martin, S. and Becker, P. (1987). High frequency ice floe collisions in the Greenland Sea during the 1984 Marginal Ice Zone experiment. *Journal of Geophysical Research: Oceans*, 92(C7):7071–7084.

Martin, S. and Becker, P. (1988). Ice floe collisions and their relation to ice deformation in the Bering Sea during February 1983. *Journal of Geophysical Research: Oceans*, 93(C2):1303–1315.

Massom, R. A. and Stammerjohn, S. E. (2010). Antarctic sea ice change and variability - Physical and ecological implications. *Polar Science*, 4(2):149–186.

Masson, D. and LeBlond, P. H. (1989). Spectral evolution of wind-generated surface gravity waves in a dispersed ice field. *Journal of Fluid Mechanics*, 202:43–81.

MATLAB (2012). *version 8.0.0.783 (R2012b)*. The MathWorks Inc., Natick, Massachusetts.

McGovern, D. J. and Bai, W. (2014). Experimental study on kinematics of sea ice floes in regular waves. *Cold Regions Science and Technology*, 103:15–30.

McKenna, R. F. and Crocker, G. B. (1990). Wave energy and floe collisions in marginal ice zones. In *Ice Technology for Polar Operations, Proceedings of the 2nd International Conference on Ice Technology*, pages 33–41, Southampton. Computational Mechanics Publications.

Mei, C. C., Stiassnie, M., and Yue, D. K. P. (2005). *Theory and Applications of Ocean Surface Waves. Part 1: Linear Aspects.* World Scientific.

Meylan, M. H. and Squire, V. A. (1993a). A model for the motion and bending of an ice floe in ocean waves. *International Journal of Offshore and Polar Engineering*, 3(4):322–323.

Meylan, M. H. and Squire, V. A. (1993b). Finite-floe wave reflection and transmission coefficients from a semi-infinite model. *Journal of Geophysical Research*, 98(C7):12537.

Meylan, M. H. and Squire, V. A. (1994). The response of ice floes to ocean waves. *Journal of Geophysical Research*, 99(C1):891–900.

Meylan, M. H., Squire, V. A., and Fox, C. (1997). Towards realism in modeling ocean wave behavior in marginal ice zones. *Journal of Geophysical Research*, 102(C10):22981–22991.

Montiel, F. (2012). *Numerical and Experimental Analysis of Water Wave Scattering by Floating Elastic Plates.* PhD thesis, University of Otago.

Montiel, F., Bennetts, L. G., Squire, V. A., Bonnefoy, F., and Ferrant, P. (2013a). Hydroelastic response of floating elastic discs to regular waves. Part 2. Modal analysis. *Journal of Fluid Mechanics*, 723:629–652.

Montiel, F., Bonnefoy, F., Ferrant, P., Bennetts, L. G., Squire, V. A., and Marsault, P. (2013b). Hydroelastic response of floating elastic discs to regular waves. Part 1. Wave basin experiments. *Journal of Fluid Mechanics*, 723:629–652.

Morison, J. R., Johnson, J. W., and Schaaf, S. A. (1950). The Force Exerted by Surface Waves on Piles. *Journal of Petroleum Technology*, 2(5):149–154.

Murray, J. J., Guy, G. B., and Muggeridge, D. B. (1983). Response of modelled ice masses to regular waves and regular wave groups. In *Proceedings of the International Conference on Oceans, 2*, pages 1048–1052, San Francisco.

Newman, J. N. (1975). Interaction of waves with two-dimensional obstacles: a relation between the radiation and scattering problems. *Journal of Fluid Mechanics*, 71(2):273–282.

Newman, J. N. (1977). *Marine Hydrodynamics*. MIT Press.

Parkinson, C. L. and DiGirolamo, N. E. (2016). New visualizations highlight new information on the contrasting Arctic and Antarctic sea-ice trends since the late 1970s. *Remote Sensing of Environment*, 183:198–204.

Parmerter, R. R. (1975). A model of simple rafting in sea ice. *Journal of Geophysical Research*, 80(15):1948.

Phillips, O. M. (1977). *The Dynamics of the Upper Ocean*. Cambridge University Press.

Prinsenberg, S. J. and Peterson, I. K. (2011). Observing regional-scale pack-ice decay processes with helicopter-borne sensors and moored upward-looking sonars. *Annals of Glaciology*, 52(57):35–42.

Rothrock, D. A. and Thorndike, A. S. (1984). Measuring the sea ice floe size distribution. *Journal of Geophysical Research*, 89:6477–6486.

Rottier, P. J. (1992). Floe pair interaction event rates in the Marginal Ice Zone. *Journal of Geophysical Research*, 97(C6):9391–9400.

Rumer, R. R., Crissman, R. D., and Wake, A. (1979). *Ice Transport in Great Lakes*. Great Lakes Environmental Research Laboratory, National Oceanic and Atmospheric Administration, U.S. Dept. of Commerce.

Shen, H. H. and Ackley, S. F. (1991). A one-dimensional model for wave-induced ice-floe collisions. *Annals of Glaciology*, 15:87–95.

Shen, H. H., Hibler, W. D., and Leppäranta, M. (1987). The role of floe collisions in sea ice rheology. *Journal of Geophysical Research*, 92(C7):7085–7096.

Shen, H. H. and Squire, V. A. (1998). Wave damping in compact pancake ice fields due to interactions between pancakes. In *Antarctic Sea Ice: Physical Processes, Interactions and Varaibility*, volume 74, pages 325–341. American Geophysical Union, Washington, D.C.

Skene, D. M., Bennetts, L. G., Meylan, M. H., and Toffoli, A. (2015). Modelling water wave overwash of a thin floating plate. *Journal of Fluid Mechanics*, 777(2015):R3.

Sommerfeld, A. (1949). *Partial Differential Equations in Physics*. Academic Press, New York, New York.

Song, Y., Huang, G., Pei, Y., Shi, X., Zhang, N., and Lin, L. (2014). Dynamic Responses of Immersing Tunnel Element During Freeboard Elimination. *International Journal of Offshore and Polar Engineering*, 24(4):262–268.

Squire, V. A. (2007). Of ocean waves and sea-ice revisited. *Cold Regions Science and Technology*, 49(2):110–133.

Squire, V. A., Dugan, J. P., Wadhams, P., Rottier, P. J., and Liu, A. K. (1995). Of ocean waves and sea ice. *Annual Review of Fluid Mechanics*, 27:115–168.

Squire, V. A. and Moore, S. C. (1980). Direct measurement of the attenuation of ocean waves by pack ice. *Nature*, 283(5745):365–368.

Squire, V. A., Williams, T. D., and Bennetts, L. G. (2013). Better operational forecasting for contemporary Arctic via ocean wave integration. *International Journal of Offshore and Polar Engineering*, 23(2):81–88.

Stephenson, S. R., Smith, L. C., and Agnew, J. A. (2011). Divergent long-term trajectories of human access to the Arctic. *Nature Climate Change*, 1(6):156–160.

Stroeve, J. C., Serreze, M. C., Holland, M. M., Kay, J. E., Malanik, J., and Barrett, A. P. (2012). The Arctic's rapidly shrinking sea ice cover: A research synthesis. *Climatic Change*, 110(3-4):1005–1027.

Wadhams, P. (1973). Attenuation of swell by sea ice. *Journal of Geophysical Research*, 78(1):3552–3563.

Wadhams, P. (1986). The Seasonal Ice Zone. In *The Geophysics of Sea Ice*, pages 825–991. Springer US.

Wadhams, P., Gill, A. E., and Linden, P. F. (1979). Transects by submarine of the East Greenland Polar Front. *Deep Sea Research Part A, Oceanographic Research Papers*, 26(12):1311–1327.

Williams, T. D., Bennetts, L. G., Squire, V. A., Dumont, D., and Bertino, L. (2013a). Wave-ice interactions in the marginal ice zone. Part 1: Theoretical foundations. *Ocean Modelling*, 71:81–91.

Williams, T. D., Bennetts, L. G., Squire, V. A., Dumont, D., and Bertino, L. (2013b). Wave-ice interactions in the marginal ice zone. Part 2: Numerical implementation and sensitivity studies along 1D transects of the ocean surface. *Ocean Modelling*, 71:92–101.

Wu, C., Watanabe, E., and Utsunomiya, T. (1995). An eigenfunction expansion-matching method for analyzing the wave-induced responses of an elastic floating plate. *Applied Ocean Research*, 17:301–310.

Yiew, L. J., Bennetts, L. G., Meylan, M. H., French, B. J., and Thomas, G. A. (2016). Hydrodynamic responses of a thin floating disk to regular waves. *Ocean Modelling*, 97:52–64.